

Low-Cost and Sustainable All-Iron Redox Flow Battery Energy Storage



Megan Jayne Pritchard

**This thesis is submitted for the degree of MSc by
research**

September 2021

Department of Chemistry

Declaration

This thesis has not been submitted in support of an application for another degree at this or any other university. It is the result of my own work and includes nothing that is the outcome of work done in collaboration except where specifically indicated. Many of the ideas in this thesis were the product of discussion with my supervisor Dr Kathryn Toghill.

Abstract

Redox flow batteries are promising grid-scale energy storage devices as they are able to decouple battery power and capacity as either property can be independently scaled. Herein a novel all aqueous all-iron redox flow battery was developed. Iron was selected because of its low cost and due to its low-toxicity, the all-iron RFB is likely to have minimal detrimental effect on the environment. Using ferrocyanide as the redox active material in the positive electrolyte and iron triethanolamine in the negative electrolyte a columbic efficiency of >80% was achieved. A redox flow battery using ferrocyanide in the positive electrolyte and iron triisopropanolamine in the negative electrolyte was also developed which achieved >81% columbic efficiency. Capacity loss was seen over 25 cycles in all battery experiments, this was found to be due to the crossover of the negative redox active material over the membrane. Both Nafion-117 and BTMA membranes were evaluated to attempt mitigation of crossover.

Further scale up of the design is hindered by limiting solubility of the negative electrolyte redox active material, however, future work into improving the solubility by adding additives to the electrolytes may improve efficiency. Additives may also improve the stability of the redox active material during the charging and discharging process and avoid crossover of species.

Contents

Chapter 1 Introduction to Redox Flow Batteries

1.1	Grid scale energy storage.....	12
1.2	Redox flow battery technology.....	13
1.3	Iron RFBs.....	19

Chapter 2 Electrochemical Evaluation of Novel Iron Complexes

2.1	Introduction.....	29
2.2	Experimental.....	29
	2.2.1 Materials and reagents.....	29
	2.2.2 Equipment and procedures.....	30
2.3	Fundamental Electrochemical Theory.....	30
2.4	Results and Discussion.....	31
	2.4.1 Electrochemical evaluation of iron complexes as FeRFB catholytes.....	32
	2.4.2 Electrochemical evaluation of iron complexes as FeRFB anolytes.....	35
2.5	Conclusions.....	39

Chapter 3 Evaluation of an iron(III) triethanolamine and ferrocyanide redox flow battery

3.1	Background.....	41
3.2	Experimental.....	41
	3.2.1 Materials and Reagents.....	41
	3.2.2 Electrolyte preparation.....	42
	3.2.3 Iron (III) triethanolamine synthesis.....	42
	3.2.7 Electrochemical cell.....	42
3.3	Results and Discussion.....	47
	3.3.1 Electrochemical evaluation of iron(III) TEA.....	47
	3.3.2 UV-Vis measurements and solubility study.....	50
	3.3.3 Charge-discharge studies of K ₄ Fe(CN) ₆ & Fe(III) TEA.....	51
	3.3.4 Capacity loss investigations.....	57
3.4	Conclusions.....	62

Chapter 4 Evaluation of Iron(III) Triisopropanolamine

4.1 Background.....	63
4.2 Experimental.....	63
4.2.1 Materials and Reagents.....	63
4.2.2 Electrolyte preparation.....	64
4.2.3 Electrochemical measurements and electrochemical cell.....	64
4.3 Results and Discussion.....	64
4.3.1 Electrochemical evaluation of iron(III) TiPA.....	64
4.3.2 UV-Vis measurements and solubility study.....	66
4.3.3 Charge-discharge studies of $K_4Fe(CN)_6$ & Fe(III) TiPA.....	67
4.3.4 Capacity loss investigations.....	71
4.4 Conclusions.....	75
Chapter 5 Conclusions and future work.....	76
5.1 Conclusions.....	76
5.2 Future work.....	77
References.....	78
Appendix A -SEM and EDX.....	82
Appendix B-SEM and EDX.....	83
Appendix C-SEM and EDX.....	84

List of Tables

Table 1: Comparison of battery costs [25,26]	19
Table 2: Comparison of the redox potential, solubility and electrolyte pH of iron complexes [38, 39, 42, 44, 46-48]	26
Table 3. Comparison of the redox potential, ΔE_p , electrolyte pH and reported maximum solubilities of the iron complexes.	39
Table 4. Capacity during charging and discharging of Fe(III) TiPA with Nafion-117 and BTMA membranes.....	71

List of Figures

Figure 1: Schematic of a generic redox flow battery	14
Figure 2: Schematic of an all-iron redox flow battery	20
Figure 3: Pourbaix diagram of Iron in water	22
Figure 4: Cyclic Voltammogram showing the 'duck' reversible shape.....	31
Figure 5: Overlay of cyclic Voltammograms of 0.1 M $K_4Fe(CN)_6$, 1 M NaCl, 1 M NaOH, N_2 atmosphere, pH=14, GC WE, scan rates 0.02 - 0.5 Vs^{-1}	32
Figure 6 Overlay of cyclic Voltammograms of 0.1 M Fe(II) oxalate, 1 M NaCl, N_2 atmosphere, pH=7, GC WE, scan rates 0.02 - 0.5 Vs^{-1}	33
Figure 7 Overlay of cyclic Voltammograms 0.2 M Fe(II/III) DMSO, 1 M NaCl, N_2 atmosphere, pH 2, GC WE, scan rates 0.02 - 0.5 Vs^{-1}	34
Figure 8. a) Structure of DMSA ligand b) Overlay of cyclic Voltammograms of 0.1 M Fe(III) DMSA, 1 M NaCl, N_2 atmosphere, GC working electrode , GC WE, scan rates 0.02 - 0.5 Vs^{-1}	35
Figure 9. Overlay of cyclic Voltammograms 0.1 M ammonium iron(III) citrate 1M KOH, 1M NaCl, pH 13, N_2 atmosphere, GC WE, scan rates 0.02 - 0.5 Vs^{-1}	36
Figure 10. Overlay of cyclic Voltammograms of 0.1 M Fe(III) DTPA, 1 M NaCl, 1 M NaOH, pH=14, N_2 atmosphere, GC WE, scan rates 0.02 - 0.5 Vs^{-1}	37
Figure 11. Overlay of cyclic Voltammograms of 0.1 M Fe(III) TEA, 1 M NaCl, 3 M NaOH, pH=14.47, N_2 atmosphere, GC WE, scan rates 0.02 - 0.5 Vs^{-1}	38
Figure 12 Overlay of cyclic Voltammograms of 0.1 M Fe(III) TiPA, 1 M NaCl, 3 M NaOH, pH=14.47, N_2 atmosphere, GC WE, scan rates 0.02 - 0.5 Vs^{-1}	39
Figure 13. Gen 2 Flow-cell design. Top left) ppg-86 graphite flow through flow-field (FTFF) current collector. Top left) Assembled Flow-cell and electrolyte reservoirs. Bottom) Electrolyte reservoir lids with 3 inlet/outlets.....	44

Figure 14 a) SEM image of the carbon paper electrode. 100 μm scale b) Elemental analysis through EDX analysis.....	45
Figure 15 Peristaltic pump calibration for the flow-rate as a function of RPM. Norprene tubing and supporting electrolyte used (1M NaCl, 3M NaCl). Each data point representing the mean flow-rate, averaged over three measurements.	47
Figure 16 a) Cyclic Voltammetry of the blank electrolyte and Fe(III) TEA, 1M NaCl, 3 M NaOH, pH=14.47, N_2 atmosphere, GC WE, scan rate 0.1 Vs^{-1} b) Randles-Sevcik analysis of the scan rate dependence study shown in Figure 11.	48
Figure 17 Koutecky-Levich analysis of 0.1 M Fe(III) TEA, 1 M NaCl, 1 M NaOH electrolyte a) RDE LSVs as a function of rotation rate. b) Koutecky-Levich plots as a function of overpotential. c) plot of the logarithm of the kinetically limited current against overpotential.	49
Figure 18 Cyclic Voltammetry of synthesised 0.1 M Fe(III) TEA at 0.1 Vs^{-1} . 1M NaCl, 3 M NaOH, pH=14.47, N_2 atmosphere, GC WE First scan shown.	50
Figure 19 a) UV-Vis spectrum of 0.1 M, 0.2 M and 1/10 diluted 0.5 M concentration of Fe(III) TEA b) Calibration of Fe(III) TEA solubility.....	51
Figure 20 Charge-discharge curves of the 0.1 M $\text{K}_4\text{Fe}(\text{CN})_6$ / 0.1 M Fe(III) TEA battery with Nafion-117 membrane at 5 mA cm^{-2} between 1.6 and 0.9 V upper and lower potential thresholds in the flow cell.....	52
Figure 21 a) Evolution of charge-discharge curves as a function of capacity. b) Charge-discharge capacities and efficiencies as a function of cycle number. (Nafion 117 membrane).....	53
Figure 22 a) Cyclic voltammetry of Fe(III) TEA before and after charge-discharge studies at 0.1 Vs^{-1} b) Cyclic voltammetry of $\text{K}_4\text{Fe}(\text{CN})_6$ before and after charge-discharge studies at 0.1 Vs^{-1}	54
Figure 23 a) SEM image of the carbon paper electrode used in $\text{K}_4\text{Fe}(\text{CN})_6$ electrolyte. 100 μm scale b) SEM image of the carbon paper electrode used in Fe(III) TEA electrolyte. 100 μm scale.	54

Figure 24 Elemental analysis through EDX analysis of a) $K_4Fe(CN)_6$ electrolyte b) Fe(III) TEA electrolyte.....	55
Figure 25 Charge-discharge curves of the 0.1 M $K_4Fe(CN)_6$ / 0.1 M Fe(III) TEA battery with BTMA membrane at 5 mA cm ⁻² between 1.6 and 0.9V upper and lower potential thresholds in the flow cell.....	56
Figure 26 a) Charge-discharge capacities and efficiencies as a function of cycle number. b) Evolution of charge-discharge curves as a function of capacity. (BTMA membrane).....	56
Figure 27 Charge-discharge curves of the 0.1 M $K_4Fe(CN)_6$ /synthesised Fe(III) TEA battery at 5 mA cm ⁻² between 1.6 and 0.9V upper and lower potential thresholds in the flow cell.....	57
Figure 28 Charge-discharge curves of the symmetrical Fe(II/III) TEA battery with Nafion-117 membrane at 5 mA cm ⁻² between 1V and -1V upper and lower potential thresholds in the flow cell.....	58
Figure 29 a) 100 Cyclic Voltammograms of 0.1M Fe TEA electrolyte at 0.1 Vs ⁻¹ . b) Cyclic voltammetry of a charged Fe TEA (+2 oxidation state) at 0.1 Vs ⁻¹ scan rate, N ₂ atmosphere. first scan shown.....	59
Figure 30. 100 continuous cyclic voltammetry scans of 0.1 M $K_4Fe(CN)_6$ in 1 M NaCl with 3 M NaOH at 0.1 Vs ⁻¹ scan rate, N ₂ atmosphere, GC WE.....	60
Figure 31 Symmetric flow cell charge-discharge curves of 0.1 M Fe(II/III)(CN) ₆ in 1 M NaCl 3 M NaOH solution. Nafion-117 membrane at 5 mA cm ⁻² between 1V and -1V upper and lower potential thresholds in the flow cell.....	60
Figure 32 UV-Vis spectra of the 'blank' supporting electrolyte over 7 days whilst cycling with Fe(III) TEA electrolyte. Absorbance peak = 219 nm.....	61
Figure 33 Structure of triisopropanolamine (TiPA) ligand.....	63
Figure 34 Randles-Sevcik analysis of the Fe(III) TiPA electrolyte scan rate dependence study shown in Figure 12.	65
Figure 35 Koutecky-Levich analysis of 0.1 M Fe(III) TEA, 1 M NaCl, 1 M NaOH electrolyte a) RDE LSVs as a function of rotation rate. b) Koutecky-Levich plots as a function of	

overpotential. c) plot of the logarithm of the kinetically limited current against overpotential.	65
Figure 36 100 continuous cyclic voltammetry scans of 0.1 M $K_4Fe(CN)_6$ in 1 M NaCl with 3 M NaOH at 0.1 Vs^{-1} scan rate, N_2 atmosphere, GC WE.....	66
Figure 37 a) UV-Vis spectrum of 0.1 M, 0.2 M and 1/10 diluted 0.5 M concentration of Fe(III) TiPA b) Calibration of Fe(III) TiPA solubility.....	67
Figure 38 Charge-discharge curves of the 0.1 M $K_4Fe(CN)_6$ / 0.1 M Fe(III) TiPA battery with Nafion-117 membrane at 5 $mA\ cm^{-2}$ between 1.6 and 0.9 V upper and lower potential thresholds in the flow cell.....	68
Figure 39 a) Charge-discharge capacities and efficiencies as a function of cycle number. b) Evolution of charge-discharge curves as a function of capacity. (Nafion-117 membrane).....	69
Figure 40 Charge-discharge curves of the 0.1 M $K_4Fe(CN)_6$ / 0.1 M Fe(III) TiPA battery with BTMA membrane at 5 $mA\ cm^{-2}$ between 1.6 and 0.9 V upper and lower potential thresholds in the flow cell	70
Figure 41 A) Charge-discharge capacities and efficiencies as a function of cycle number. B) Evolution of charge-discharge curves as a function of capacity. (BTMA membrane).....	70
Figure 42 Charge-discharge curves of the symmetrical Fe(II/III) TiPA battery with Nafion-117 membrane at 5 $mA\ cm^{-2}$ between 1V and -1V upper and lower potential thresholds in the flow cell.....	72
Figure 43 a) SEM image of the carbon paper electrode after use in Fe(III) TiPA. 100 μm scale b) Elemental analysis through EDX analysis.....	73
Figure 44 A) Cyclic Voltammetry of 0.1 M Fe(III) TiPA, 1 M NaCl, 3 M NaOH after battery cycling, 0.1 Vs^{-1} scan rate, N_2 atmosphere, first scan shown. B) 0.1 M $K_4Fe(CN)_6$, 1 M NaCl, 3 M NaOH after battery cycling, 0.1 Vs^{-1} scan rate, N_2 atmosphere, first scan shown.....	74
Figure 45 UV-Vis spectra of the 'blank' supporting electrolyte over 7 days whilst cycling with Fe(III) TiPA electrolyte. Absorbance peak = 220 nm.....	75

List of Abbreviations

Abbreviation/ Acronym	Meaning
RFB	Redox Flow Battery
ROM	Redox-active Organic Molecules
phen	o-phenanthroline
DTPA	Diethylenetriamine pentaacetate
EDTA	Ethylenediaminetetraacetic acid
TEA	Tiethanolamine
DMSO	Dimethyl sulfoxide
DIPSO	3-[bis (2-hydroxyethyl) amino]-2-hydroxypropanesulfonicacid
TIPA	Triisopropanolamine
CV	Cyclic Voltammetry
CE	Coulombic Efficiency
VE	Voltaic Efficiency
EE	Energy Efficiency
PP	Polypropene
PTFE	Polytetrafluoroethylene
EDPM	Ethylene-propylene diene monomer
PFA	Perfluoroalkoxy alkane
FTFF	Flow through Flow Field
SEM	Scanning Electron Microscopy
GC	Glassy Carbon
WE	Working Electrode
RE	Reference Electrode
CE	Counter Electrode
RDE	Rotating Disk Electrode

Chapter 1 – Introduction to Redox Flow Batteries

1.1 Grid scale energy storage

The demand for energy is always increasing as the global population grows and economies develop. In the next 30 years energy needs are projected to increase by 50%,¹ with demand increasing from 11.4 billion tons of oil equivalent to 17.7 billion. Energy is a necessity on which our population relies and is utilised in most aspects of daily life. As our consumption of energy grows we must look at how we can meet this demand but also, avoid an emerging climate crisis resulting from man-made greenhouse gases. Therefore, a rapid decarbonisation of our energy networks is required urgently to offset carbon emissions.² Hence, there is an increased demand for renewable, carbon neutral energy sources as we move away from using fossil fuels, due to their adverse effects on the environment. Solar and wind power are an increasing source of renewable energy, but because of their unpredictable intermittent nature it would be impossible to rely on them fully to meet energy demand as their power generation fluctuates. A solution to this problem is developing an energy storage system which can store excess renewable electricity.³

Electricity storage technology supports energy networks in a number of ways, including ‘frequency response’ which is the rapid charging or discharging of the storage device in response to increased or decreased grid frequency which must be maintained to within 1% of 50 Hz. ‘Load levelling’ and ‘peak shaving’ enable the storage of energy generated during periods of low demand or high generation, which can then be delivered back during periods of high demand or low generation, respectively. Finally, ‘seasonal displacement’ is where electricity generated over different seasons is stored over many months to level the discrepancy between wind and solar generation through the year.⁴ Existing energy storage systems include short term high-power systems, such as capacitors and flywheels, and large-capacity systems, such as pumped hydropower, compressed air reservoirs, and batteries which deliver comparably lower power over longer periods.⁵ In this regard, batteries are currently the most practical energy storage system because they deliver the best compromise between power and capacity, whilst remaining geographically unrestricted.

Battery technologies

The most common rechargeable battery is lead-acid which is low cost and the most mature, but has a low life cycle, poor depth of discharge (the extent to which the battery can be discharged) and poor charge retention.^{3,6} Other types of rechargeable batteries include lithium-ion⁷ and nickel-cadmium batteries which have a good cycle life, efficiency and high energy density but are expensive. These traditional battery technologies have an enclosed configuration where energy is intrinsic to the electrodes which can impact their scalability as all the battery components require scaling up to increase capacity. Therefore, the grid-scale application of these technologies becomes problematic due to increasing costs and the challenging logistics of managing each individual cell connected within the battery packs.⁸

Alternatively, there is the redox flow battery (RFB) technology which was first developed in the 20th century. The RFB design offers a semi-continuous electrochemical system where redox mediators in solution are charged and discharged at electrodes, but the charged/discharged electrolytes are stored separately in reservoirs external to the electrochemical cells. This system effectively decouples the power and capacity of the RFB because power is dependent on the total electrode area, whereas the capacity is dependent on the total volume of electrolytes. Hence, the RFB technology is highly flexible and more easily scalable compared to other battery technologies.⁸

1.2 Redox flow battery technology

Operating principles

RFBs are electrochemical energy storage devices that store electrical energy in the form of charged electrolyte solutions. Each half-cell of the battery contains a separate electrolyte and redox active species which are stored in tanks separate from the electrochemical cells. These are for the negative redox process (anolyte) and the positive redox process (catholyte) which only when operating do the catholyte and anolyte circulate through the cell, driven by a pump.⁹ A membrane is used in the electrochemical cells to stop the electrolytes mixing. An effective membrane must have the ability to prevent the preferential transfer of water from one half-cell to the other as this results in flooding of one half-cell while diluting the other.¹⁰ The membrane must also have low permeability to the redox active material but high

permeability to the charge carrying hydrogen ions. In large systems, the cells are collated electrically in series and parallel to give a stack through which the electrolytes flow.

When an RFB is charged an electron is released by an oxidation reaction on the positive side of the battery. These electrons leave the positive side of the cell stack and enter the negative side of the cell stack. In turn, a reduction reaction on the negative side of the battery occurs. To complete the circuit, ions in the solution migrate through the membrane to maintain electroneutrality. When the battery is discharged the current and the chemical reactions are reversed. A schematic representation of an RFB is shown in Fig.1.

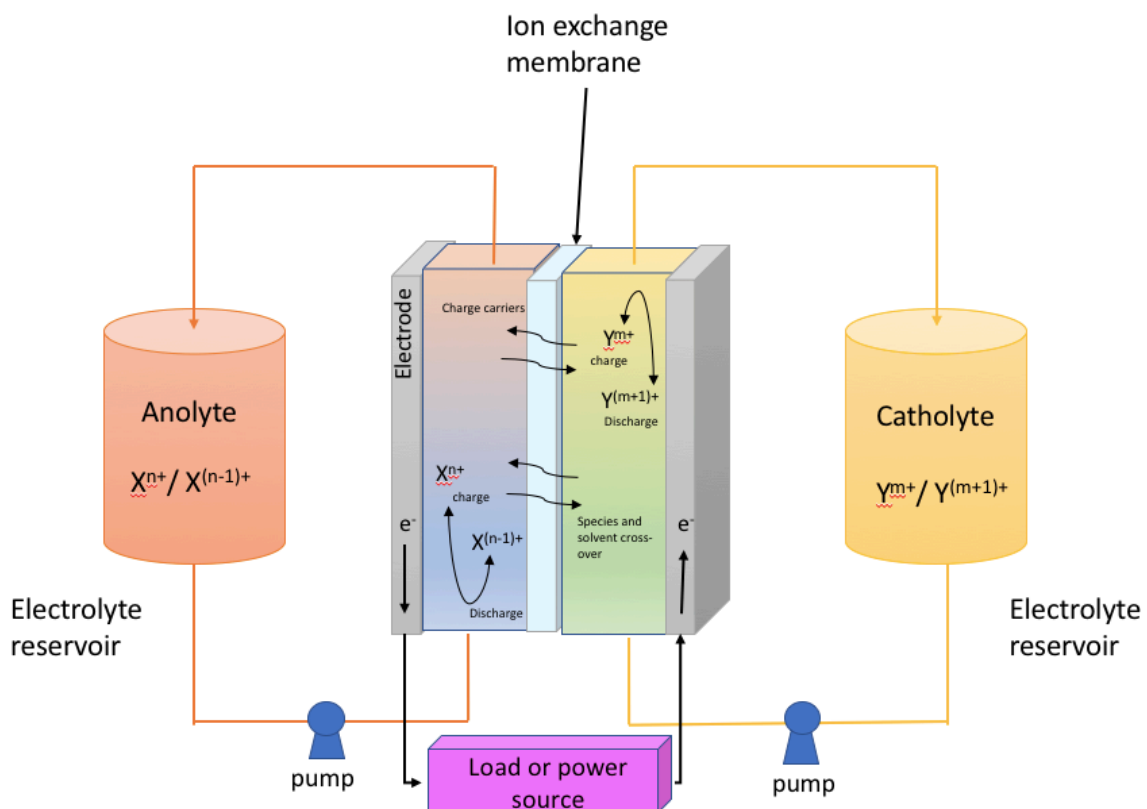


Figure 1. Schematic of a generic redox flow battery. Redrawn based on Figure 1 by Weber et al.⁹

The electrolyte is made up of solvent which can be aqueous/non-aqueous, salt such as NaCl which acts as a supporting salt and the redox active species which dictates the overall performance of the RFB. The redox potential and solubility are essential when considering the energy density, as the amount of energy that can be stored by a flow battery will depend on the solubility of the chemicals. The size of the tanks that store and pump the electrolyte also have an effect on capacity as this decides the volume of electrolytes that can be used. The equilibrium potentials of the active species in the half cells must also be taken into account as they determine the cell voltage.

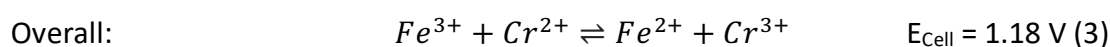
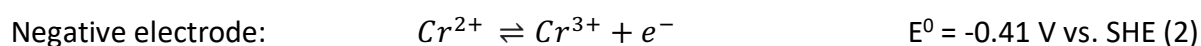
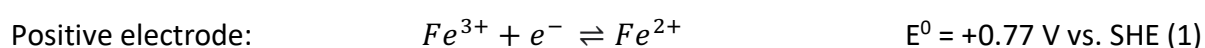
The design of RFBs allow them to accommodate any pairing of electrolytes and aren't limited to using water as a solvent. The redox chemistry of a flow battery is critical to its cost and performance, but the technology offers a wide scope for electrolyte design and development.

Efficiency of the RFB is also an important issue, the overall energy efficiency of the battery is specified by columbic and voltage efficiency.¹¹ The coulombic efficiency is defined as the ratio of the number of charges that enter the battery during charging, to the number that can be extracted from the battery during discharging. The voltage efficiency is determined by the voltage difference between the charging and discharging voltage of the battery. The differences between the charge and discharge performance can due to multiple reasons such as the electrode kinetics, reaction kinetics, cell design, membrane resistances and electrolyte flow rates.¹² Therefore, the characterisation of a flow battery requires consideration of many aspects of the design concurrently to minimise energy losses.

Electrolyte chemistries

Traditional RFBs

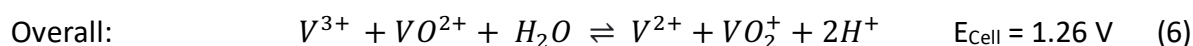
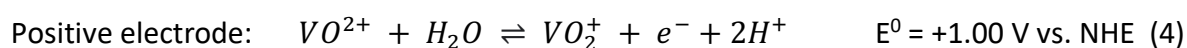
Developed in the 1970s by NASA, the iron chromium system is considered to be the first true RFB.¹³ It utilizes abundant chromium and iron chlorides as redox active materials, making it a very cost effective RFB.¹⁴ The iron chromium RFB produces a cell voltage of 1.18 V through the half-cell reactions given by Eqs. 1 and 2. The overall reaction is shown by Eq. 3. Note that the cell voltage is defined here as the open-circuit voltage at 50% state of charge (SOC).



Despite the low cost, the chromium redox couple has slow kinetics and requires expensive and problematic electrocatalysts. The iron chromium RFB (FeCrFB) also faces problems regarding crossover of the iron into the chromium electrolyte and *vice versa*. This is problematic for all flow batteries which have so called asymmetric chemistry, where in the redox active species in the half cells is markedly different. Such crossover causes irreversible cross-contamination of the battery electrolytes and loss of battery capacity with time.

A symmetric battery is a system that consists of a single parent molecule that can be oxidized and reduced to facilitate the positive and negative electrode half reactions.¹⁵ The first

example of this was an all-vanadium redox flow battery (VRFB) which uses the four stable aqueous oxidation states of vanadium in acid. Having vanadium on both sides of the battery means that any migration of the vanadium species through the membrane results in slight self-discharge rather than cross-contamination.¹⁶ This discharge can then be countered by simply rebalancing the electrolytes and fully charging the battery. The VRFB is also able to achieve a maximum energy density of 38 Wh/L, which is relatively high for a RFB, but typically lower than other battery technologies.¹⁷ The VRFB produces a cell voltage of 1.26 V.



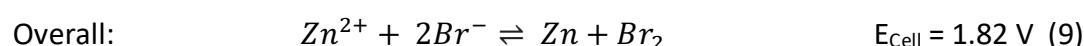
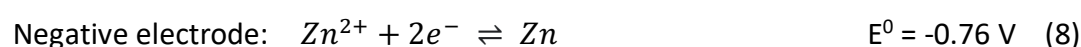
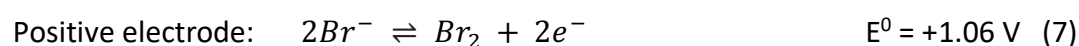
The kinetics of both half-cell reactions are very poor. Heterogeneous rate constants for the vanadium species are approximately 10^{-6} cm/s, which is highly irreversible, in an electrochemical sense. Nevertheless, both the VRFB and FeCrFB exhibit good energy efficiency, owing to the enhanced mass transport and high concentrations of the electrolytes. Both of these RFBs demonstrate high energy efficiencies of 80.3% and 78.4% for the VRFB and the iron chromium RFB at a current density of 120 mA cm^{-2} , respectively.¹⁸ However, the cost of vanadium has prevented the technology from being viable. There are also concerns about the eco-friendliness of vanadium(V) oxide which is used in all-vanadium RFBs as it is toxic to aquatic life with long lasting effects.¹⁹

VRFBs are capable of long lifetimes of >20 years without needing to replace the electrolytes.¹⁶ This is due to the redox mediators remaining in solution and consequently avoiding any phase changes at the electrodes. Solid phase changes, as seen in conventional batteries and ion intercalation batteries, rapidly decrease the lifetime of a battery system because of irreversible morphological changes.²⁰

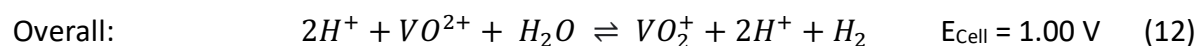
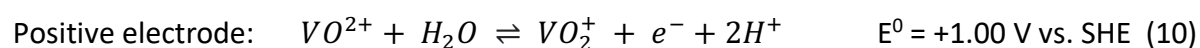
Hybrid RFBs

Batteries in which not all the redox-active material exists in a flowing form in a maximum of one half-cell are referred to as hybrid RFBs, where one half-cell involves either the evolution of a gas or deposition of a solid.⁸ The zinc/bromine system is one of the oldest RFB hybrid systems. In which a $ZnBr_2$ solution is used. Zinc deposition proceeds in neutral aqueous

solutions because the hydrogen evolution reaction is kinetically inhibited and results in a high hydrogen overpotential. The zinc is deposited on a carbon anode which limits the capacity. The incomplete dissolution of zinc and differences in current-density leads to a risk of dendrite formation as deposition doesn't proceed uniformly. Consequently, this leads to losses in efficiency or complete failure. However, the ZnBr battery is a well-established commercialised system with much lower operating costs than the VRB, due to its availability and high negative electrode potential. The ZnBr battery produces a standard voltage of 1.82 V.



Hydrogen-based systems are another example of hybrid RFBs. The hydrogen-based anode is combined with a suitable cathodic redox couple such as Br_2/Br^- or $\text{VO}_2^+/\text{VO}^{2+}$ and continuous process management is performed with electrolyte circulation. The H_2/V flow batteries operate using a Pt-based anode coated in a catalyst. An electrolyte containing 1 M $\text{VO}_2^+/\text{VO}^{2+}$ in 5 M H_2SO_4 is able to achieve a maximum power density of 114 mWcm^{-2} and a charging/discharging energy efficiency of 60 %. The H_2/V flow battery produces a cell voltage of 1.00 V.



Emerging chemistries

A purely organic RFB can be created using redox-active organic molecules (ROM). Electrolytes containing ROMs are capable of high energy densities because ROMs can be highly soluble ($\approx 1 \text{ M}$)²¹ and so are appealing to use in a RFB because of their low cost and sustainability.²² However, the decomposition of ROMs in various electrolyte media is presently problematic due to their relative complexity compared to simple metal ion RFBs, ROMs display a lack of stability, which causes irreversible capacity loss via decomposition.

Metal-organic complexes on the other hand are much more stable.²³ Metal salts can be complexed with organic ligands to achieve relatively high solubilities in organic and aqueous solvents (≈ 2 M for VRFB) in organic and aqueous.²⁴ The transition metals at the centre of these complexes can exist in multiple oxidation states and can therefore be used in symmetric RFBs. Metal-organic complexes show how the electrochemistry of metals can be altered by complexing with ligands and how solubility can be drastically improved by the addition of solubilising groups to the structure.²⁵

Non-aqueous chemistry

Non-aqueous RFBs use aprotic solvents such as ethers, nitriles and carbonates. Aprotic solvents have a wider electrochemical working potential range than protic electrolytes and can dissolve redox couples that are unstable in aqueous or protic media.²⁶ Higher cell voltages should therefore be achievable by using an RFB with aprotic electrolyte solutions. In comparison to water, the oxidative and reductive decomposition of organic solvents tend to occur at higher/lower potentials respectively. Therefore, redox materials which reside outside the water stability region can be utilised in aprotic solvents.

The temperature range at which the solvents are a liquid is another vital property to take into consideration for a RFB. Due to the freezing temperature of water being $0\text{ }^{\circ}\text{C}$, it is unsuitable for use within the electrolyte for climates that regularly experience sub-zero temperatures. In contrast, aprotic solvents are typically in a liquid state for larger temperature ranges, for example N,N-Dimethylformamide (DMF) is a liquid between $-60.4\text{ }^{\circ}\text{C}$ and $153.0\text{ }^{\circ}\text{C}$. Although few solvents possess the combination of a high relative permittivity/low viscosity, which are characteristics of water, they are not as readily available and so increase the cost of the RFB. Hence, water is a more cost-effective choice for a RFB.

RFB Limitations

Limitations of current battery technologies include cost and sustainability. A comparison of costs between RFB and other rechargeable batteries is shown in Table 1. The VRFB uses expensive vanadium materials and the V(V) H_2SO_4 electrolyte is very corrosive and oxidising, whilst the Fe-Cr RFB uses cheaper metal salts but relies on expensive electrocatalysts which makes the battery less cost effective. The energy density, a measure of how much energy a battery contains in proportion to its weight, of RFBs is also a limiting factor; other battery

technologies such as Li-ion have much higher energy densities.²⁷ However, in the context of stationary storage, energy density is a less critical factor, especially as the capacity of the RFB can be scaled distinctly from its power output. When these limitations are considered with respect to the lifetime, the duration of charge and discharge at which RFBs operate, their potential for use in grid scale stationary storage is evident.

Battery	Capital cost (\$/KWh)	Lifetime (cycles/years)	Discharge duration (h)	Citation
VRFB	435 - 952	>2000 / >10	4-10	25,26
Li-ion	223 - 323	750 - 3000 / 6-8	1-5	25,26
Lead-acid	120 - 291	1000 - 1200 / 3-4	3-5	25,26
Sodium-sulphur	400 - 1000	2500 - 4500 / 6-12	6-8	25,26

Table 1. Comparison of battery costs

The high capital cost of RFBs is an issue as it is not cost effective to store electricity at such high cost per kWh. The Department for Energy in the US set the target of \$150 /kWh a decade ago, which is beyond the scope of the RFB, and even the ZnBr battery. The plummeting cost of Li-ion batteries is also a problem for RFBs,²⁸ as these technologies have been widely deployed in portable electronics, and therefore already have public acceptance.

Alternative chemistry is the most probable way in which RFB technologies will become competitive in the energy storage market. The target is a symmetric battery that is low-cost, sustainable and has a sufficiently high energy density to surpass the commercial VRB. An aqueous all-iron redox flow battery could be the solution because of its inexpensive materials and the natural abundance of iron salts.

1.3 Iron RFBs

Properties of Fe RFBs

In 1981, Hruska and Savinell²⁹ pioneered the first hybrid all-iron RFB using the Fe²⁺/Fe redox pair in the negative electrolyte and the Fe³⁺/Fe²⁺ redox pair in the positive electrolyte. This was a promising start to research into all-Fe RFBs however, the use of solid metallic iron involved in the negative redox reaction meant that the energy and power of the RFB was no longer completely decoupled from each other. There was also a concern of dendrite formation because of the deposition and dissolution of the metallic iron on the negative electrode which

can cause the battery to short-circuit. Moreover, the standard redox potential of Fe^{2+}/Fe couple is 450 mV more negative than that of hydrogen evolution reaction (HER) at pH=0, which also posed a challenge. The all-iron RFB is represented in Fig.2 comprising simple chloride salts.

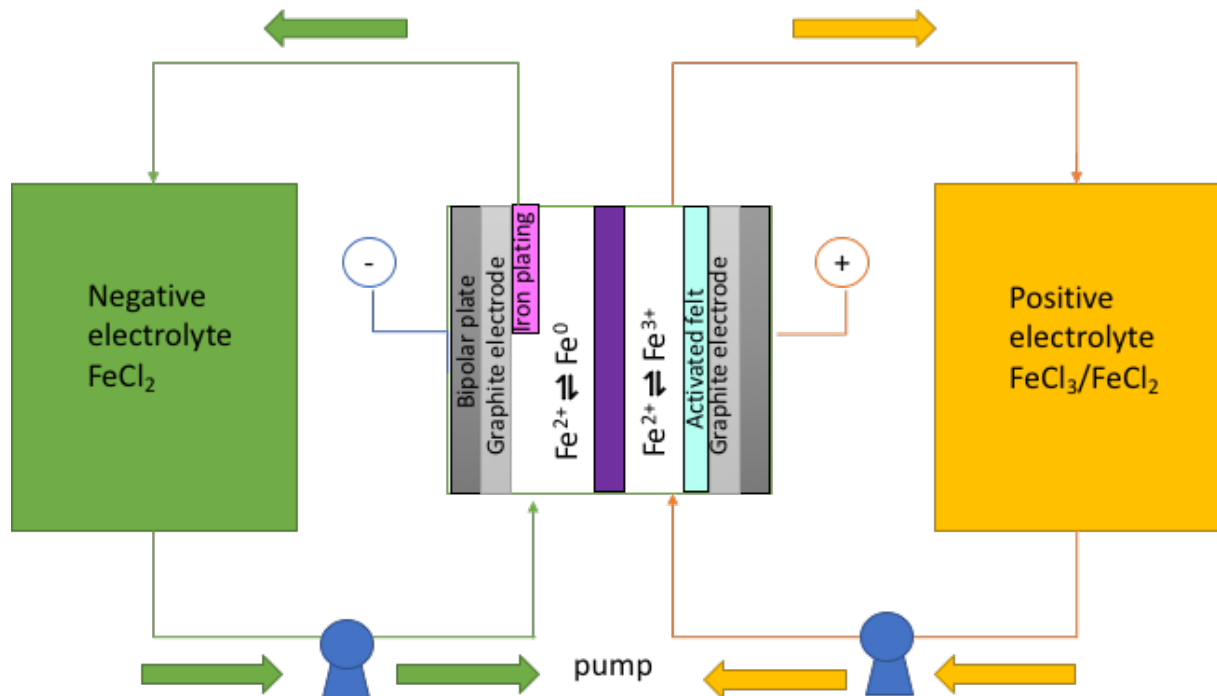
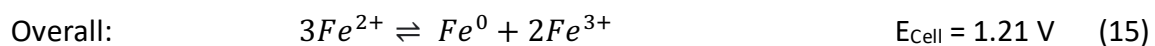


Figure 2. Schematic of an all-iron redox flow battery. Redrawn based on Figure 2 by Dinesh et al.²⁵

Typically, the positive electrolyte contains iron in a +3 oxidation state and the negative electrolyte contains iron in a +2 oxidation state. During charging the iron(III) in the positive electrolyte is reduced and the iron(II) in the negative electrolyte is oxidised from Fe(0) to Fe(II). The electrolytes, which are stored in external tanks, flow through the cell stacks of the battery and take part in the half-cell reactions given by Eqs. 13 and 14. The overall reaction is shown in Eq. 15. The negative electrode utilizes plating and dissolution of iron as a solid plate.³⁰ The positive electrode uses a carbon structure to oxidise and reduce iron which remain in solution.



The cell voltage of the all-iron FB is 1.21 V which is similar to that of the all vanadium RFB of 1.26 V at 50% state charge.³¹

The iron plating potential is more negative than the hydrogen evolution in acid. By operating at a pH of around 3, the HER can be mitigated as this will shift the equilibrium

potential of hydrogen evolution more negative. However, this presents a challenge at the positive electrode as Fe(III) will precipitate to form ferric hydroxide at pHs greater than about 2.³² To avoid precipitation of Fe(III) it is possible to use complexing ligands in the positive electrolyte.

Inorganic chemistry of iron

Iron is a transition metal and therefore has multiple oxidation states since it is relatively easy for transition metals to lose electrons is because of their incomplete d-sub shell. The electron configuration for Fe is $[\text{Ar}]3d^6 4s^2$, the outermost s electrons are always removed first in the process of forming transition metal cations. Iron is therefore stable in a +2 oxidation state as the 2 electrons from the 4s sub-shell are removed to give the electronic configuration of $[\text{Ar}]3d^6$. A half-filled d-sub shell (d^5) is also particularly stable which is the result of an iron atom losing a third electron which gives rise to a +3 oxidation state with the electronic configuration $[\text{Ar}]3d^5$. Transition metals can form coordination complexes because they have empty valence shell orbitals that can accept pairs of electrons. In an iron complex the iron acts as a Lewis acid that is coordinated by one or more ligand which act as a Lewis base, forming coordinate bonds.³³ The atoms in the ligands that are directly bonded to the iron are known as donor atoms, a ligand that bonds to the iron centre once is a monodentate ligand. A chelated compound forms when the ligand is bonded to the iron centre at two or more points.

Aqueous coordination complexes of iron in RFBs

The simplest iron complex in aqueous solutions is $\text{Fe}(\text{H}_2\text{O})_6$, where the metal ion is coordinated to six water molecules in acidic pH. Figure 3 is a Pourbaix diagram for iron in water and indicates the various redox states of iron with respect to pH and electrode potential. In $\text{pH} < 2$ the Fe(II) and Fe(III) species are stable, but at higher pH the metal ion begins to precipitate as iron oxide solid. Nevertheless, the Fe(II)/(III) couple is well established in the natural world, featuring in many biological processes owing to an accessible redox potential of 0.77 V vs the SHE. The formation of complexes with organic biomolecules means that the Fe(II)/(III) couple can operate at higher pH without precipitation. Furthermore, the Fe(II)/(III) species typically exhibits slow heterogeneous kinetics, with rate constants of the order of 10^{-3} cm/s, whereas iron-ligand complexes often exhibit faster redox kinetics, rendering them more suited to RFB reactions that can deliver a high current density.

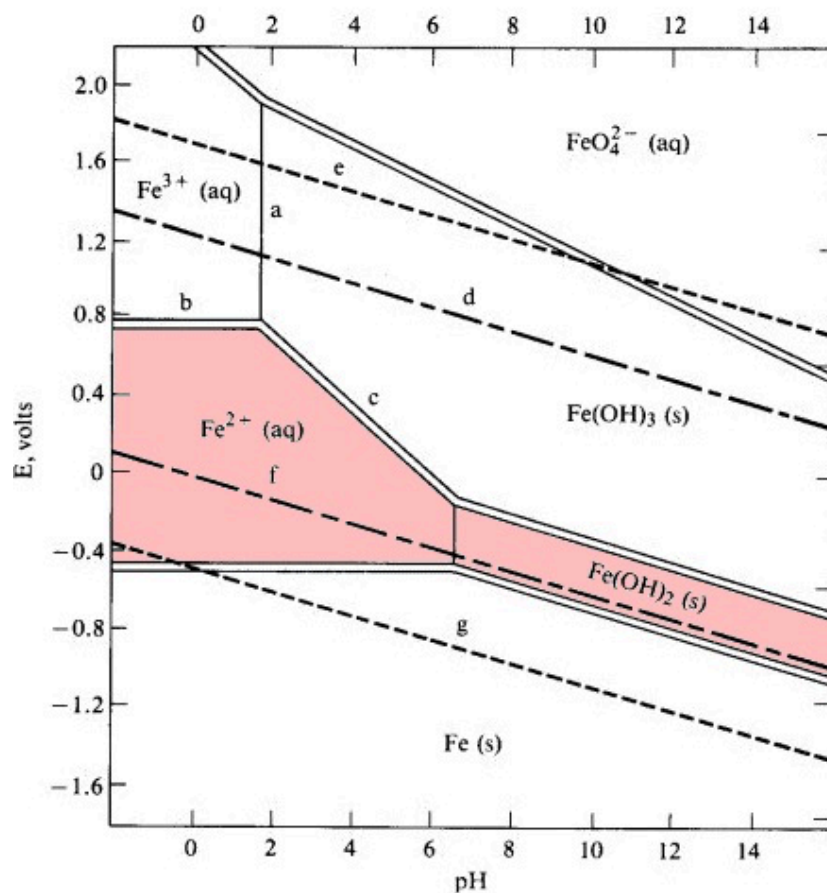


Figure 3. Simplified Pourbaix diagram for 1 M Iron solutions ³⁴

Whilst investigating the all-Fe RFB Hruska and Savinell²⁹ found that raising the pH of the electrolyte suitably suppressed the competing HER. This shifts the equilibrium potential to the highly negative region and results in a drop in diffusion-controlled current due to H₂ evolution. But, the change in pH also impacted on the positive electrode process by prompting the precipitation of the Fe(III).³⁵ To overcome this problem, organic ligands were used as complexing agents for Fe(III) to mitigate its precipitation.²⁷ Very few publications have reported on successful all-iron complex RFBs, however a number of ligands have been employed with an iron centre to preliminarily evaluate their performance as possible RFB electrolytes.⁴⁰⁻⁵⁰ These are discussed below, considering whether the complex is suitable to use as the anolyte or catholyte species of an all-iron RFB. Their overall performances are also presented in Table 2.

The near-reversible [Fe(CN)₆]³⁻/[Fe(CN)₆]⁴⁻ redox couple has been used frequently in electrochemical measurements and energy storage.^{36,37} K₃[Fe(CN)₆] and K₄[Fe(CN)₆] are now being applied to RFBs, the first example was K₃[Fe(CN)₆] being used as a catholyte in a Zn/

$K_3[Fe(CN)_6]$ semi-flow alkaline RFB.³⁸ The redox reaction of ferrocyanide follows a quasi-reversible state at room temperature and as temperature increases the state becomes irreversible. Using a carbon felt containing carbon-oxygen functional groups alleviates the irreversibility in the redox reaction.³⁹ The aqueous solubility of $Fe(CN)_6$ is 0.4 M in pH 14 and the standard potential of the $Fe(CN)_6^{3-}/Fe(CN)_6^{4-}$ redox pair is 0.36 V (vs SHE), however the formal potential depends on the ionic strength of the solution. A solution with an ionic strength equivalent to a 0.5 M salt solution has a redox potential of 0.44 V (vs. SHE).⁴⁰ It is a reliable iron complex with well-established voltammetry and kinetics, such that it is frequently used as a catholyte to help evaluate new RFB anolytes in asymmetric systems.

The Fe(II/III) redox couple was complexed with o-phenanthroline (phen) type ligands by Chen et al.⁴¹ It was found that the complexation of the redox couple with phenanthroline or bipyridyl type ligands results in significant positive shifts in the potential of the redox couple, because of the formation of a more stable Fe(II) complex. The redox potential of Fe(phen) was 1.064 V (vs.SHE) in 0.5 M H_2SO_4 electrolyte and the solubility of the Fe(phen) complex is 0.8 M. However, there was partial loss of capacity upon long term storage due to the instability of the ferric form.

Complexing agents

The Fe(DTPA) complex is formed from the complexation of the Fe(II/III) redox couple with Diethylenetriamine pentaacetate (DTPA). The Fe(DTPA) has the redox potential range of 0.029 V to 0.120 V (vs. SHE) at pH ranges 4 to 10 which forms a more stable Fe(III) complex.^{42,43} A concentration of 0.1 M was soluble in the supporting electrolyte of 0.1 M NH_4F . This makes the Fe(DTPA) unsuitable to use in the positive electrolyte but it could be suitable to use in the negative half-cell of an all-iron RFB if paired with a highly positive active species in the positive half-cell.⁴⁴

The Fe(II/III) redox couple has been complexed with ethylenediaminetetraacetic acid (EDTA) to create the Fe(EDTA) complex which causes the formal potential of the iron redox couple to shift in the negative direction.²⁷ The redox potential of the Fe(EDTA) complex was 0.089 to 0.109 V (vs. SHE) between pH 3 and 7, indicating a proton dependence in the redox chemistry. A concentration of 0.15 M was soluble in the supporting electrolyte of 0.1 M NH_4F , these properties make the iron complex unsuitable to use in the positive half-cell of an all-iron RFB as compared to the ferrocyanide redox couple the half-cell potential isn't high enough.^{45,42}

The Fe(II/III)-(TEA) complex was evaluated for use in an iron-bromine RFB.⁴⁶ Complexing the Fe(II/III) redox couple with triethanolamine (TEA) shifts the Fe(II/III) reaction potential to around -0.816 V (vs. SHE). This was based on an electrolyte containing 0.05 M Fe(III)-TEA complex, 1 M NaOH and 0.4 M NaCl which had a pH of 13.96 . The Fe(II/III)-TEA complex is soluble in alkaline media to a maximum concentration of 0.6 M and the reported open circuit voltage of the Fe-TEA/Br₂ cell was 1.9 V. Further experiments are required to increase the long-term stability and solubility of the electrolyte which was shown to degrade and precipitate.

In 2016, a new all-soluble all-Fe RFB was proposed by Gong⁴⁷ using an iron-triethanolamine redox pair and iron-cyanide redox pair. The $[\text{Fe}(\text{TEA})\text{OH}]/[\text{Fe}(\text{TEA})(\text{OH})]^{2-}$ couple has a redox potential of -0.86 V (vs. SHE), creating a 1.34 V of formal cell voltage. The electrolyte had a pH of 13 and contained 0.2 M FeCl₂, FeCl₃, 2 M TEA and 3 M NaOH. The RFB demonstrated good performance with a discharge density power greater than 160 mVcm⁻² however, the free TEA ligand was able to crossover the membrane and therefore membrane selection must be taken into consideration.

The organic complex Fe(DIPSO) consists of iron and 3-[bis (2-hydroxyethyl) amino]-2-hydroxypropanesulfonicacid (DIPSO) ligand. The Fe(DIPSO) complex has been suggested as a negative species for an all-Fe RFB where ferrocyanide is used as the positive species. The cell voltage for this RFB is 1.37 V⁴⁸ and the redox potential of Fe(DIPSO) is -0.851 V (vs. SHE), which is equal to that of Fe(TEA). In comparison to Fe(TEA), the Fe(DIPSO) has a stronger resistance against reduction to Fe(s) leading to a better performance and more stable RFB. In the RFB, 0.5 M of Fe(CN)₆ was used and as Fe(DIPSO) is a one electron transfer process 0.5 M of the complex was used to preserve the stoichiometric balance.

Recently the Fe(II/III) redox couple was complexed with new triisopropanolamine (TiPA) ligand.⁴⁹ The Fe(TiPA) complex that was used successfully as a negative redox species is an iron-cobalt RFB, with a redox potential of -0.901 V (vs. SHE). The Fe(TiPA) has the potential to be used as the negative species in an all-Fe RFB with a potassium hydroxide electrolyte and has a solubility of 0.81 M in 5 M KOH. When compared to Fe(TEA), the Fe(TiPA) is much more stable in KOH, enabling the stable redox reactions over a longer period (90% capacity retention over 100 cycles)⁴⁹.

A screening of multiple organic ligands as complexing agents for Fe(III) ions to use in the positive electrolyte of an all-Fe RFB was completed by Hawthorne et al.⁵⁰ Iron citrate was

found to shift the potential negatively to -0.040 V (vs. SHE), even at its natural pH of 5.25 which makes citrate unsuitable to use in the positive electrolyte but it has the potential to be used in the negative electrolyte.

The Fe(malic acid) has a redox potential of 0.701 V (vs.SHE) at pH 0.67, can be utilised as a species in the positive electrolyte. Malic acid has good solubility in aqueous media at 4.16 M, however, when the pH was adjusted to 2.5 the potential shifted negatively to -0.111 V (vs. SHE) making Fe(malic acid) unsuitable for the positive electrolyte.

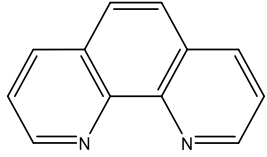
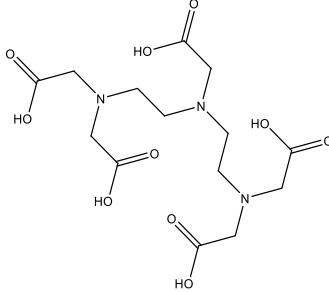
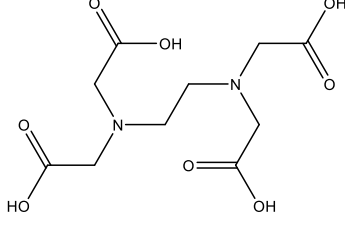
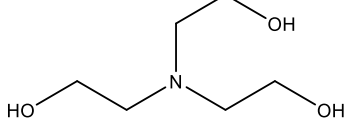
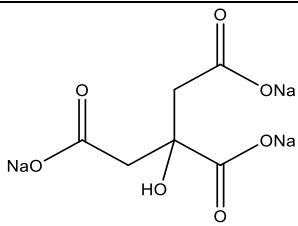
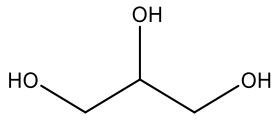
The Fe(glycerol) complex has a redox potential of 0.690 V (vs.SHE) at pH 1.5 and a redox potential of 0.706 V (vs.SHE) at pH 2.5. This makes it a feasible option to use as a species in the positive electrolyte and glycerol is miscible in aqueous media. However, the diffusion coefficients of both Fe(glycerol) and Fe(malic acid) could not be measured due to irreversibility in electrokinetics at the adjusted pH 2.5.

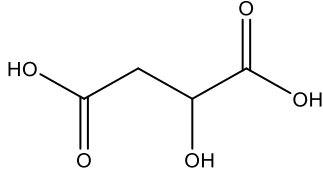
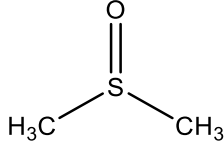
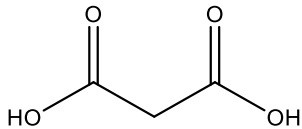
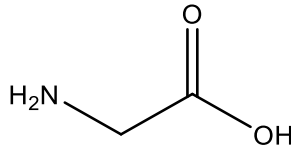
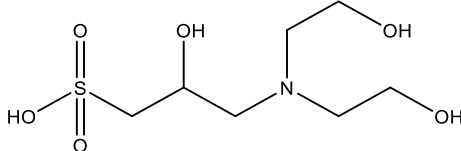
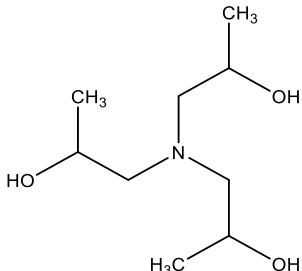
Fe(malonic acid) displays good kinetics and is miscible in aqueous media, it has a redox potential of 0.684 V (vs.SHE) at pH 0.73. When the pH is adjusted to 2.5 using NaOH, the potential becomes less positive at 0.305 V (vs.SHE), which isn't feasible to use in a positive electrolyte when other species have more positive redox potentials.

The Fe(DMSO) complex is formed from the complexation of the Fe(II/III) redox couple with dimethyl sulfoxide (DMSO), the complex exhibits good kinetics and has a redox potential of 0.680 V (vs.SHE) at pH 1.78. Upon adjusting the pH to 2.5 the potential is not greatly affected at 0.684 V (vs.SHE). DMSO is also highly soluble in aqueous media making it a possibility for use in the positive electrolyte.

The Fe(glycine) gave the best electrochemical performance of all the complexes screened, as the kinetics and diffusion coefficients were near those of ferric/ferrous ions without ligands. The electrolyte containing 4:1 glycine to iron had a redox potential of 0.516 V (vs.SHE) at pH 2.85 and upon adjusting the pH to more acidic conditions, the redox potential was 0.565 V (vs.SHE). The electrolyte containing equal parts glycine to iron showed a high open circuit potential of 0.667 V (vs.SHE) and it was stable at the adjusted pH of 2.5.

Fe redox material Comparison

Complex	Redox potential vs. SHE (a)	Electrolyte pH	Solubility (M)	Ligand structure	Citation
Fe(phen)	1.064 V	0	0.8M		41
Fe(DTPA)	0.120 V – 0.029 V	3-10	0.1M		44
Fe(EDTA)	0.109 V – 0.089 V	3-7	0.15M		44
Fe(TEA)	-0.816 V	13.96	0.6M		46
Fe(CN) ₆	0.44 V	14	0.76M		40
Fe(citrate)	-0.040 V	5.25	2.45		50
Fe(glycerol)	0.690 V	1.5	Miscible		50

Fe(malic acid)	0.701 V	0.67	4.16		50
Fe(DMSO)	0.680 V	1.78	Miscible		50
Fe(malonic acid)	0.684 V	0.73	Miscible		50
Fe(glycine)	0.516 V	2.85	3.33		50
Fe(DIPSO)	-0.851 V	14	Not mentioned, 0.5M used		48
Fe(TiPA)	-0.901 V	-	0.81M in 5M KOH		49

(a) Potential was converted to standard hydrogen potential (SHE) by relationships: SCE = 0.244 V vs SHE, Ag/AgCl = 0.199 V vs SHE.

Table 2. Comparison of the redox potential, solubility and electrolyte pH of iron complexes

Based on redox potentials given in Table 2, we can see that the best redox materials for use in a positive electrolyte are Fe(phen), Fe(glycerol), Fe(malic acid), Fe(DMSO), Fe(malonic acid) and Fe(glycine). The solubility of the redox material is also important as it dictates the amount of energy the battery can store, for this reason Fe(phen) becomes a less viable option compared to the other complexes. The redox potentials of Fe(TEA), Fe(DIPSO) and Fe(TiPA)

make them promising options to use in a negative electrolyte however, their solubility is poor (< 0.5 M) when compared to complexes with positive redox potentials.

All-iron RFBs are promising energy storage devices which could store excess renewable energy on a grid scale. They are able to store energy for longer durations of time whilst being cost effective and due to iron's low-toxicity, are likely to have minimal detrimental effect on the environment. There have been some ligands that have proved to be successful in the positive electrolyte reactions, but have hindered the negative electrode reactions by interfering with the iron plating at the negative electrode of the all-Fe RFB.⁵¹ To further develop the all-Fe RFB, more research into iron salts and ligands that could be used in the electrolytes is required. In particular, research into organic ligands that enhance solubility and kinetics of the redox active species whilst remaining cost effective are required.

Chapter 2 – Electrochemical Evaluation of Novel Iron complexes

2.1 Introduction

The screening of multiple iron complexes was carried out to evaluate their electrochemical behaviour and their suitability to be used in as the redox active electrolytes in an all-iron redox flow battery (FeRFB). To achieve a desirable energy storage capacity in a flow battery a high solubility of iron active material is required. An FeRFB requires a pH above 3 to avoid HER at the negative electrode, therefore alkaline pHs were generally used. At these pHs precipitation of the ferric ions can occur as $\text{Fe}(\text{OH})_3$. To prevent this precipitation an investigation into complexing iron with different complexing ligands was carried out. A successful iron-ligand complex will exhibit fast and reversible electrokinetics with moderate solubility and the ligand should be electrochemically inactive. The ligands investigated in this work were selected due to their availability or their promising usage in literature which could be improved by using alternative supporting salt, the ligand/complexes investigated included meso-2,3-dimercaptosuccinic acid (DMSA), diethylenetriaminepentaacetic acid (DTPA), dimethyl sulfoxide (DMSO), citrate, triethanolamine (TEA), triisopropanolamine (TiPA), oxalate and ferrocyanide. The structures of the ligands/complexes have been illustrated in Table 1 in Chapter 1.

2.2 Experimental

2.2.1 Materials and Reagents

Iron(III) chloride hexahydrate (98%, reagent grade), meso-2,3-dimercaptosuccinic acid (98%), dimethyl sulfoxide(99%, BioReagent), diethylenetriaminepentaacetic acid (99%), iron(II) oxalatedihydrate (99.99%), triethanolamine (99%, Sigma Aldrich), triisopropanolamine (99%, Sigma Aldrich), ammonium iron(III) citrate (reagent grade) potassium hexacyanoferrate(II) trihydrate (98%, ACS reagent), sodium Chloride (99%, ACS reagent) and sodium hydroxide (98%, BioXtra) were purchased and used as received.

2.2.2. Equipment and procedures

Electrolyte preparation

The Fe(III) ligand electrolyte was prepared by dissolving 0.1 M FeCl₃ in a minimum volume of deionised water, 0.5 M of the ligand and 1 M NaCl supporting salt. The pH of each electrolyte was measured using a Toledo pH meter.

Electrochemical measurements

Cyclic voltammograms were performed on a glassy carbon electrode (GC) WE (3mm diameter, BASinc) using a standard 20 mL three electrolyte voltammetry cell (BASinc). A platinum wire (BASinc) served as counter electrode (CE) and Ag/AgCl as the reference electrode (RE). The GC WE was polished using 3µm, 0.25µm, 0.05µm alumina micropolish and polishing pads, then sonicated in deionized water for 10 minutes before use. All voltammograms were recorded using an EmStat³⁺ (Palmsens) and conducted under nitrogen. Preliminary evaluation of electrochemical kinetics were determined from scan rate dependence studies, whereby the electrodes were cycled as a function of multiple scan rates (0.02 - 0.5 Vs⁻¹).

2.3 Fundamental Electrochemical Theory

Electrochemistry is used to investigate reactions involving electron transfers and it is able to relate the flow of electrons to chemical changes. The movement of electrons from one element/metal-ligand complex to another in an electrochemical reaction is known as an oxidation-reduction reaction (redox reaction), in these reactions there is a change in oxidation state of the elements/metal-ligand complexes. Cyclic Voltammetry (CV) is a commonly used technique to investigate the reduction and oxidation processes of the species. The electrochemical cell used in CV investigations has a three-electrode set up which includes a working, counter and reference electrode, the current flows between the working and counter electrodes and the reference electrode is used to measure the applied potential. Voltammograms of redox active species can be recorded by connecting a potentiostat to the electrodes, the voltammograms x axis shows the applied potential (E) whilst the y axis is the resulting current (i) response. For a one electron system there should be two peaks, one corresponding to the oxidation of the species and one corresponding to the reduction of the species, these peaks commonly form a 'duck' shaped voltammogram as seen in Figure 4,⁵² but

the shape of the voltammogram is based on of the type of system whether it be a reversible, quasi-reversible or irreversible process.⁵³

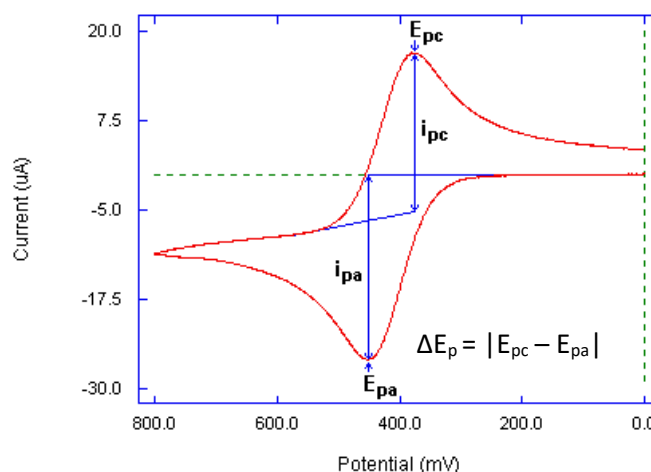


Figure 4 Cyclic Voltammogram showing the 'duck' reversible shape.

A reversible CV is symmetrical such that the ratio of peak currents for the anodic and cathodic processes equal to 1, the peak current ($i_{pc/pa}$) should also increase linearly with the square root of scan rate. The peak potentials ($E_{pc/pa}$) of the cathodic and anodic processes are independent of scan rate in reversible systems and generally the peak to peak separation (ΔE_p) is $57/n$ mV at 25°C .

Irreversible systems require large overpotentials to drive the back reaction and therefore the concentration of the reduced redox active material generated in the forward reaction has diffused away from the electrode before oxidation can take place. It is expected that irreversible CVs therefore show little to no back peak and peak to peak separation is $>120/n$ mV.

Quasi-reversible systems are the intermediate of reversible and irreversible electrode kinetics as a back peak is observed but it is not symmetrical with the forward peak. The peak to peak separation can typically lie between $59/n$ and $120/n$ mV for a quasi-reversible system but the peak separation and peak potentials can increase with scan rate.

2.4 Results and Discussion

2.4.1 Electrochemical evaluation of iron complexes as potential FeRFB catholytes

Ferrocyanide

Ferrocyanide is used frequently in RFB applications due to its high reversibility, stability and low cost.⁵⁴ The ferrocyanide electrolyte contained 1 M NaOH which gave a pH of 13, alkaline conditions were used as ferrocyanide can release toxic cyanide gas at low pHs.⁵⁵ The reported maximum solubility of ferrocyanide is 0.76 M in 1 M NaOH. The overlaid CV scans seen in Figure 5 show a quasi-reversible system with a positive half wave potential of 0.33 V vs Ag/AgCl, the back peak is not symmetrical with the forward peak and there is a difference of 80 mV between anodic and cathodic peaks.

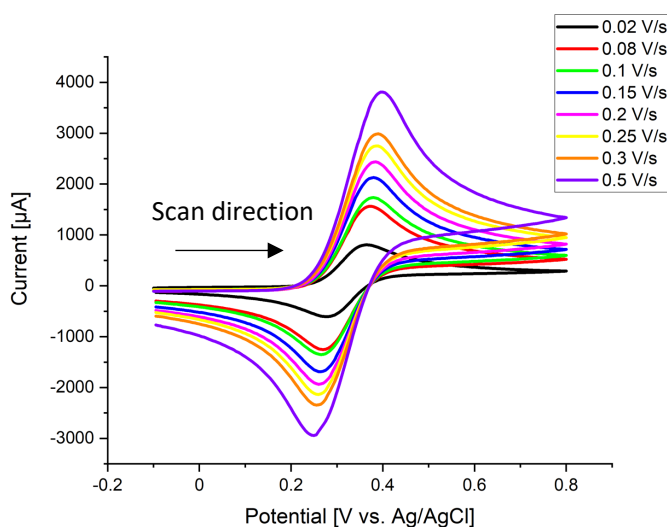


Figure 5 Overlay of cyclic Voltammograms of 0.1 M $K_4Fe(CN)_6$, 1 M NaCl, 1 M NaOH, N_2 atmosphere, pH=14, GC WE, scan rates 0.02 - 0.5 Vs^{-1}

Iron (II) Oxalate

An Fe(II) oxalate complex was investigated as a possible candidate for use in the positive electrolyte as it has a reported redox potential of 0.30 V vs Ag/AgCl and known stable states of Fe(II) to Fe(III).^{56,57} The CV responses shown in Figure 6 suggest the electrochemical redox activity of the complex is poor, however. The Fe(II) oxalate gave an unsymmetrical CV shape with an oxidation peak of 0.47 V vs Ag/AgCl but no clear reduction peak, and as such it was not possible to obtain a formal redox potential. This complex was evaluated at a pH of 7 as in

alkaline pH the oxalate will precipitate out. The results were disappointing, as reversible voltammetry is reported for 0.1 M iron in oxalic acid.⁵⁸

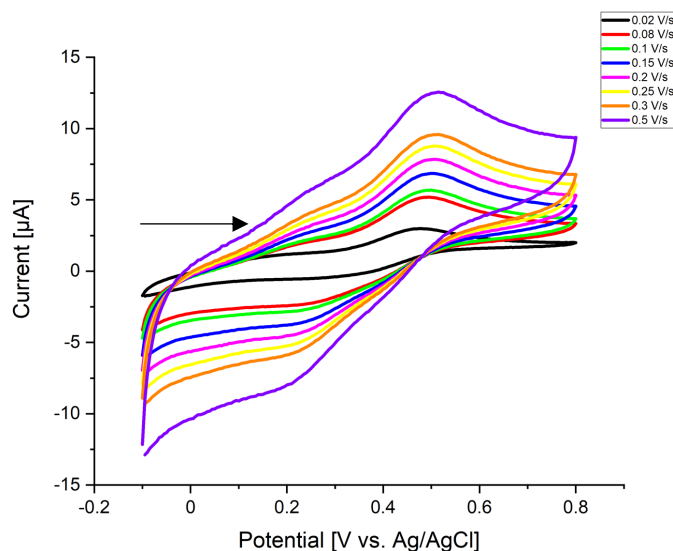


Figure 6 Overlay of cyclic Voltammograms of 0.1 M Fe(II) oxalate, 1 M NaCl, N₂ atmosphere, pH=7, GC WE, scan rates 0.02 - 0.5 Vs⁻¹

Iron (II/III) dimethyl sulfoxide (DMSO)

As both Fe²⁺ and Fe³⁺ oxidation states were present in the electrolyte it was possible to assess the electrolyte as either a positive or negative electrolyte. The Fe DMSO electrolyte gave a redox potential of 0.493 V vs Ag/AgCl with a difference between anodic and cathodic peaks of around 415 mV as seen in Figure 7, the large peak to peak separation suggests that the system is irreversible. The positive redox potential would suggest that the electrolyte would be more suitable as a positive electrolyte but the unsymmetrical shape of the CV makes the electrolyte unsuitable for continuous charging and discharging as seen in a RFB. The pH of the electrolyte was also measured as 2 which would be too acidic for use in a FeRFB. Previous reports using Fe DMSO had synthesised an electrolyte using a larger quantity of ligand (0.8 M) and had achieved a more symmetrical CV shape, however, low pHs < 3 were used which are unsuitable for use in an FeRFB.⁵⁰

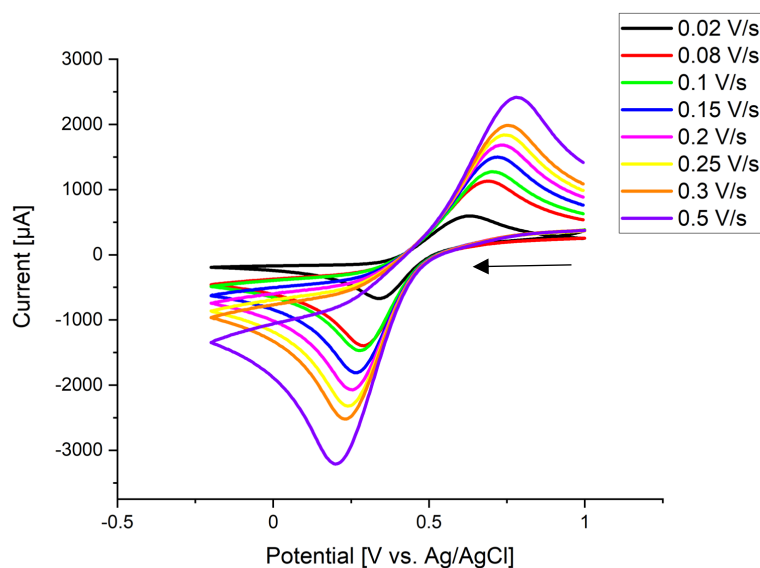


Figure 7 Overlay of cyclic Voltammograms 0.2 M Fe(II/III) DMSO, 1 M NaCl, N₂ atmosphere, pH 2, , GC WE, scan rates 0.02 - 0.5 Vs⁻¹

Iron(III) meso-2,3-Dimercaptosuccinic acid (DMSA)

The novel Fe(III) DMSA complex was investigated as a potential positive electrolyte as the DMSA chelating agent seen in Figure 8a in non-toxic, water soluble and readily available.⁵⁹ The complex gave diffusion limited peak shaped voltammetry with a half wave potential, E° , of 0.49 V vs Ag/AgCl as shown in Figure 8b. The peak-to-peak separation was 365 mV and the waveform was unsymmetrical. This suggests Fe DMSA has slow kinetics and is an irreversible system on the glassy carbon electrode. The pH of the electrolyte was measured as 2.8 which is also slightly too acidic for use in a FeRFB. Although the electrolyte exhibits a good positive redox potential the data obtained from the CV suggests it would be currently unsuitable for a RFB due to the irreversibility of the system but could be improved in the future by optimising pH conditions and supporting salts.

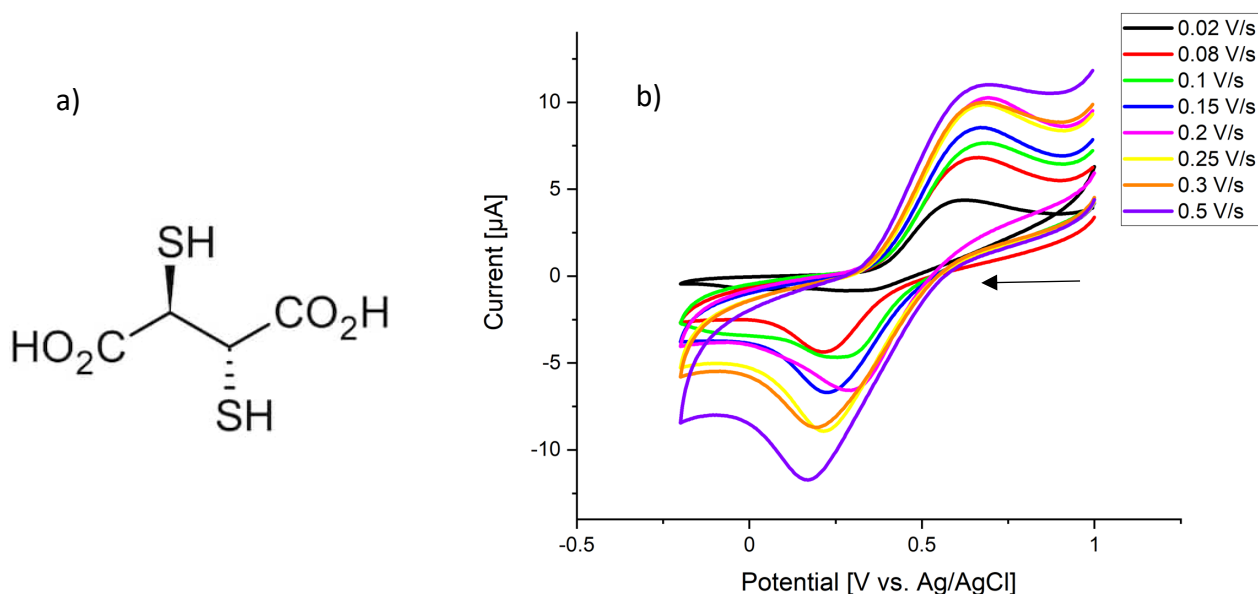


Figure 8. a) Structure of DMSA ligand b) Overlay of cyclic Voltammograms of 0.1 M Fe(III) DMSA, 1 M NaCl, N_2 atmosphere, GC working electrode, GC WE, scan rates 0.02 - 0.5 Vs^{-1}

2.4.2 Electrochemical evaluation of iron complexes as potential FeRFB analytes

Ammonium iron(III) citrate

Iron is well known to form a complex with the citrate ligand to give a distinctive orange. It is this complex that traditionally gave Irn-Bru[®] its vibrant, distinctive colour.⁶⁰ Ammonium Fe(III) citrate complex was evaluated by Hawthorne in 2014 for use in a RFB. It gave a good performance at pH 5.25 with a half wave potential of -0.24 V vs Ag/AgCl, the maximum solubility was reported as 2.45 M which is the best solubility of all screened complexes. Here the electrolyte was prepared by dissolving 0.1 M ammonium Fe(III) citrate salt and 1 M NaCl in deionized water, the pH was altered to 14 by the addition of 1 M NaOH base as the pH of the posolyte and anolyte should be similar to minimise the difference in osmotic pressure and volume change of the electrolyte. From the overlaid CVs we can see a non-symmetrical shape consistent with an irreversible system. The CV shows a clear reduction peak for the reduction of Fe^{3+} to Fe^{2+} , however, there is no oxidation peak for the oxidation of Fe^{2+} to Fe^{3+} at all scan rates, suggesting that the Fe(II)citrate complex has sluggish kinetics or is chemically unstable. The complex is reduced at ca. -0.3 V, which would have been a possible anolyte electrolyte, but the system's irreversibility makes it unsuitable for use as an electrolyte in a RFB. The difference between the results obtained and results in the literature could be due to the altered pH.

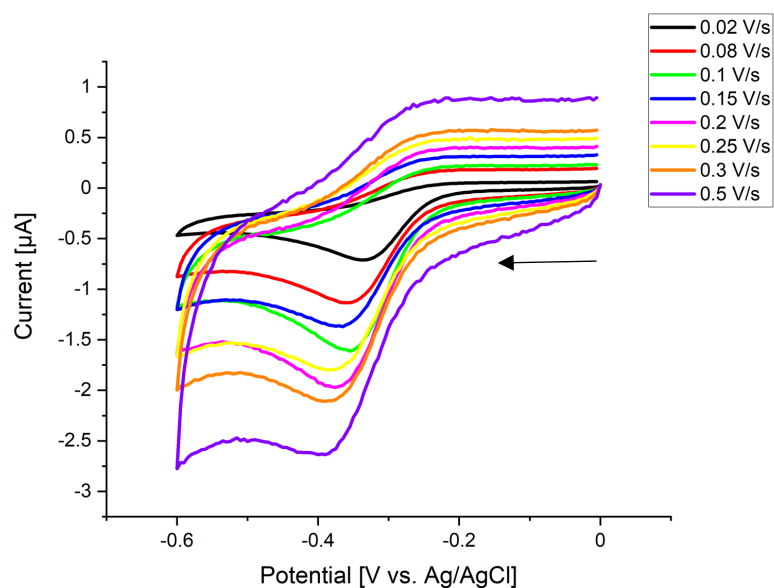


Figure 9. Overlay of cyclic Voltammograms 0.1 M ammonium iron(III) citrate 1M KOH, 1M NaCl, pH 13, N₂ atmosphere, GC WE, scan rates 0.02 - 0.5 Vs⁻¹

Iron(III) diethylenetriaminepentaacetic acid (DTPA)

The Fe(III) DTPA pH was recorded as 14 as the electrolyte contains 1 M NaOH. The CV recorded had a negative redox potential of -0.02 V vs Ag/AgCl and the peak-to-peak separation as 40 mV. This suggests a quasi-reversible system as the front and back peak are not symmetrical and as scan rate increases the ratio of i_{pa}/i_{pc} increases. The electrolyte doesn't exhibit a very negative redox potential, for use in a FeRFB the positive electrolyte would need to have a very positive redox potential to achieve a potential difference of at least 1.0 V between electrolytes. Ibanez et al. used a pH range of 4-10 to achieve a negative redox potential range of -0.124 to -0.215 V vs SCE for Fe(II/III) DTPA.⁴⁴ The difference in the redox potential recorded here can therefore be accounted for by the difference in pH. The pH 14 Fe(III) DTPA electrolyte is therefore not suitable for use as an anolyte in an FeRFB due to its poor negative redox potential. The reported maximum solubility for the complex is 0.1 M which is the poorest solubility of the screened complexes, the solubility of the species effects the maximum concentration and in turn effects the RFB capacity as a lower concentration of redox active species means a lower capacity.

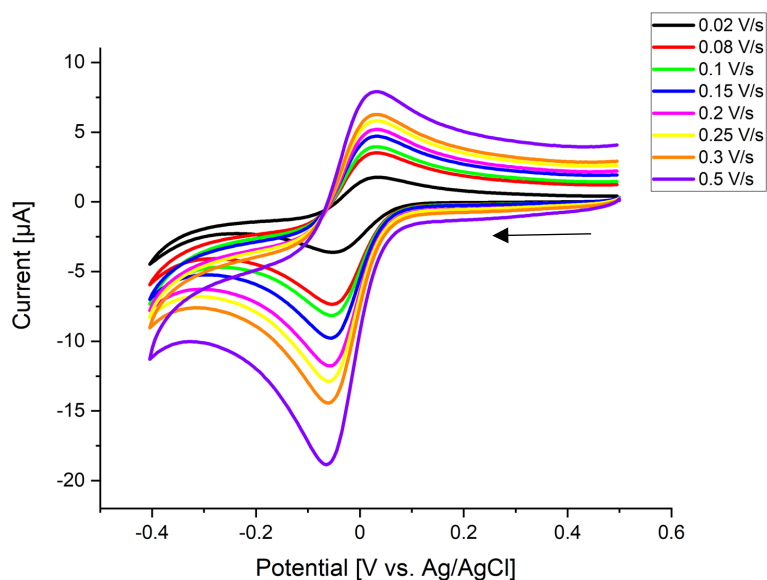


Figure 10. Overlay of cyclic Voltammograms of 0.1 M Fe(III) DTPA, 1 M NaCl, 1 M NaOH, pH=14, N₂ atmosphere, GC WE, scan rates 0.02 - 0.5 Vs⁻¹

Iron (III) triethanolamine (TEA)

The cyclic voltammetry of 0.1 M Fe(III) TEA in 3 M NaOH at pH 14.47 was recorded as a function of scan rate shown in Figure 11. The 3 M NaOH conditions were selected based upon Gong et al. promising Fe TEA RFB results.⁴⁷ The recorded CV shows symmetrical diffusion-limited peaks showing that the system corresponds to a one electron reversible exchange Fe(III/II). A half wave potential of -1.03 V vs Ag/AgCl was obtained with a difference between anodic and cathodic peaks of around 170 mV. The relatively large peak separation would suggest an irreversible system whilst the peak current ratios are > 0.8 and peak-to-peak separation increases with increasing scan rates which suggests a more quasi-reversible system. In the literature the Fe TEA complex is reported as giving one of the most negative redox potentials and a maximum solubility of 0.6 M.⁴⁷

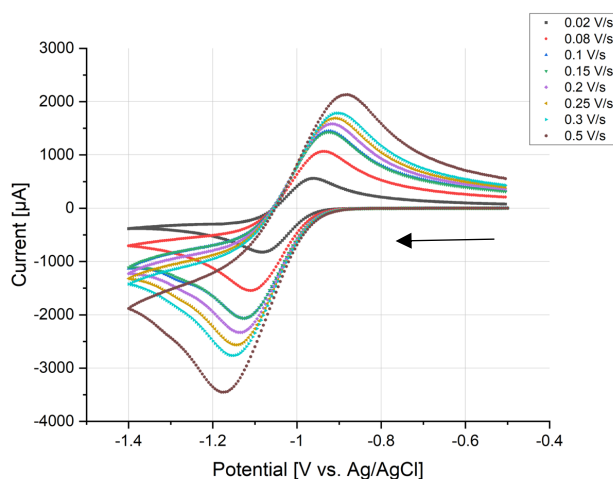


Figure 11. Overlay of cyclic Voltammograms of 0.1 M Fe(III) TEA, 1 M NaCl, 3 M NaOH, pH=14.47, N₂ atmosphere, GC WE, scan rates 0.02 - 0.5 Vs⁻¹

Iron(III) triisopropanolamine (TiPA)

The Fe(III) TiPA electrolyte was prepared with 3 M NaOH as previously done with Fe(III) TEA at pH 14.47. The cyclic voltammetry of 0.1 M Fe(III) TiPA gives symmetrical, diffusion-limited peaks showing that the system corresponds to one electron reversible exchange (FeIII/II) as seen in Figure 12. A negative redox potential of -1.07 V vs Ag/AgCl was obtained with a difference between anodic and cathodic peaks around 75 mV, the difference in peak value suggests a quasi-reversible system but the CV appears very symmetrical and generally $i_{pa} \approx i_{pc}$ which suggests a more reversible system. Fe(III) TiPA has previously been used in Fe-CoRFB applications as the TiPA ligand is readily available, low cost and the complex has a good negative redox potential and a maximum solubility of 0.81 M,⁴⁹ Fe TiPA therefore looks to be a promising choice as a negative electrolyte.

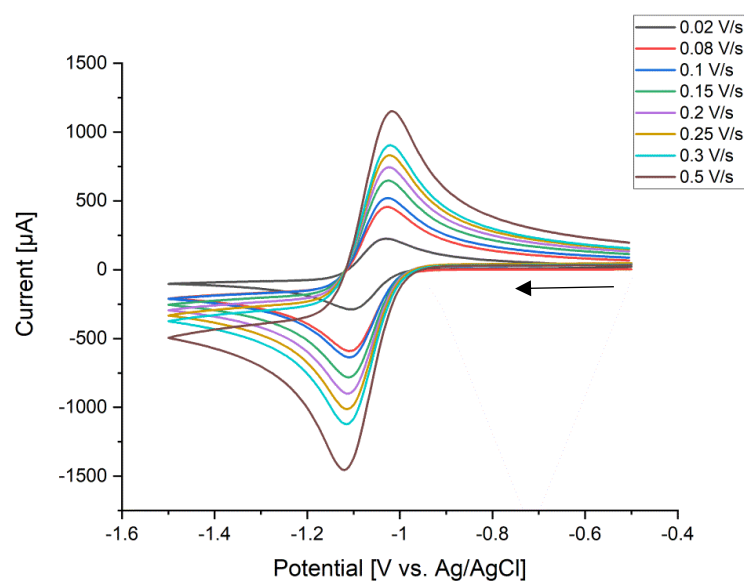


Figure 12 Overlay of cyclic voltammograms of 0.1 M Fe(III) TiPA, 1 M NaCl, 3 M NaOH, pH=14.47, N₂ atmosphere, GC WE, scan rates 0.02 - 0.5 Vs⁻¹

2.5 Conclusions

A range of iron complexes using simple, readily available ligands were evaluated in the context of being used as redox catholytes and anolytes. As seen in table 3 the performance of each electrolyte has been compared.

Iron complex	Redox potential vs Ag/AgCl (V)	ΔE_p (mV)	E_{pa} (V)	E_{pc} (V)	pH	Reported maximum solubility (M)	Citation
K ₄ Fe(CN) ₆	0.33	80	0.36	0.28	14	0.76	40
Fe(II/III) DMSO	0.493	415	0.70	0.295	2	miscible	50
Fe(III) DMSA	0.49	365	0.675	0.30	2.8	-	Novel
Fe(III) Citrate	-	-	-	-0.37	14	2.45	50
Fe(III) DTPA	-0.02	80	0.03	-0.05	14	0.1	44
Fe(III) TEA	-1.03	170	-0.97	-1.09	14.47	0.6	47
Fe(III) TiPA	-1.07	75	-0.98	-1.17	14.47	0.81	49

Table 3. Comparison of the redox potential, ΔE_p , E_{pa} , E_{pc} , electrolyte pH and reported maximum solubilities of the iron complexes.

Of the catholyte candidates, the ferrocyanide couple that is commonly used in aqueous organic redox flow studies was identified as the best candidate. This is because it performed well at pHs over 3 giving quasi reversible voltammetry. The solubility of the complex is said to be highest at $\text{pH} < 12$.⁶¹ In the presence of DMSA and DMSO the iron gave a redox couple of 0.49 V vs Ag/AgCl in solution of roughly pH 2. The complexes were not stable at higher pHs and it is not confirmed if a complex was formed at all for the DMSA solution. While DMSA is a known chelating agent for heavy metal analysis, its voltammetry in an iron complex is not reported. In the interest of saving time ferrocyanide was selected as the catholyte for the RFB experiments as it has been used frequently in RFB applications and the main focus of the screening was to find a suitable anolyte, however, the catholyte of all-FeRFB should be improved in future by increasing ferrocyanide solubility.

Of the anolyte candidates, citrate gave an irreversible reduction response at -0.4 V, with no oxidation peak at pH 14. The DTPA gave a quasi reversible peak-shaped response, but at a moderate potential of -0.02 V vs Ag/AgCl, thus making it unsuitable for the anolyte or catholyte. The best contenders for anolytes were the TEA and TIPA ligands, both of which have been reported in aqueous inorganic flow batteries previously.^{47,49}

The electrolytes selected for the first RFB experiment were ferrocyanide as the catholyte and Fe(III) TEA as the anolyte. The Fe(III) TEA anolyte was selected due to its negative redox potential of -1.03 V vs Ag/AgCl at an alkaline pH which is suitable for pairing with ferrocyanide.

Chapter 3 – Evaluation of an iron(III) triethanolamine and ferrocyanide redox flow battery.

3.1 Background

The results obtained through the screening of multiple iron-ligand complexes suggest triethanolamine (TEA) as one of the best candidates for an all-iron RFB; therefore further studies of Fe(III) TEA were carried out. Triethanolamine is a ligand that can form coordination complexes with transition metal centres. The Fe(III) TEA complex has been reported to exist as a μ -oxo bis(TEA) diiron core where each iron is tetracoordinated by a TEA ligand. The two Fe(III) atoms are bridged by one oxygen atom and have a bipyramidal coordination geometry.⁶² As discussed in Chapter 1 and 2, Fe(III) TEA has previously been used in RFB applications.⁴⁷ Fe TEA exhibits a good negative redox potential of -1.03 V which makes it a good contender to use in an all-iron RFB with ferrocyanide as the potential difference is 1.36 V. Gong et al. suggested an all-soluble all-iron RFB constructed by combining an iron-triethanolamine redox pair (i.e. $[\text{Fe}(\text{TEA})\text{OH}]^-/[\text{Fe}(\text{TEA})(\text{OH})]^{2-}$) and an iron-cyanide redox pair (i.e. $\text{Fe}(\text{CN})_6^{3-}/\text{Fe}(\text{CN})_6^{4-}$) and suggested the main reason for capacity loss during battery cycling was due to the TEA ligand crossover through the Nafion membrane.⁴⁷ An investigation in to optimizing this set up by more comprehensively assessing the battery performance with two membranes to mitigate crossover of the TEA ligand was carried out. Crossover studies were performed to assess the crossover hypothesis suggested by Gong et al. Finally, a stability study to confirm degradation of the Fe(III) TEA complex through symmetrical cycling was carried out.

3.2 Experimental

3.2.1 Materials and Reagents

Triethanolamine (99%, Sigma Aldrich), Iron(III) chloride hexahydrate (98%, reagent grade), Sodium Chloride (99%, ACS reagent) and Sodium hydroxide (98%, BioXtra) were purchased and used as received.

3.2.2. Electrolyte preparation

Electrolytes were prepared by dissolving $\text{FeCl}_3 \cdot 6\text{H}_2\text{O}$ (2.7 g, 0.01 mol) in deionized water followed by triethanolamine (6.6 mL, 0.05 mol), NaOH (12 g, 0.3 mol) and NaCl (5.84 g, 0.1 mol) and the volume made up to 100 mL. Precipitation was observed during the preparation of the electrolytes which re-dissolved as the electrolytes were stored under nitrogen for 3 days and shaken daily until a clear purple solution could be seen. The pH was calculated as 14.47. This was to ensure no precipitation of $\text{Fe}(\text{OH})_3$ and as $\text{K}_4\text{Fe}(\text{CN})_6$ has been chosen as the positive electrolyte the same pH is desirable for the negative electrolyte to avoid diffusion of water over the membrane. The pH of the electrolytes was recorded during electrolyte preparation, before cyclic voltammetry (when the solution had come to equilibrium) and after CV evaluations. During battery cycling the pH of the electrolytes were measured before and after the cycling using a glass pH meter.

3.2.3 Iron(III) triethanolamine synthesis

Iron (III) triethanolamine synthesis was reproduced as per a literature procedure from Le at al.⁶² In the procedure $\text{FeCl}_3 \cdot 6\text{H}_2\text{O}$ (5.6 g, 20 mmol) was dissolved in 10 mL deionized water with N_2 purging. Triethanolamine was then added (3.8 g, 26 mmol) and after 10 minutes stirring an excess of KOH (5.6 g, 140 mmol) was added. The solution was filtered under vacuum to remove any solids then the filtrate was diluted with deionised water was evaluated using CV. Due to poor CV results and in the interest of saving time no further characterisation of the synthesised sample was done. Due to lack of characterisation we are unable to confirm if the sample was pure and if there were any impurities present, this could in turn have had an effect on the observed CV results.

3.2.4 Electrochemical cell

The performance of a RFB is highly dependent on the design of the flow-cell, therefore cell engineering and optimisation is critical in achieving high current densities and power output from the battery.⁶³ The current density can be improved by a steady flow of electrolyte, this enables more reactions to occur at the surface of the electrode. The power density determines the electrochemical cell size required to achieve a given output, increasing the surface area of the electrodes can increase the cells current at a given current density which delivers more power. To avoid disintegration and contamination, the appropriate materials must also be

used. In this project, alkaline aqueous electrolytes at roughly pH 14 are used as $K_4Fe(CN)_6$ is present in the positive electrolyte. All materials in contact with the electrolytes should therefore be highly chemically resistant.⁶⁴

In this section the different components used in the RFBs will be discussed.

Flow Cell

A replica of the Brushett 'Gen2' flow cell,⁶⁵ as seen in Figure 13, was used to carry out charge-discharge studies. The flow cell is comprised of cell bodies made of polypropylene (PP) which encase the flow-field current collectors made of ppg-86 graphite-PP composite. Two types of gasket materials are used in the cell, polytetrafluoroethylene (PTFE) plastic and ethylene-propylene diene monomer (EPDM) rubber, both highly chemically resistant. The EPDM gaskets are used to seal the cell to ensure no leakage whilst the PTFE gaskets are used to ensure electrical insulation between the half cells. Carbon felts were used as the electrode material (13x15 mm). The electrolytes were pumped between the reservoirs and the flow-cell by tubing lines constructed of perfluoroalkoxy alkane (PFA) and Norprene peristaltic pump tubing, both with a 1.6 mm internal diameter. The battery electrolytes were stored in 20 mL glass vials which were placed in 100 mL glass bottles under nitrogen. The lids of the glass bottles had 3 inlet/outlets, one of the outlets was used to pump the electrolyte from the reservoir to the flow cell whilst another was used for the electrolyte being pumped out of the flow cell back to the reservoir. The final inlet/outlet was used to keep the system under Nitrogen. This type of flow cell enables different flow-field current collector patterns to be used to vary the electrolyte flow through the carbon felt electrodes. The flow through flow-field (PTFF) current collector was selected for use in this research as its design forces all of the electrolyte to pass through the electrode material which improves mass transport and decreases cell resistance.⁶⁶

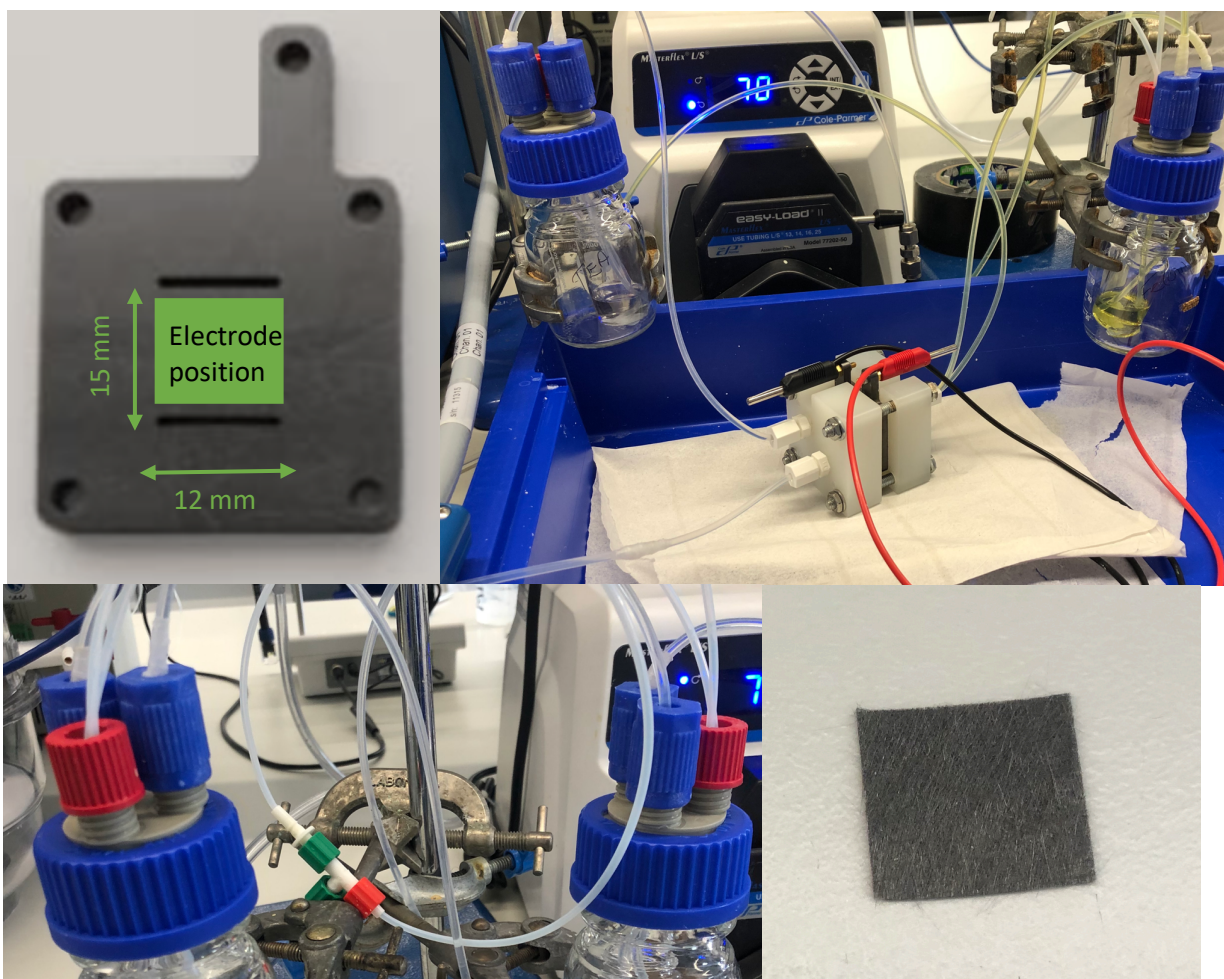


Figure 13 Gen 2 Flow-cell design. Top left) ppg-86 graphite flow through flow-field (FTFF) current collector. Top right) Assembled Flow-cell and electrolyte reservoirs. Bottom left) Electrolyte reservoir lids with 3 inlet/outlets. Bottom right) Carbon paper electrode

Electrode materials

Electrode materials for RFBs are typically carbon-based materials such as carbon felt, carbon cloth or graphite felts. The requirements for a good electrode material include high chemical stability in the electrolyte, high surface area, low electrical resistivity and a wide operating potential range.⁶⁷ In this research, carbon paper (A20301 'carbon mat', Technical Fibre Products, 13 x 16 x 0.5 mm dimensions) material was used as electrodes for the flow cell. Carbon paper was chosen as the electrode material as they are low cost and provide a high surface area to maximise current densities. The electrode material was studied by scanning electron microscopy (SEM) and energy dispersive X-ray spectroscopy (EDX) to examine its structure.

The SEM analysis showed the carbon paper material is composed of long inflexible fibres in a somewhat random orientation which are bound together with a binder substance which coheres the macrostructure. The electrode was studied by EDX which showed the fibres were composed of carbon (76.4 %) and on inspection of the binder substance it showed a high amount of oxygen present (23%). This was consistent with previous inspections of the carbon felts used which stated the binder is composed of polyvinyl alcohol (PVA) plastic and a high abundance of oxygen is to be expected (Appendix A).⁶⁸

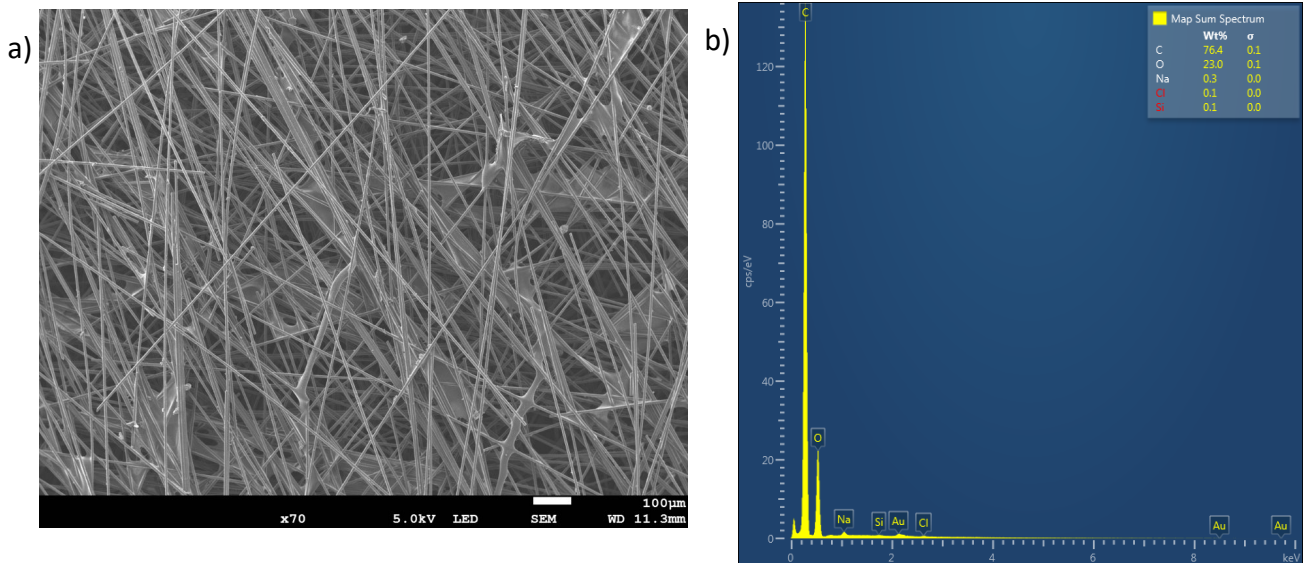


Figure 14 a) SEM image of the carbon paper electrode. 100 µm scale b) Elemental analysis through EDX analysis.

Membranes

The ion selective membrane is an essential component of a RFB. The membrane serves to prevent the anolyte and catholyte from mixing during operation while allowing selective ions pass through it.⁶⁹ Additionally, the membrane must be chemically resistant and inert in the applied battery electrolyte, durable and cost effective.

Membranes are usually made up of cross-linked linear polymer chains that form a three-dimensional network. One of the most commonly used membranes in iron RFB applications is Nafion which is formed of perfluorosulfonic acid polymers.⁷⁰ Nafion's structure consists of perfluorovinyl ether groups terminated with sulfonate groups which ensure ionic conductivity, these are attached to the hydrophobic Teflon backbone which provides mechanical and chemical stability. In this research Nafion-117 is used as well as the novel

benzyltrimethylammonium(TMA) (TMA=trimethylamine) anion exchange membrane (AEM) which will be referred to as BTMA during this work. The BTMA membrane was made by J. Ponce-Gonzalez at The University of Surrey, the method used was similar to that reported in previous work⁷¹ of immersing 50 micron thick poly(ethylene-co-tetrafluoroethylene) (ETFE) films in an aqueous solution of the amine. The membrane has a thickness of 0.10 mm and an ion-exchange capacity of 1.820 meq g⁻¹ compared to the 0.18 mm thickness and ≥ 0.9 meq g⁻¹ ion-exchange capacity of Nafion-117. The increased thickness of the Nafion-117 membrane may help avoid crossover but could lead to increased resistance whereas the ion-exchange capacity of Nafion-117 is smaller than that of BTMA. A high ion exchange capacity allows more ions to pass through the membrane but the membrane must remain ion selective otherwise it could lead to crossover of species.⁷²

The membranes were soaked for 72 hours in Fe TEA for K₄Fe(CN)₆/ Fe(III)TEA charge-discharge studies and rinsed with deionised water before use in the flow cell.

Peristaltic pump calibrations

A digital peristaltic pump was used to pump the electrolytes through the flow cell. To get optimal flow rate for the system the peristaltic pump was calibrated by measuring the time taken to dispense 20 ml of supporting electrolyte (1 M NaCl, 3 M NaOH) as a function of rotation per minute (RPM). As seen in Figure 15, a correlating liner relationship ($R^2= 0.998$) was achieved and used to set a specific flow-rate. A flow-rate of 20 mL min⁻¹ was used in the flow cell as battery electrolytes were typically 10 mL and this would allow the complete circulation of the electrolyte every 30 seconds. At higher flow-rates leakage of electrolytes can become problematic due to increased electrolyte pressure on the flow-cell seals and gaskets. The supporting electrolyte was used in the calibration as the flow-rate is dependent on the solutions properties e.g. viscosity and temperature, it was assumed that the supporting electrolyte would have approximately the same viscosity as the redox active electrolytes.

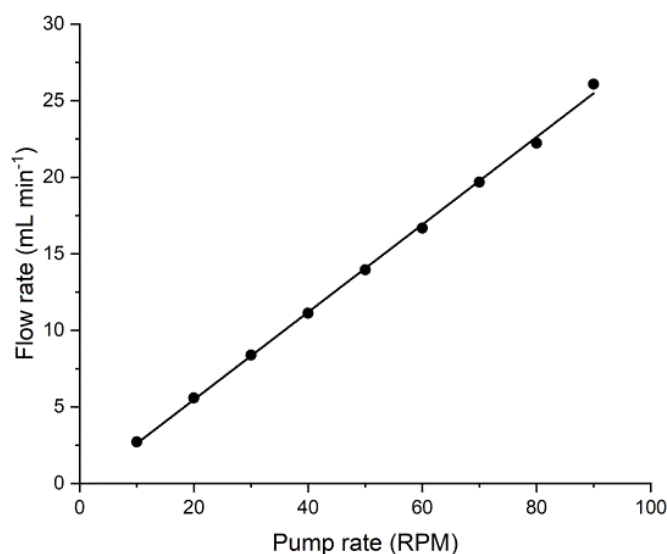


Figure 15 Peristaltic pump calibration for the flow-rate as a function of RPM. Norprene tubing and supporting electrolyte used (1M NaCl, 3M NaCl). Each data point representing the mean flow-rate, averaged over three measurements.

3.3 Results and Discussion

3.3.1 Electrochemical evaluation of Iron(III) TEA

Beyond the provisional screening study in Chapter 2, voltametric methods were performed on the Fe(III) TEA electrolyte to investigate the fundamental electrochemical properties and assess its suitability in an all-iron RFB. The electrochemical behaviour of non-synthesised Fe(III) TEA electrolyte was investigated initially by CV, the results of which were given in Figure 11. A Randles-Sevcik analysis of the CVs taken at multiple scan rates can be seen in Figure 16b and Figure 16a is the CV of the Fe(III) TEA electrolyte (0.1 M Fe(III) TEA, 0.1 M NaCl, 3 M NaOH) and the blank electrolyte (1 M NaCl, 3 M NaOH, 0.5 M TEA) which shows that the Fe(III) TEA CV resides well in the electrolyte stability region.

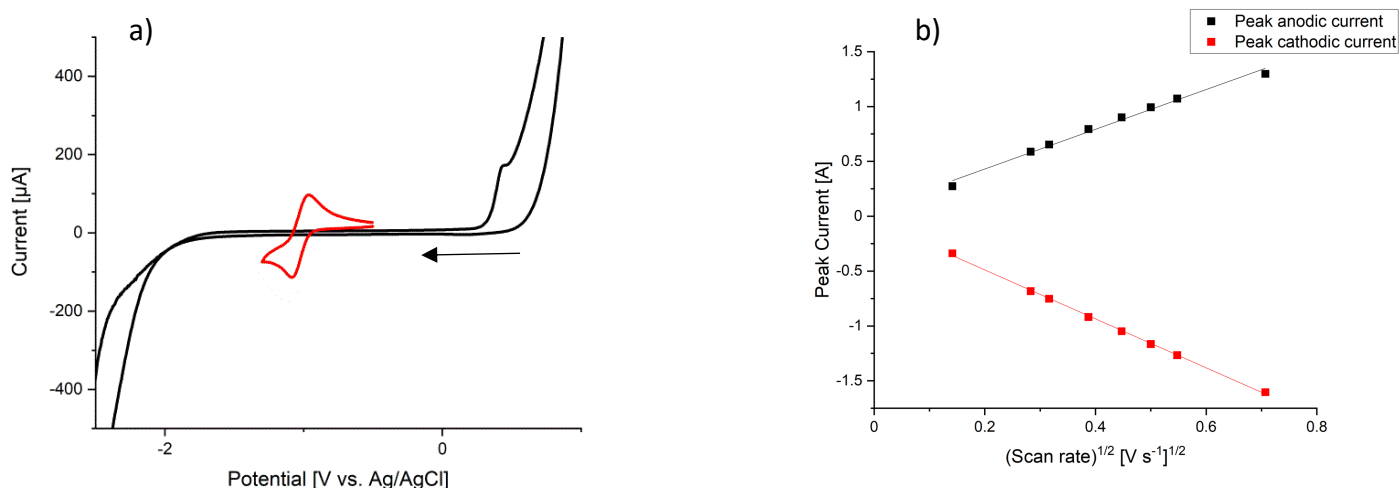


Figure 16 a) Cyclic Voltammetry of the blank electrolyte and Fe(III) TEA, 1M NaCl, 3 M NaOH, pH=14.47, N₂ atmosphere, GC WE, scan rate 0.1 Vs⁻¹ b) Randles-Sevcik analysis of the scan rate dependence study shown in Figure 11.

From the cyclic voltammograms the peak current from both anodic and cathodic peaks were analysed by Randles-Sevcik analysis at scan-rates $\leq 500 \text{ mV s}^{-1}$ to give a linear dependency on the square root of scan rate. The Randles-Sevcik equation for a reversible system is given by **Equation 1**, where I_p is the peak current, n is the number of electrons in the process, A is the electrode area, C_{bulk} is the bulk concentration of the species of interest, D is the diffusion coefficient and v is the scan rate.⁷³

$$I_p = (2.69 \times 10^5) n^{3/2} A C_{\text{bulk}} D^{1/2} v^{1/2} \quad \text{Eq. 1}$$

Assuming that the Randles-Sevcik equation for a reversible system is valid the diffusion coefficient for the oxidation of Fe(III) TEA was calculated as $1.2 \times 10^{-6} \text{ cm}^2 \text{ s}^{-1}$.

Rotating disk electrode (RDE) liner sweep voltammograms were collected using an RRDE-3A apparatus (ALS Co.), 100 mL voltammetry cell with the three electrodes used in previous experiments. The RDE introduces mechanical convection to the system such that the currents response of the electrochemical reaction can be related to the mass transport via convection and diffusion.⁶⁸ Koutecky-Levich analysis was carried out on the Fe TEA as shown in Figure 17 to further confirm mass transport and kinetic information. Liner sweep voltammetry (LSV) as a function of rotation rate gave limiting current plateaus at overpotentials of $>1.2 \text{ V}$. The analysis of region 1 to 1.4 V overpotential gave somewhat non-linear responses of the inverse current against inverse square-root of rotation rate. A linear relationship is expected for the

Koutecky-Levich analysis as a function of rotation rate, the nonlinear results from the data collected could be due to using a small volume of electrolyte (<100 mL), equipment failure or lack of repeats. The corresponding standard electrochemical rate constant of $4.2 \times 10^{-4} \text{ cm s}^{-1}$ and a transfer coefficient of 0.48 was calculated.

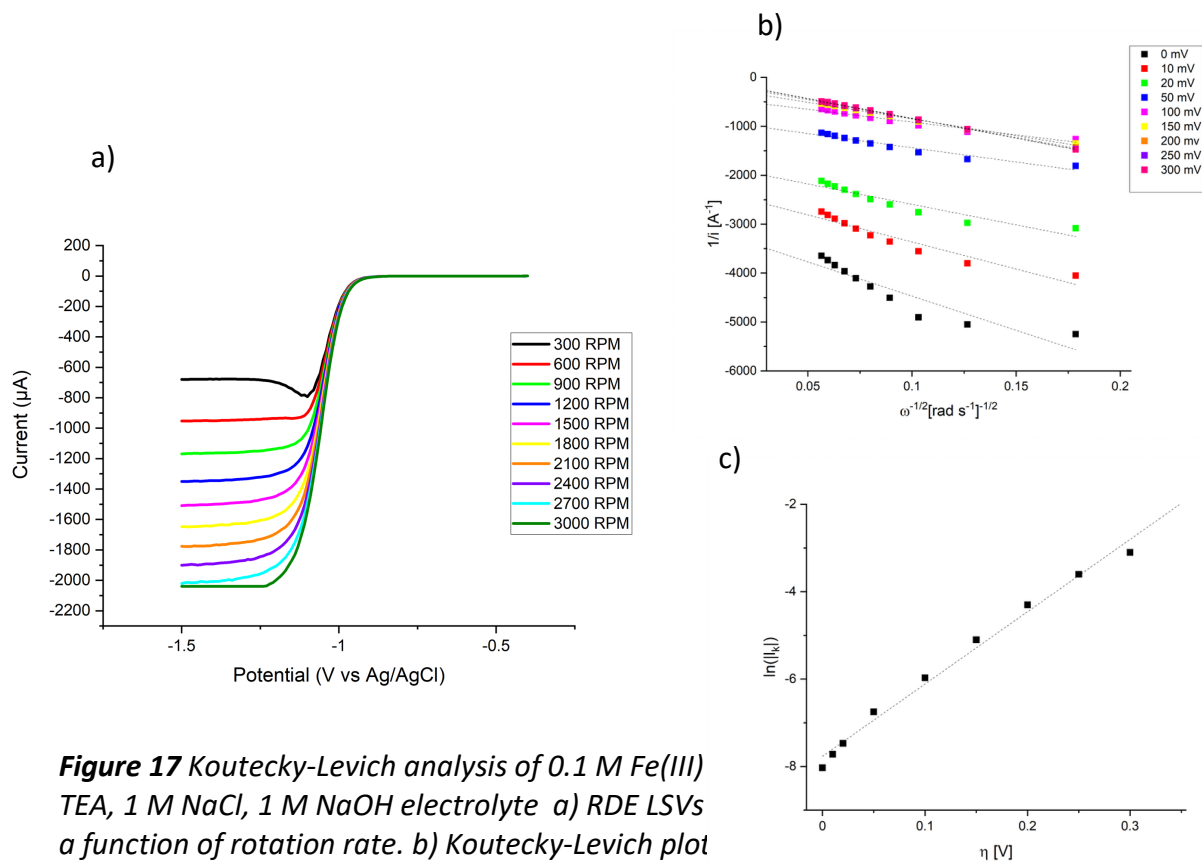


Figure 17 Koutecky-Levich analysis of 0.1 M Fe(III) TEA, 1 M NaCl, 1 M NaOH electrolyte a) RDE LSVs a function of rotation rate. b) Koutecky-Levich plot as a function of overpotential. c) plot of the logarithm of the kinetically limited current against overpotential.

The electrochemical behaviour of a synthesised Fe(III) TEA complex was also investigated at a scan rate of 0.1 Vs^{-1} as seen in Figure 18. Again, a negative redox potential of $-1.05 \text{ V vs Ag/AgCl}$ was obtained but a larger difference between anodic and cathodic peaks of 340 mV was seen. The synthesised Fe(III) TEA cyclic voltammogram peaks were less pronounced compared to the non-synthesised electrolyte. The peak separation is double that of the unsynthesised Fe(III) TEA electrolyte which proves that the synthesised redox active material is less stable than un-synthesised, this also suggests the system is irreversible and likely undergoing a secondary chemical step when in the reduced state. However, Le at al. synthesised Fe TEA and achieved a reversible system with a peak separation of 70 mV, the discrepancies between our values could be due to use of a different initial iron salt. Fe(III) sulphate was reported as their

initial iron salt whereas Fe(III) chloride was used as the initial iron salt in this work. Sulphate could be more easily displaced by the TEA ligands and form a more stable structure.^{62,49}

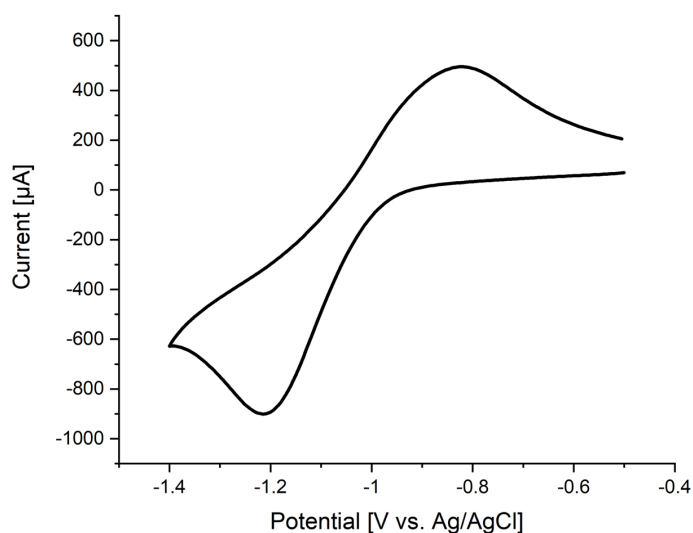


Figure 18 Cyclic Voltammetry of synthesised 0.1 M Fe(III) TEA at 0.1 Vs⁻¹. 1M NaCl, 3 M NaOH, pH=14.47, N₂ atmosphere, GC WE First scan shown.

As Fe(III) TEA electrolyte is easily prepared and has a suitable negative redox potential of -1.03 V it is promising for use with K₄Fe(CN)₆ which has a positive redox potential of 0.33 V in KOH in a RFB to create a potential difference of 1.36 V. A charge-discharge study using K₄Fe(CN)₆ and Fe(III)TEA was therefore carried out and its performance investigated.

3.3.2 UV-Vis measurements and solubility study

The UV-Vis spectra of the Fe(III) Triethanolamine electrolytes were recorded by an Agilent Cary 60 spectrophotometer using a 1 mm path length cuvettes (Starna scientific). The solubilities of the Fe(III) TEA electrolyte were measured by a UV-Vis method by first acquiring calibration spectra at 0.1 M and 0.2 M concentrations. A UV-Vis spectra of a 1/10 dilution of 0.5 M concentration was recorded. A Beer-Lambert calibration plot was then produced based upon the absorbance ($\lambda = 596 \text{ nm}$) at the UV-Vis peak as seen in Figure 19a. The diluted 0.5 M concentration point sits above the line of best fit which confirms that the Fe TEA is soluble at this concentration which is supported by previous reports of a 0.6 M solubility limit in 3 M NaOH.⁵⁰ A 1.0 M concentration electrolyte was prepared but the salts were insoluble at such

high concentration, therefore UV-Vis of the electrolyte wasn't possible and the calibration plot of the Fe(III) TEA solubility was based on the three soluble concentrations.

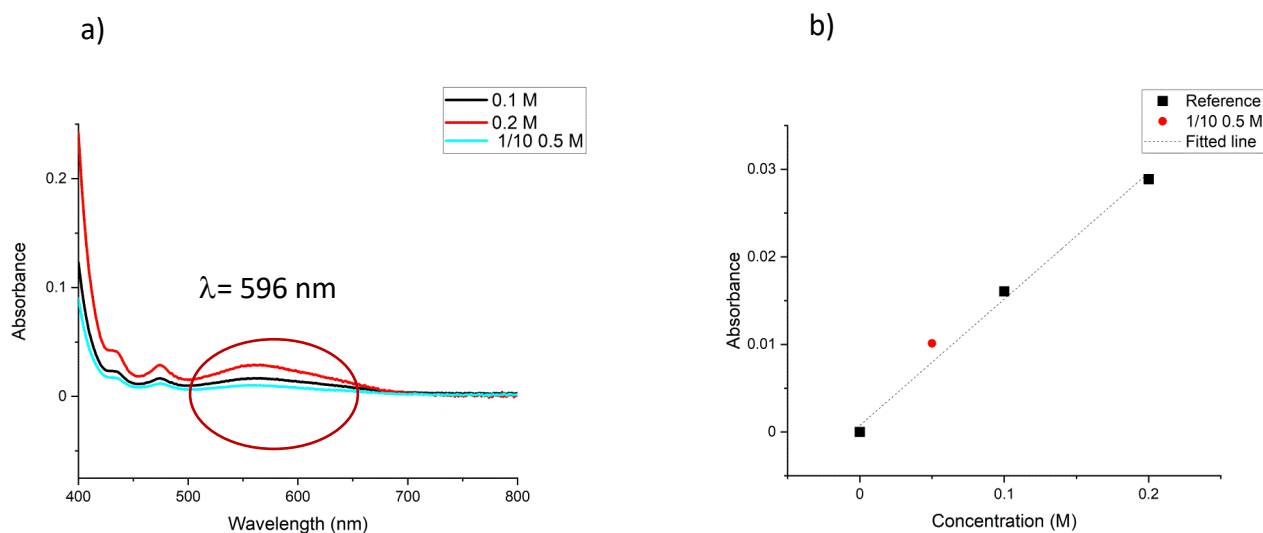
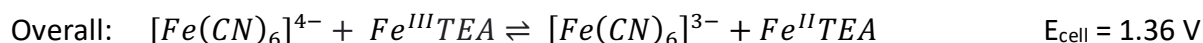
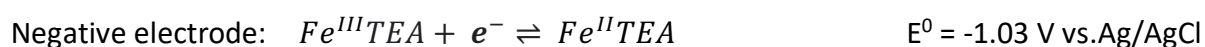


Figure 19 a) UV-Vis spectrum of 0.1 M, 0.2 M and 1/10 diluted 0.5 M concentration of Fe(III) TEA b) Calibration of Fe(III) TEA solubility

3.3.3 Charge-discharge studies of $K_4Fe(CN)_6$ & Fe(III) TEA

Charge-discharge studies were conducted using $K_4Fe(CN)_6$ as the redox active material in the positive electrolyte and Fe(III)TEA in the negative electrolyte. This study uses only one redox material, iron, and two oxidation states, Fe(II) and Fe(III), meaning the oxidation of the $K_4Fe(CN)_6$ in one electrolyte can be coupled to the reduction of Fe(III)TEA in the other electrolyte. The electrolytes are reversibly converted from 0-100% SOC by repeatedly charging and discharging the cell. The cell allows battery properties, such as redox material stability, to be investigated easily. The corresponding redox reactions and electrode potentials are shown by the following equations.



The charge-discharge of the redox couple was assessed using two different membranes- Nafion-117, and BTMA. Nafion-117 is used frequently in RFB applications whereas the novel BTMA membrane is being investigated in this work to assess its suitability for use in RFBs. The initial charge-discharge study of the all-soluble all-Fe RFB was with 10 mL $K_4Fe(CN)_6$ positive electrolyte and 10 mL Fe(III) TEA negative electrolyte which were stored in separate reservoirs. The electrolyte reservoirs and the flow cell were connected by tubing and the electrolyte was circulated at a flow rate of 20 mL/min. The first membrane assessed in this set up was Nafion-117, a 5 mA cm^{-2} current density was used for the charge-discharge cycling, the charge-discharge response was recorded for each cycle and is shown in Figure 20.

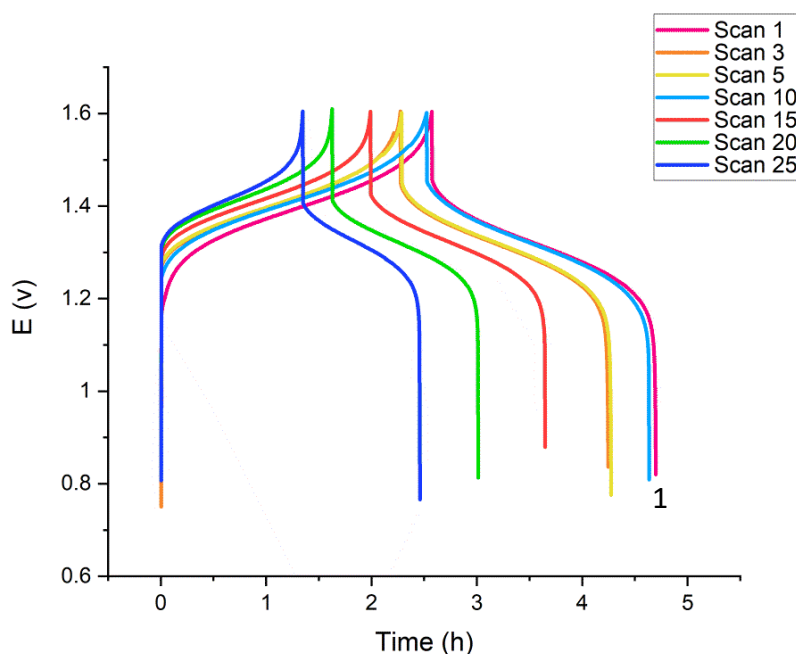


Figure 20 Charge-discharge curves of the $0.1\text{ M } K_4Fe(CN)_6 / 0.1\text{ M } Fe(III)\text{ TEA}$ battery with Nafion-117 membrane at 5 mA cm^{-2} between 1.6 and 0.9 V upper and lower potential thresholds in the flow cell.

The theoretical capacity can be calculated for Equation 2, where $Conc$ is the concentration of the redox active material, z is moles of electrons involved in charge or discharge reaction and F is the Faraday constant.

$$\text{Theoretical capacity (Ah L}^{-1}\text{)} = \frac{Conc \times z \times F}{2 \times 3600} \quad \text{Eq. 2}$$

The theoretical capacity of the system is 2.68 Ah L^{-1} , as 10 mL electrolyte was used the theoretical capacity the system can achieve in the experiment is 26.8 mA h. The time taken to complete a full charge-discharge at the theoretical capacity would be 5.36 h. In the first charge cycle the system achieved a capacity of 25.7 mA h which is 96% relative capacity to the theoretical. From Figure 20 it can be seen that as cycle number increased the time to charge and discharge the system decreases, this is due to a capacity loss over time. From cycle 1 to cycle 25 the capacity decreased from 25.7 mA h to 13 mA h, a 49.4% capacity fade. Capacity loss is to be expected over time in systems such as this, in a previous example of this system the capacity initially decreased and then became stable after 20 cycles, 110 cycles were recorded, however, volumes of electrolyte were not stated.⁴⁷ Generally, the Columbic efficiency remains above 83% whilst Voltaic efficiency remains above 79% and the Energy efficiency above 66% across the 25 cycles, as shown in Figure 21b, these values are consistent with the energy values given by Gong et al.⁴⁷

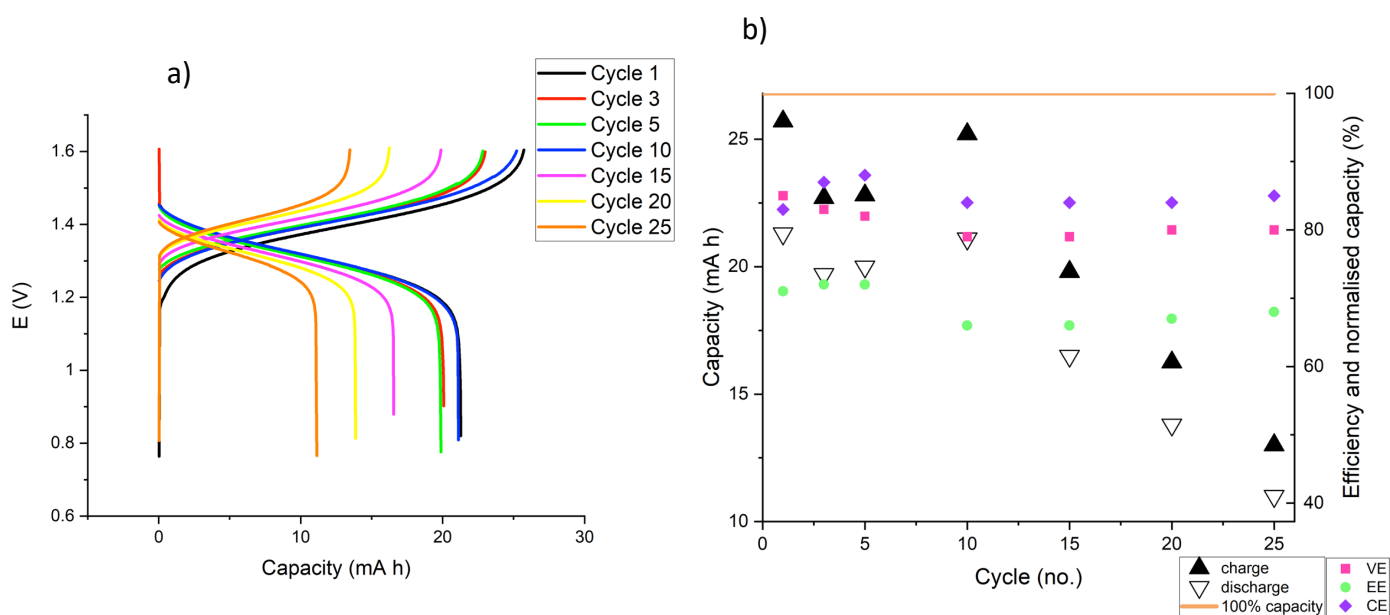


Figure 21 a) Evolution of charge-discharge curves as a function of capacity. b) Charge-discharge capacities and efficiencies as a function of cycle number. (Nafion 117 membrane)

After the charge-discharge studies the electrolytes were studied by cyclic voltammetry again. In Figure 22 the height on the cathodic and anodic peaks after battery cycling had decreased, implying a loss in the concentration of redox active material. Assuming the Randles-Sevcik equation (Eq. 1) is valid the loss is calculated to be 50%. The carbon paper electrodes were investigated by SEM and EDX analysis as they were suspected to be responsible for the

concentration decrease as previous all-aqueous RFB had reported the redox active material becoming deposited on the electrode material.⁴⁹ The wet carbon paper electrodes were dried at 80 °C for 6 hours under vacuum to remove moisture before SEM and EDX analysis.

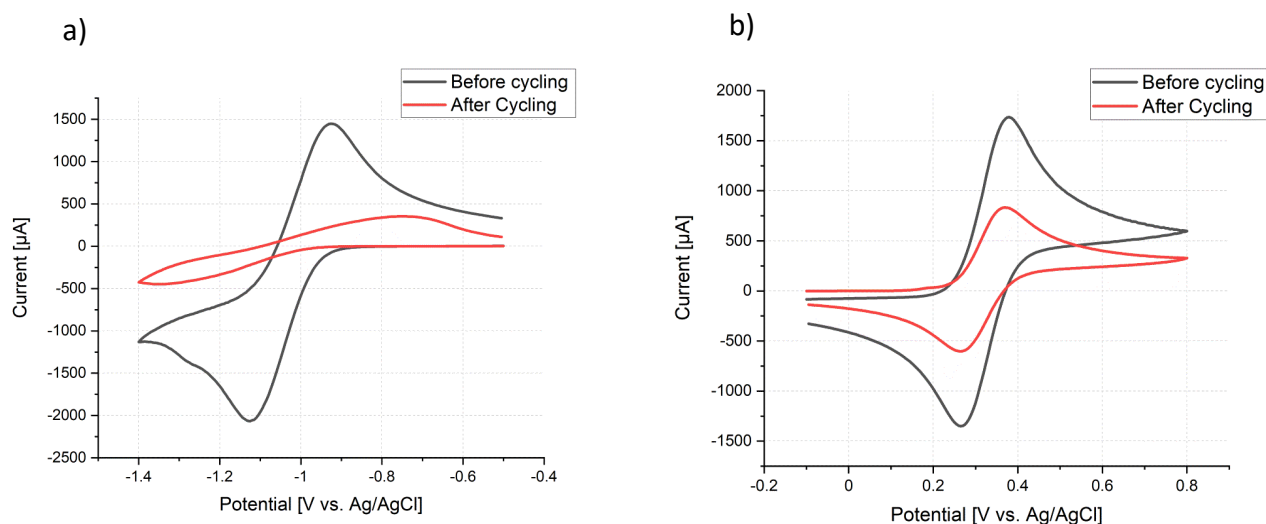


Figure 22 a) Cyclic voltammetry of Fe(III) TEA before and after charge-discharge studies at 0.1 Vs^{-1} b) Cyclic voltammetry of $\text{K}_4\text{Fe}(\text{CN})_6$ before and after charge-discharge studies at 0.1 Vs^{-1} .

The SEM images of the used carbon felt electrodes for $\text{K}_4\text{Fe}(\text{CN})_6$ and Fe(III)TEA electrolytes can be seen in Figure 23. Upon inspection a small amount of salt can be seen deposited on the fibres of the carbon felt, EDX analysis (Appendix B) confirmed the presence of iron in both electrode material, 0.4 % Fe in $\text{K}_4\text{Fe}(\text{CN})_6$ electrode and 0.1 % Fe in Fe(III) TEA electrode as well as a 4.4 % of Na in $\text{K}_4\text{Fe}(\text{CN})_6$ electrode and 5.7 % Fe in Fe(III) TEA electrode.

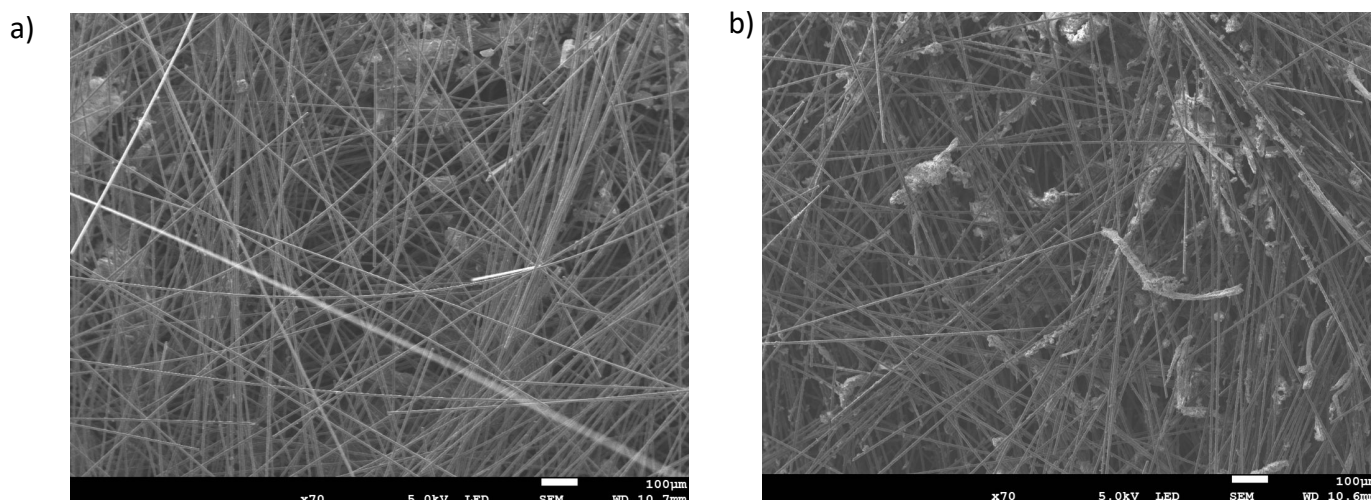


Figure 23 a) SEM image of the carbon paper electrode used in $\text{K}_4\text{Fe}(\text{CN})_6$ electrolyte. $100 \mu\text{m}$ scale b) SEM image of the carbon paper electrode used in Fe(III) TEA electrolyte. $100 \mu\text{m}$ scale.

Another possible explanation for the loss of iron concentration is iron oxide depositing in the tubing between the reservoirs and the flow cell. After a few days of continuous charge-discharge cycling an orange/brown layer could be seen inside the tubing which seemed to be iron depositing, this was likely due to oxygen entering the system. In order to minimise this effect extra precautions were taken to ensure the system was gas tight and would remain under nitrogen at all times.

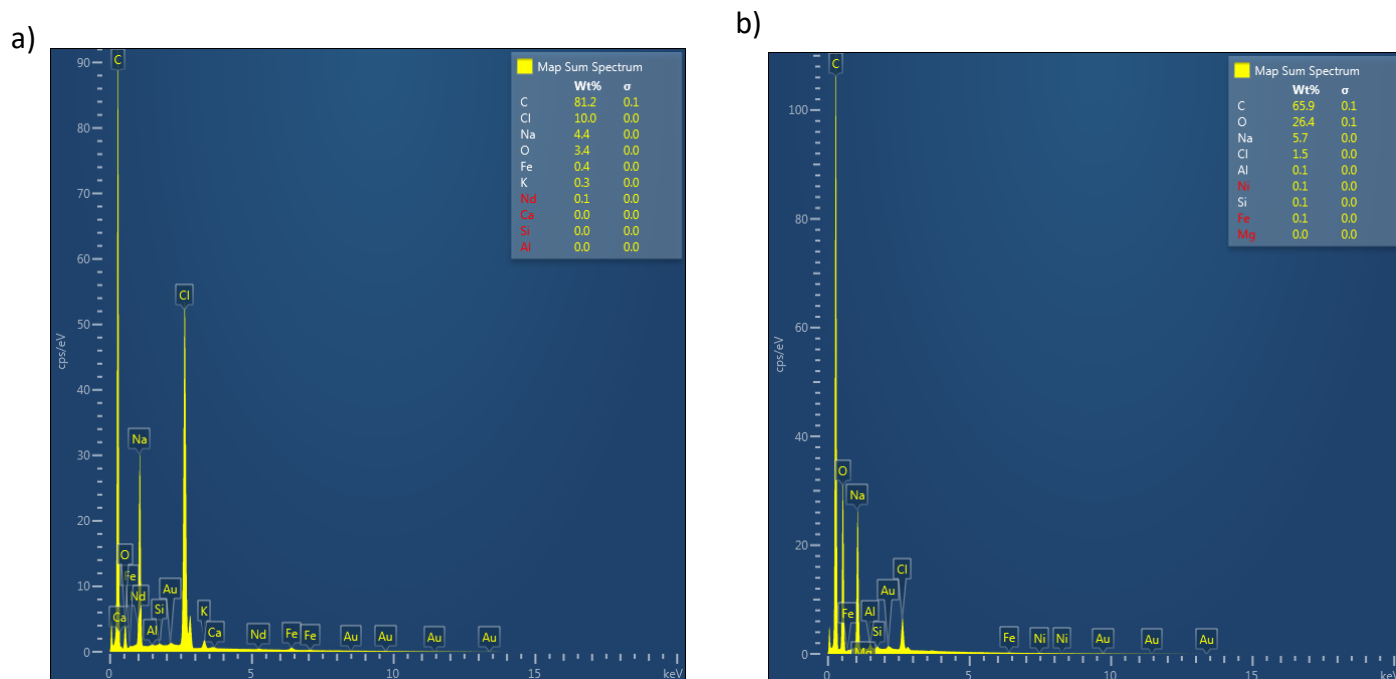


Figure 24 Elemental analysis through EDX analysis of a) $K_4Fe(CN)_6$ electrolyte b) Fe(III) TEA electrolyte

The flow cell experiment containing $K_4Fe(CN)_6$ and Fe(III) TEA electrolytes was also carried out with the Cationic BTMA membrane. The cell was assembled and the charge-discharge study was conducted using 10 mL $K_4Fe(CN)_6$ positive electrolyte and 10 mL Fe(III) TEA negative electrolyte which were stored in separate reservoirs. The electrolyte reservoirs and the flow cell were connected by tubing and the electrolyte was circulated at a flow rate of 20 mL/min and the cycling took place at 5 mA cm^{-2} current density. As seen in Figure 25 the capacity loss using this membrane is much quicker than that of the Nafion-117. The capacity of charge 1 was 26.3 mA h which is 98% relative capacity to the theoretical, by cycle 25 the capacity decreased to 2.5 mA h, which is a 90.5% capacity loss. The capacity loss was much greater than Nafion-117 where the capacity decreased by 50% from cycle 1 to 25.

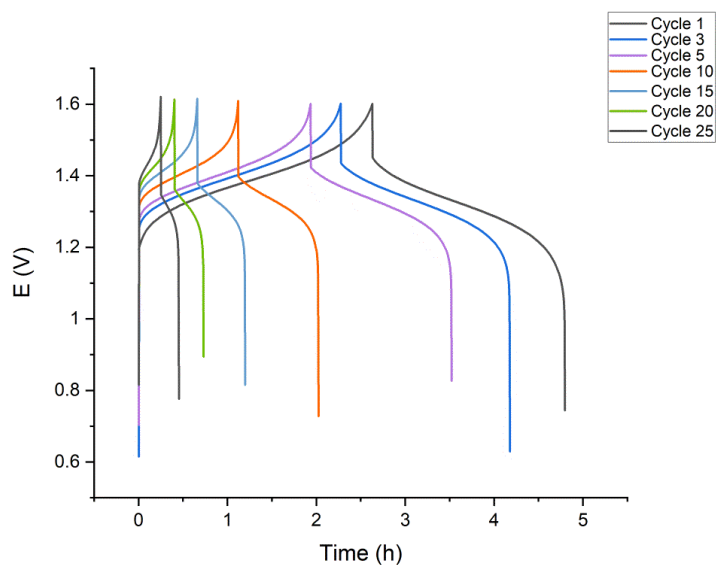


Figure 25 Charge-discharge curves of the 0.1 M $K_4Fe(CN)_6$ / 0.1 M Fe(III) TEA battery with BTMA membrane at 5 mA cm^{-2} between 1.6 and 0.9V upper and lower potential thresholds in the flow cell.

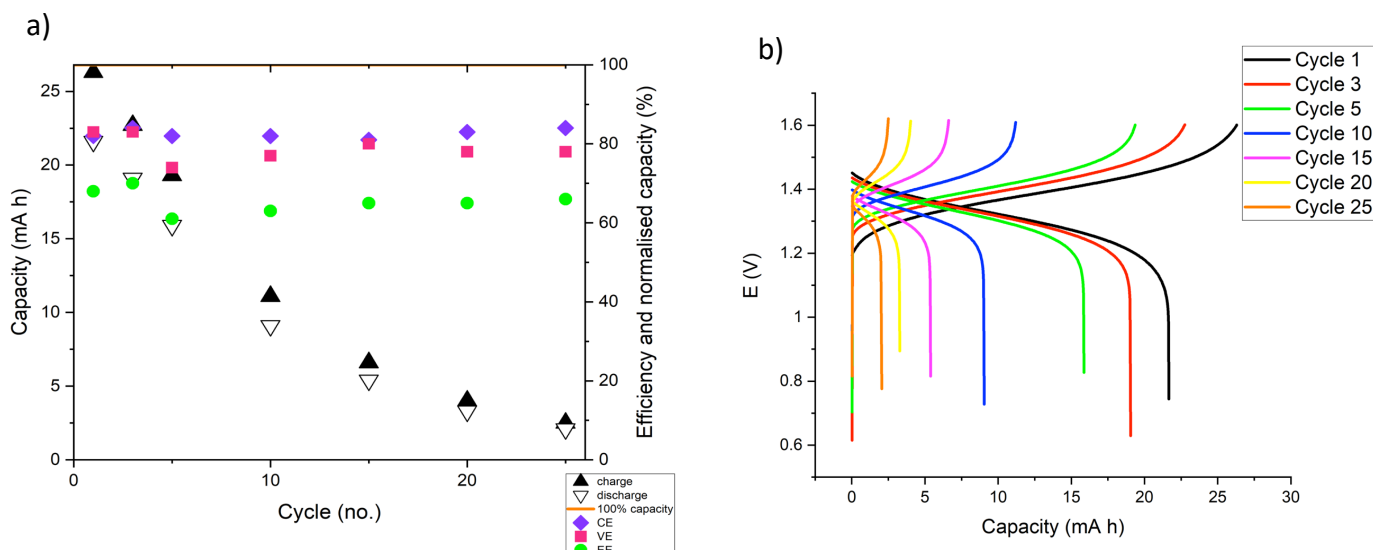


Figure 26 a) Charge-discharge capacities and efficiencies as a function of cycle number. b) Evolution of charge-discharge curves as a function of capacity. (BTMA membrane)

The efficiencies of this system were also poorer compared to the system using a Nafion-117 membrane. Over the 25 cycles the columbic efficiency remained at 81% or above and the voltaic efficiency at 71% or above, the overall energy efficiency remained at 66% or above. Although the efficiencies remained fairly consistent, as seen in Figure 26A, the capacity during charge and discharge decreased rapidly over the 25 cycles, the difference in performance of the systems should be due to the membrane as it is the only variable, this suggests the BTMA

membrane is not as suited to RFB applications as Nafion-117, this could be due to its large ion-exchange capacity.⁷²

Despite the synthesised Fe(III) TEA having a large peak separation in cyclic voltammetry and A charge-discharge experiment of the synthesised Fe(III) TEA with $K_4Fe(CN)_6$ was also carried out with a Nafion-117 membrane. The flow cell and electrode material were consistent with previous experiments. The charge-discharge study cycling took place at 5 mA cm^{-2} current density, this can be seen in Figure 27, although the electrolytes had been successfully charged and discharged the system's capacity decreased much faster than the un-synthesised Fe(III) TEA battery, therefore the synthesised Fe(III) TEA electrolyte was not investigated any further.

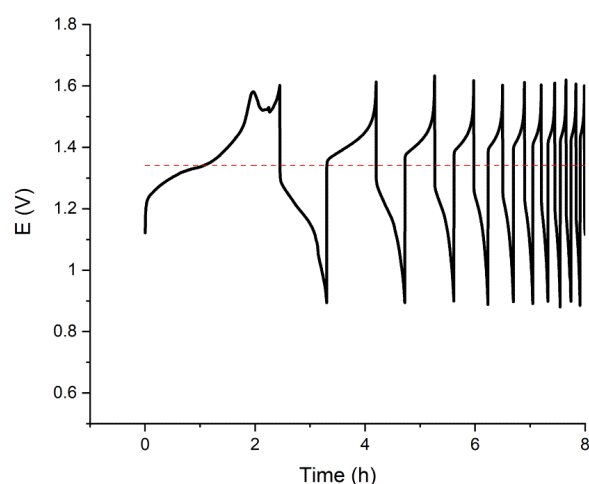


Figure 27 Charge-discharge curves of the $0.1\text{ M } K_4Fe(CN)_6$ /synthesised Fe(III) TEA battery at 5 mA cm^{-2} between 1.6 and 0.9V upper and lower potential thresholds in the flow cell.

3.3.4 Capacity loss investigations

Symmetric cycling

The charge-discharge studies using $K_4Fe(CN)_6$ and Fe(III)TEA had significant capacity loss over time regardless of membrane and whether the Fe TEA electrolyte was synthesised or not. To investigate this capacity loss further a symmetrical charge-discharge experiment was carried out where Fe(III) TEA was cycled against Fe(II) TEA. Figure 28 shows how the capacity retention rapidly decreases when Fe(III/II) TEA are cycled against each other, this shows the Fe TEA

degradation whilst charging and discharging. The electrolyte was prepared as an Fe(III) complex which would remain stable over many weeks under nitrogen which was proven by voltammetry which suggests the degradation comes from the Fe(II) complex.

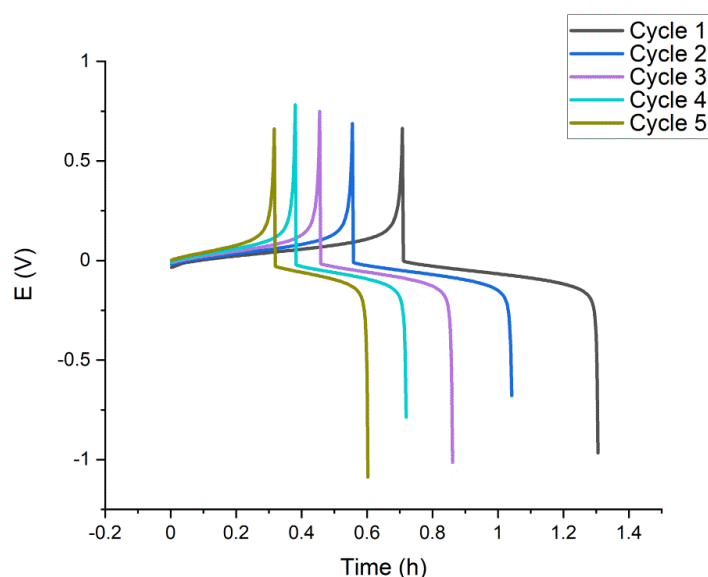


Figure 28 Charge-discharge curves of the symmetrical Fe(II/III) TEA battery with Nafion-117 membrane at 5 mA cm^{-2} between 1V and -1V upper and lower potential thresholds in the flow cell.

The symmetrical cycling of the Fe TEA electrolyte suggested that the electrolyte degrades over time, to further investigate the stability of the Fe(III/II) TEA complex 100 cyclic voltammograms that were recorded continuously at 0.1 Vs^{-1} . As seen in Figure 29, by scan 15 the oxidation peak from the oxidation of Fe(III) to Fe(II) becomes undefined and messy. This suggests that the complex in the +2 oxidation state becomes unstable over time and this could be causing the capacity decay. To assess this hypothesis the Fe(III) TEA was charged against $\text{K}_4\text{Fe}(\text{CN})_6$ and the cyclic voltammetry of the charged electrolyte (Fe(II) TEA) was recorded, as seen in Figure 29b the oxidation reaction from Fe(III) to Fe(II) has two undefined peaks which provides additional evidence to prove the Fe TEA complex becomes unstable when iron is in a +2 oxidation state.

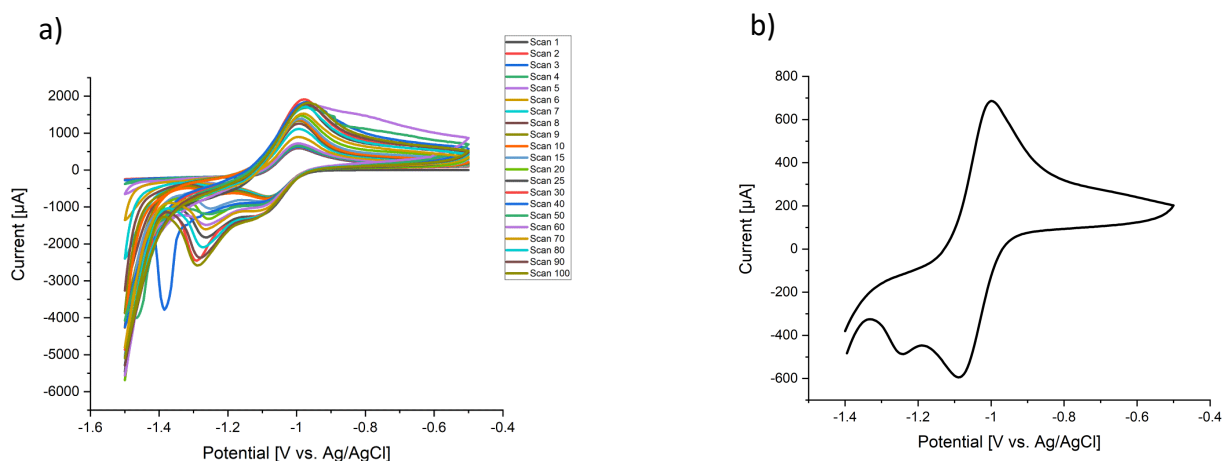


Figure 29 a) 100 Cyclic Voltammograms of 0.1M Fe TEA electrolyte at 0.1 Vs⁻¹. b) Cyclic voltammetry of a charged Fe TEA (+2 oxidation state) at 0.1 Vs⁻¹ scan rate, N₂ atmosphere. first scan shown.

To confirm that the Fe(III) TEA electrolyte was responsible for the capacity loss of the system an assessment of the Fe(CN)₆ electrolytes stability and suitability for use in a RFB application was carried out, both by voltametric cycling and by symmetrical battery cycling. The ferrocyanide must remain stable during the continuous charge and discharge of the RFB. To assess the electrolyte stability during this type of process 100 cyclic voltammograms were recorded at 0.1 Vs⁻¹ scan rate. Figure 30 voltammetry shows little change and implies that the ferrocyanide complex is considerably more stable than the Fe TEA.

A symmetrical cycling of the ferrocyanide was carried out where a charged version of the electrolyte (Fe³⁺) was cycled against an uncharged electrolyte (Fe²⁺) and the potential as a function of time was recorded. From the graph in Figure 31 we can see cycles 1-10, over the course of these cycles there is a loss of capacity, this wasn't expected as the 100 continuous cycles showed the ferrocyanide complex to be very stable. The ferrocyanide may become unstable over a longer duration of time due to the high pH which could be causing a chemical decomposition associated with the CN⁻ ligand dissociation.³⁷

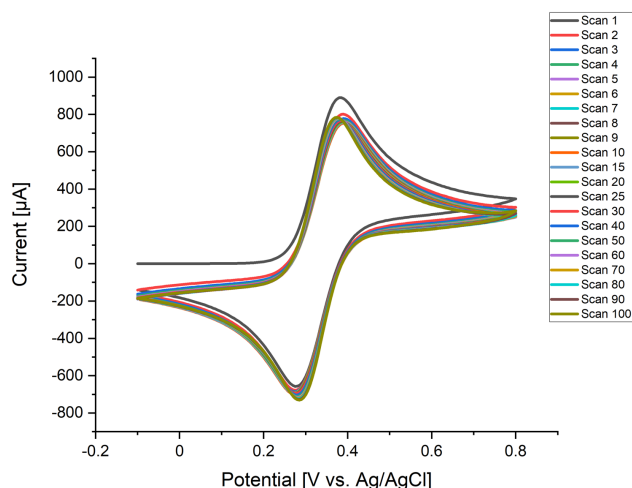


Figure 30. 100 continuous cyclic voltammetry scans of 0.1 M $K_4Fe(CN)_6$ in 1 M NaCl with 3 M NaOH at 0.1 Vs^{-1} scan rate, N_2 atmosphere, GC WE.

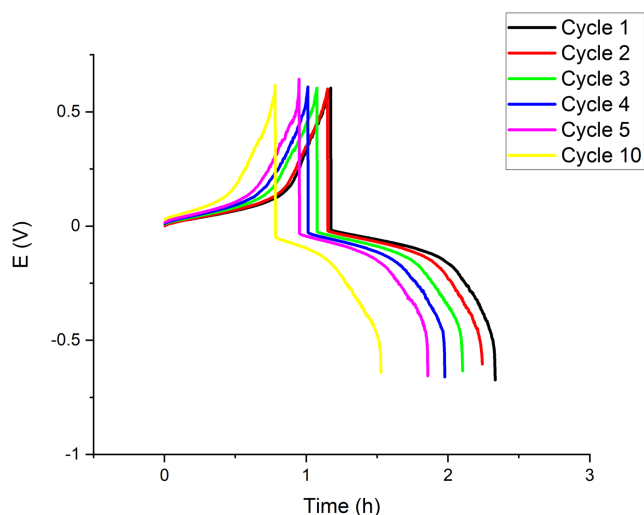


Figure 31 Symmetric flow cell charge-discharge curves of 0.1 M $Fe(II/III)(CN)_6$ in 1 M NaCl 3 M NaOH solution. Nafion-117 membrane at 5 mA cm^{-2} between 1V and -1V upper and lower potential thresholds in the flow cell.

Membrane crossover

The reported literature on this redox couple suggests that the capacity loss is due to the labile TEA ligand crossing over the membrane.⁴⁷ The TEA labile ligand is said to be able to dissociate from the iron core and crossover the membrane due to its small size.⁴⁷ The crossover of the ligand leads to contamination of the RFB and capacity loss. To investigate, a crossover study

was carried out where the Fe(III) TEA electrolyte was cycled continuously through one half of the flow cell at a rate of 20 mL/min without a current being applied. The other half of the flow cell contained a 'blank' electrolyte, which contained 1 M NaCl and 3 M NaOH, both halves of the flow cell were separated by a Nafion-117 membrane. Both electrolytes were flowed through the flow cell without charging/discharging for a week. This was to assess if the Fe(III) TEA crosses over the membrane over time, this was assessed by taking UV-Vis spectra of the blank electrolyte daily. As the 1 mM concentration of the Fe(III) TEA solution is transparent the UV section of the spectrum was used to assess the crossover using the absorbance peak $\lambda = 219$ nm. From the UV-vis graph shown in Figure 32 it can be seen that the concentration of Fe(III) TEA in the blank solution increases over time proving that Fe(III) TEA crosses over the Nafion-117 membrane, by day three of cycling there is the equivalent of a 1mM Fe(III) TEA concentration in the blank electrolyte. The rate of this crossover would be amplified if the system was being charged/discharged as a current would be applied. The crossover of electrolytes in a RFB leads to a loss of materials in each half cell and will account for some of the capacity loss seen in this system.

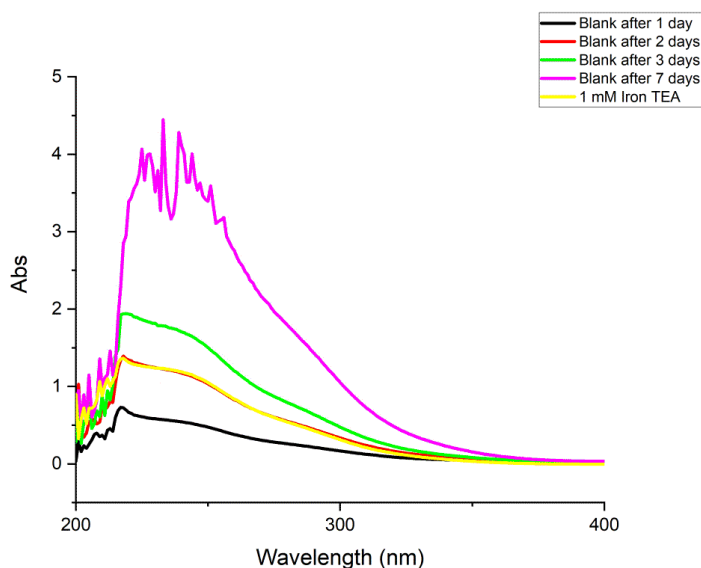


Figure 32 UV-Vis spectra of the 'blank' supporting electrolyte over 7 days whilst cycling with Fe(III) TEA electrolyte. Absorbance peak = 219 nm

3.4 Conclusions

In conclusion, the Fe(III) TEA electrolyte remains stable under nitrogen but upon charging and discharging there is degradation of the electrolyte. Triethanolamine is known to be a labile ligand and does crossover the membrane which also leads to contamination of the RFB and causes a capacity loss during charge-discharge studies. To improve the system a ligand which imparts a negative redox potential whilst remaining coordinated to the iron centre in both oxidation states is required.

Chapter 4 – Evaluation of Iron(III) Triisopropanolamine

4.1 Background

As discussed in Chapter 1 triisopropanolamine (TiPA) has previously been used in a RFB application where Fe TiPA was cycled with cobalt TiPA. This study suggested that the Fe TiPA electrolyte is more suitable for use in RFB applications compared to Fe TEA as the structure was more stable. TIPA has a similar structure to TEA but has an additional methyl group, as seen in Figure 33 the extra stability of the structure is provided by the additional methyl group. Fe TiPA exhibits a negative redox potential of -1.07 V vs Ag/AgCl, it is therefore a promising candidate for the negative electrolyte in an all-iron RFB. If paired with $K_4Fe(CN)_6$ a formal redox potential of 1.4 V could be achieved. An electrochemical evaluation to assess the stability of Fe TiPA in alkaline conditions was carried out followed by battery cycling experiments with $K_4Fe(CN)_6$. The battery performance was assessed using two membranes, Nafion-117 and BTMA. Crossover studies were performed to evaluate the crossover of TiPA in comparison to TEA. Finally, a stability study on the Fe TiPA was carried out through symmetrical cycling to evaluate and degradation over time.

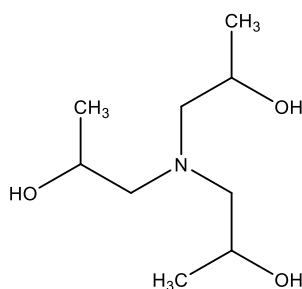


Figure 33 Structure of triisopropanolamine (TiPA) ligand

4.2 Experimental

4.2.1 Material and Reagents

Triisopropanolamine (99%, Sigma Aldrich), Iron(III) chloride hexahydrate (98%, reagent grade), Sodium Chloride (99%, ACS reagent) and Sodium hydroxide (98%, BioXtra) were purchased and used as received.

4.2.2 Electrolyte preparation

Electrolytes were prepared by dissolving 0.1 M FeCl₃.6H₂O dissolving FeCl₃.6H₂O (2.7 g, 0.01 mol) in deionized water followed by triisopropanolamine (8.6 mL, 0.05 mol) , NaOH (12 g, 0.3 mol) and NaCl (5.84 g , 0.1 mol) and the volume made up to 100 mL. Precipitation was observed during the preparation of the electrolytes which re-dissolved. The electrolytes were stored under Nitrogen for 3 days and shaken daily until a clear brown solution could be seen. The Fe(III) TiPA electrolytes pH were adjusted using 3M NaOH to a pH value of 13.9. This was to ensure no precipitation of Fe(OH)₃. The pH of the electrolytes was recorded during electrolyte preparation, before cyclic voltammetry (when the solution had come to equilibrium) and after CV evaluations. During battery cycling the pH of the electrolytes were measured before and after the cycling.

4.2.4 Electrochemical measurements and electrochemical cell

Cyclic voltammograms were performed on a glassy carbon electrode (GC) WE (3mm diameter, BASinc) using a standard 20 mL three electrolyte voltammetry cell (BASinc). A platinum wire (BASinc) served as counter electrode (CE) and Ag/AgCl as the reference electrode (RE) as explained in Chapter 2. The same replica of the Brushett 'Gen2' flow cell used in Chapter 3 was used for all charge-discharge studies

4.3 Results and Discussion

4.3.1 Electrochemical evaluation of Iron(III) TiPA

Beyond the provisional screening study in Chapter 2, voltametric methods were performed on the Fe(III) TiPA electrolyte to investigate the fundamental electrochemical properties and assess its suitability in an all-iron RFBs previously shown in Chapter 2.

From the cyclic voltammograms the peak current from both anodic and cathodic peaks were analysed by Randles-Sevcik analysis at scan-rates $\leq 500 \text{ mV s}^{-1}$ to give a linear dependency on the square root of scan rate. Assuming that the Randles-sevcik Eq. 1) for reversible system is valid the diffusion coefficient for the oxidation of Fe(III) TiPA was calculated as $1.16 \times 10^{-6} \text{ cm}^2 \text{ s}^{-1}$, very similar to that of the Fe(TEA).

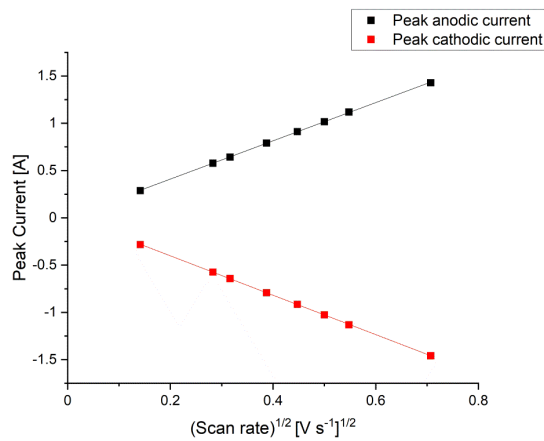


Figure 34 Randles-Sevcik analysis of the Fe(III) TiPA electrolyte scan rate dependence study shown in Figure 12.

Koutecky-Levich analysis as seen in Figure 35 to further confirm mass transport and kinetic information. Linear sweep voltammetry (LSV) as a function of rotation rate gave limiting current plateaus at overpotentials of >1.25 V. The analysis of region 1.1 to 1.4 V overpotential gave somewhat non-linear responses of the inverse current against inverse square-root of rotation rate. A linear relationship is expected for the Koutecky-Levich analysis as a function of rotation rate, the nonlinear results from the data collected could be due to using a small volume of electrolyte (<100 mL), equipment failure or lack of repeats. A corresponding standard electrochemical rate constant of $1.92 \times 10^{-4} \text{ cm s}^{-1}$ and a transfer coefficient of 0.50 was calculated.

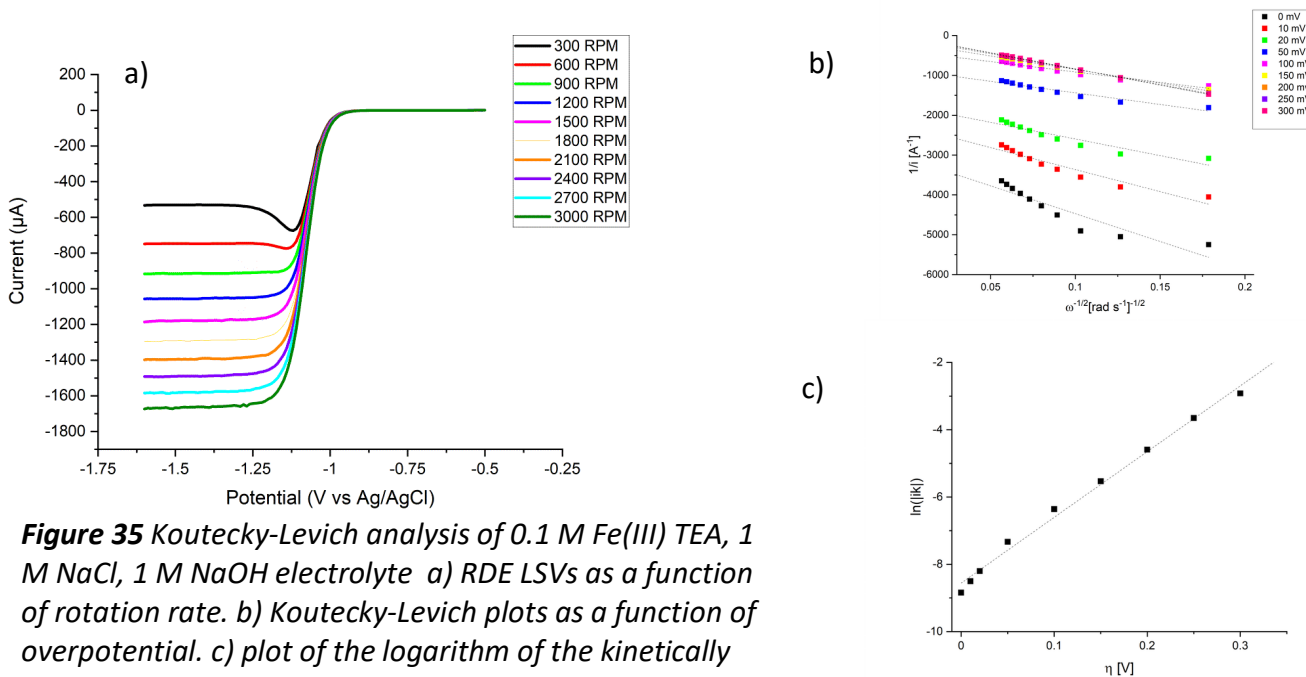


Figure 35 Koutecky-Levich analysis of 0.1 M Fe(III) TEA, 1 M NaCl, 1 M NaOH electrolyte a) RDE LSVs as a function of rotation rate. b) Koutecky-Levich plots as a function of overpotential. c) plot of the logarithm of the kinetically limited current against overpotential.

To assess the electrochemical behaviour and stability of the Fe TiPA further 100 cyclic voltammograms were recorded continuously at a 0.1 Vs^{-1} scan rate. As seen in figure 36 the Fe TiPA voltammograms are essentially all overlapped in the same symmetrical shape showing it remains a reversible system over the 100 cycles. This is unlike the Fe TEA electrolyte where deterioration can be seen by cycle 15, this confirms that the TiPA ligand creates a more stable iron-ligand complex than the TEA, which could be due to TiPA's additional methyl group. This also suggests that Fe(III) TiPA will make a better negative electrolyte in an all-iron RFB.

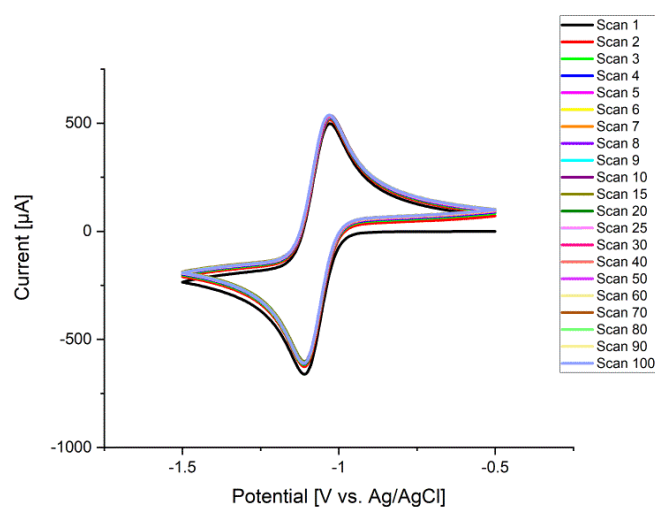


Figure 36 100 continuous cyclic voltammetry scans of $0.1 \text{ M K}_4\text{Fe(CN)}_6$ in 1 M NaCl with 3 M NaOH at 0.1 Vs^{-1} scan rate, N_2 atmosphere, GC WE.

4.3.2 UV-Vis measurements and solubility study

The spectra of the Fe(III) Triisopropanolamine electrolytes were recorded by an Agilent Cary 60 spectrophotometer using a 1 mm path length cuvettes (Starna scientific). The solubilities of the Fe(III) TiPA electrolyte were measured by a UV-Vis method by first acquiring calibration spectra at 0.1 M and 0.2 M concentrations. A UV-Vis spectra of a 1/10 dilution of 0.5 M concentration was recorded. A Beer-Lambert calibration plot was then produced based upon the absorbance ($\lambda = 473 \text{ nm}$) at the UV-Vis peak. The diluted 0.5 M concentration point does not fit the calibration curve showing that Fe TiPA is not soluble at a 0.5 M concentration. A 1.0 M concentration electrolyte was prepared but the salts were insoluble at such high concentration, therefore UV-Vis of the electrolyte wasn't possible and the calibration plot of the Fe(III) TiPA solubility was based on the three soluble concentrations. From the graph in Figure 37 the maximum solubility can be calculated as roughly 0.28 M. This is inconsistent with

literature which suggests a maximum solubility of 0.81 M in 5 M KOH, the discrepancy between our values could be due to different concentration of bases used (3 M NaOH in this work) or use of different initial iron salt, Fe(III) sulphate vs Fe(III) chloride, this could be due to the sulphate being more easily displaced by the TiPA ligands and form a more stable structure.

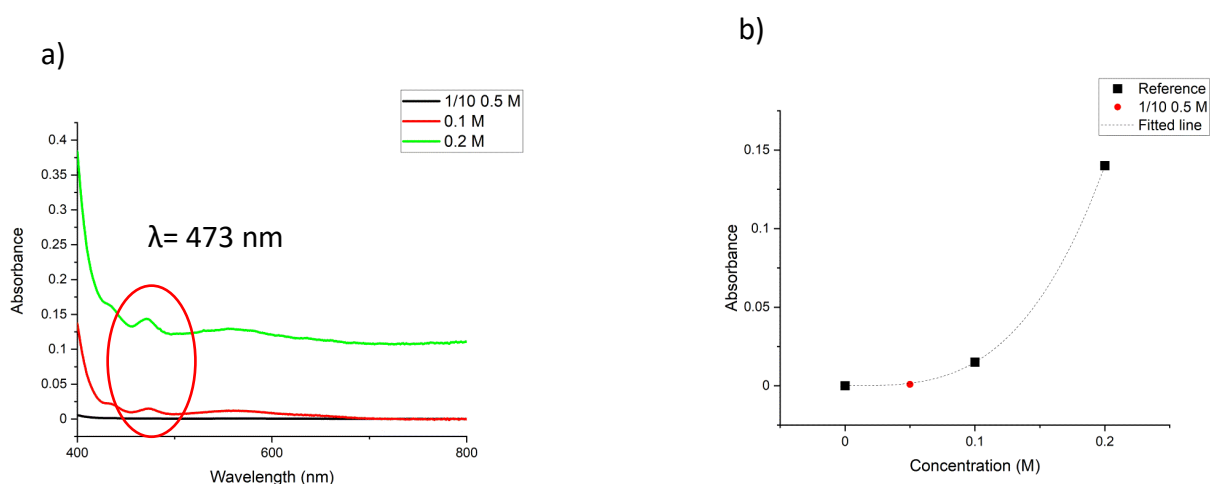
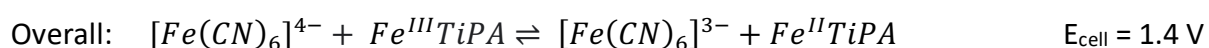
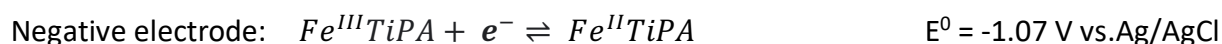


Figure 37 a) UV-Vis spectrum of 0.1 M, 0.2 M and 1/10 diluted 0.5 M concentration of Fe(III) TiPA b) Calibration of Fe(III) TiPA solubility

4.3.3 Charge-discharge studies of $K_4Fe(CN)_6$ / Fe(III)TiPA

Charge-discharge studies were conducted using $K_4Fe(CN)_6$ as the redox active material in the positive electrolyte and Fe(III) TiPA in the negative electrolyte. This study uses only one redox material, iron, and two oxidation states, Fe(II) and Fe(III), meaning the oxidation of the $K_4Fe(CN)_6$ in one electrolyte can be coupled to the reduction of Fe(III) TiPA in the other electrolyte. The electrolytes are reversibly converted from 0-100% SOC, determined by the voltage limits, by repeatedly charging and discharging the cell. The cell allows battery properties, such as redox material stability, to be investigated easily. The corresponding redox reactions and electrode potentials are shown by the following equations.



The initial charge-discharge study of the all-soluble all-Fe RFB was with 10 mL $K_4Fe(CN)_6$ positive electrolyte and 10 mL Fe(III) TiPA negative electrolyte which were stored in separate reservoirs. The electrolyte reservoirs and the flow cell were connected by tubing and the electrolyte was circulated at a flow rate of 20 mL/min. The first membrane assessed in this set up was Nafion-117, a 5 mA cm⁻² current density was used for the charge-discharge cycling, the charge-discharge response was recorded for each cycle and is shown in Figure 38.

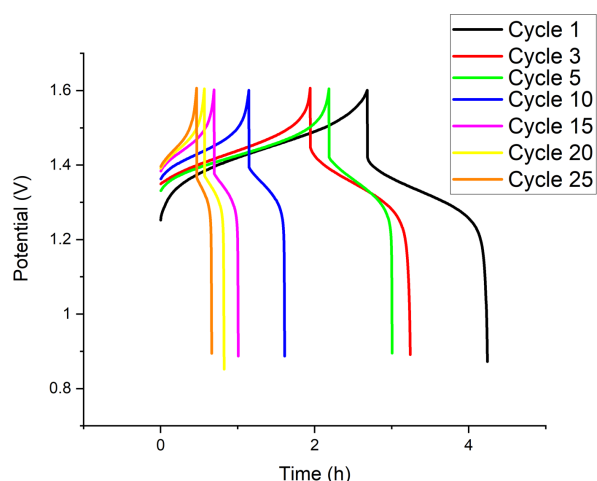


Figure 38 Charge-discharge curves of the 0.1 M $K_4Fe(CN)_6$ / 0.1 M Fe(III) TiPA battery with Nafion-117 membrane at 5 mA cm⁻² between 1.6 and 0.9 V upper and lower potential thresholds in the flow cell.

The theoretical capacity of the system is 2.68 Ah L⁻¹, as 10 mL electrolyte was used the theoretical capacity the system can achieve in the experiment is 26.8 mA h. The time taken to complete a full charge-discharge at the theoretical capacity would be 5.36 h. In the first charge cycle the system achieved a capacity of 26.8 mA h which is 100% relative capacity to the theoretical, however, during discharge a capacity of only 15.6 mA h was achieved. The time taken to complete a charge-discharge cycle decreases with every cycle number. As we can see in figure 38 the capacity during charging considerably decreases between cycles 1-25 from 26.8 mA h at cycle 1 to 4.7 mA h at cycle 25, which is an 82% capacity loss. The graph in figure 39b shows how drastically the capacity reduces over the course of the 25 cycles. The capacity seen during the charging of the system is considerably higher than the capacity of the discharge which can be seen in Table 4, this suggests that the Fe(III) TiPA electrolyte does not discharge fully, because of this the system is not as efficient as the $K_4Fe(CN)_6$ and Fe(III) TEA RFB. The efficiencies of the system can be seen in Figure 39a and are much poorer than that of the $K_4Fe(CN)_6$ and Fe(III) TEA system, the columbic and voltaic

efficiencies generally remains above 37% and the overall energy efficiency of the system remains above 13%. These values were not expected as the preliminary screening of the Fe(III) TiPA looked more promising for use in a RFB than Fe(III) TEA due to its increased structure stability.⁴⁹

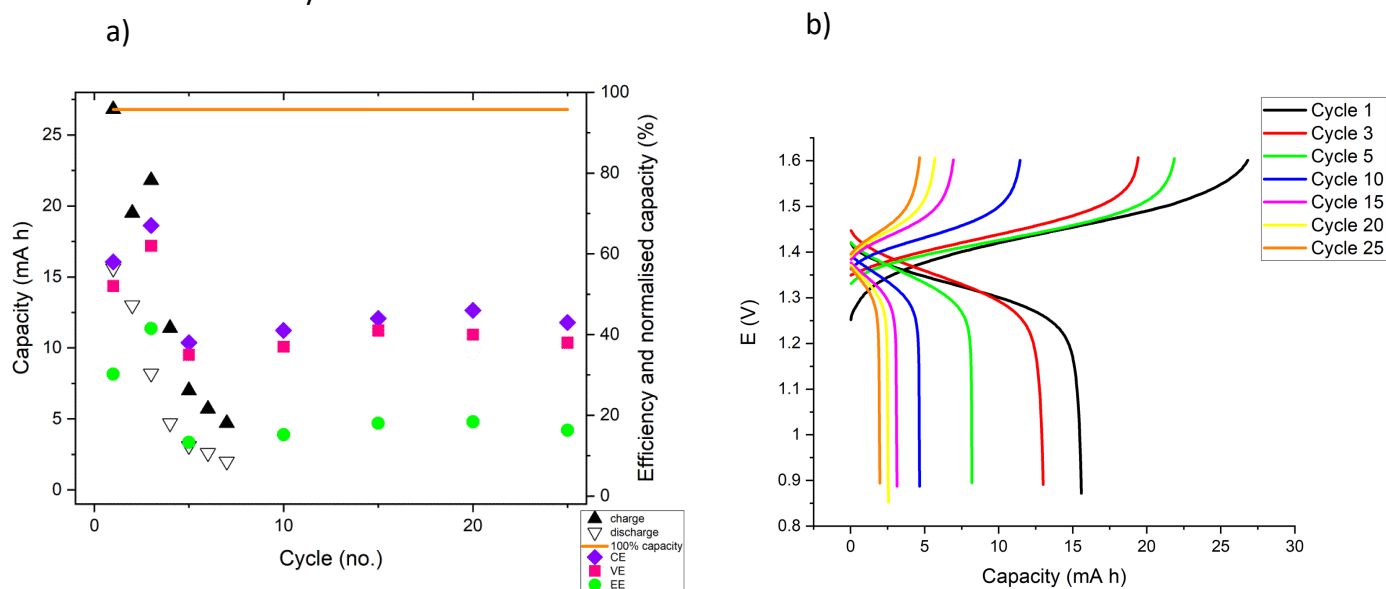


Figure 39 a) Charge-discharge capacities and efficiencies as a function of cycle number. b) Evolution of charge-discharge curves as a function of capacity. (Nafion-117 membrane)

To investigate the Fe(III) TiPA electrolyte further a charge-discharge study was carried out using the $K_4Fe(CN)_6$ and Fe(III) TiPA electrolytes with the BTMA membrane. The cell assembly was consistent with previous flow cell experiments where 10 mL $K_4Fe(CN)_6$ positive electrolyte and 10 mL Fe(III) TiPA negative electrolyte which were stored in separate reservoirs. The electrolyte reservoirs and the flow cell were connected by tubing and the electrolyte was circulated at a flow rate of 20 mL/min and the charge-discharge cycling took place at 5 mA cm^{-2} current density. As seen in Figure 40 the shape of the charge-discharge graph suggests that the battery was unable to discharge fully, which was consistent with the previous experiment with Nafion-117. The capacity loss seen in the system with the BTMA membrane was quicker than that of the system using a Nafion-117 membrane, this is consistent with the $K_4Fe(CN)_6$ and Fe(III) TEA battery experiment where the capacity loss is significantly worse when using the BTMA membrane, this suggests that the iron salt or ligand is able to crossover the membrane easier which contaminates the electrolytes and leads to a quicker capacity loss. The time taken to complete a charge-discharge cycle decreases rapidly from cycle 1 to cycle

25 as does the capacity, from cycle 1 to cycle 25 the capacity decreased by 99% from 20.3 mA h in cycle 1 which is 75.7% relative capacity the theoretical to 0.03 mA h in cycle 25. The capacity loss is greater than that of the system with the Nafion-117 where the capacity decreased by 82% from cycle 1 to 25.

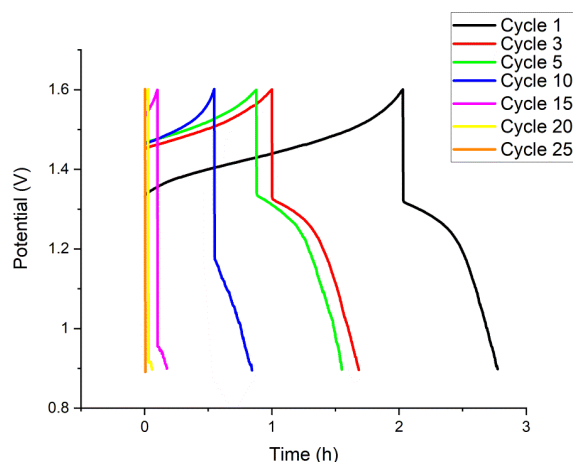


Figure 40 Charge-discharge curves of the 0.1 M $K_4Fe(CN)_6$ / 0.1 M Fe(III) TiPA battery with BTMA membrane at 5 mA cm^{-2} between 1.6 and 0.9 V upper and lower potential thresholds in the flow cell.

The capacity during the charging of the first cycle is 20.3 mA h whilst the capacity of the first cycle discharging is 7.4 mA h, this is a large capacity loss seen within the same cycle. The capacity loss between charge and discharge is also seen in the Nafion-117 system which can be seen in Table 4 and Figure 41b, this confirms that the Fe(III) TiPA electrolyte is unable to discharge fully. The graph in Figure 41a shows the calculated efficiencies of the system including the columbic, voltaic and energy efficiencies which confirmed the system was inefficient due to its large capacity losses.

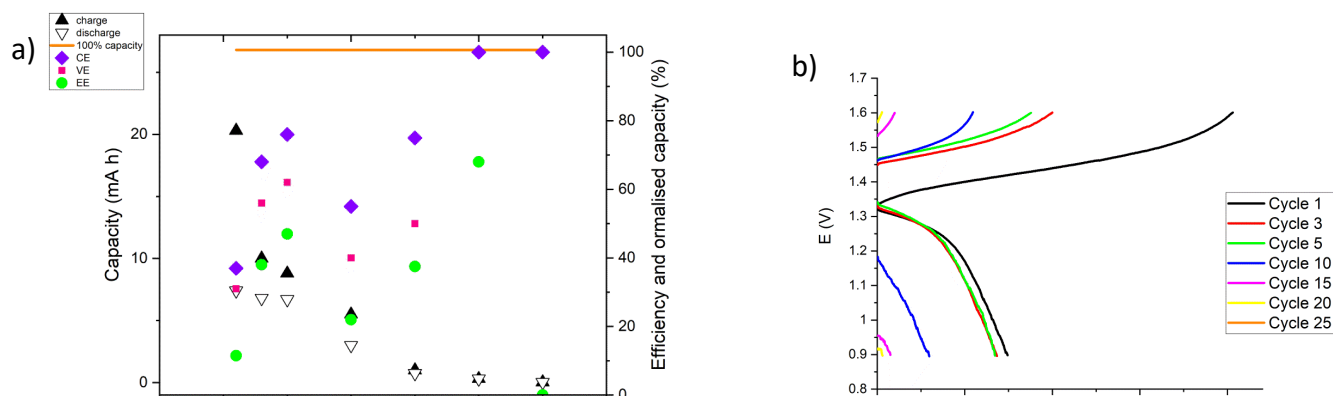


Figure 41 A) Charge-discharge capacities and efficiencies as a function of cycle number. B) Evolution of charge-discharge curves as a function of capacity. (BTMA membrane)

Table 4 shows the capacity loss of the $K_4Fe(CN)_6$ and Fe(III) TiPA system was heightened when using the BTMA membrane, this is consistent with the $K_4Fe(CN)_6$ and Fe(III) TEA system which also performed poorly with the membrane. The ion exchange capacity of the BTMA membrane is double that of the Nafion-117 membrane and could be the reason for increased crossover. In conclusion the Nafion-117 membrane is more suitable for RFB applications.

Cycle	Capacity (mA h)					
	Nafion-117			BTMA		
	Charge	Discharge	Efficiency of charge (%)	Charge	Discharge	Efficiency of charge (%)
1	26.8	15.6	100	20.3	7.4	76
3	19.5	13	73	10	6.8	37
5	21.8	8.2	81	8.8	6.7	33
10	11.4	4.7	43	5.5	3	21
15	7	3.1	26	1	0.75	4
20	5.7	2.6	21	0.3	0.3	1
25	4.7	2	18	0.03	0.03	0.1

Table 4 Capacity during charging and discharging of Fe(III) TiPA with Nafion-117 and BTMA membranes

4.3.4 Capacity loss investigations

The charge-discharge of the $K_4Fe(CN)_6$ and Fe(III) TiPA battery with the BTMA membrane lead to significant capacity loss as did the $K_4Fe(CN)_6$ and Fe(III) TEA battery, therefore the membrane was not investigated further in capacity loss investigations. To investigate the capacity loss seen during the charge-discharge process of the $K_4Fe(CN)_6$ and Fe(III) TiPA battery a degradation study was completed by a symmetrical Fe(III) TiPA cycling where the flow cell was assembled with a Nafion-117 membrane. The Fe(III) TiPA electrolyte was fully charged against $K_4Fe(CN)_6$ and then cycled against an uncharged Fe(III) TiPA electrolyte. As seen in Figure 42 the capacity decreases rapidly between cycle 1 and 10. This confirms that

the capacity loss during previous battery cycling experiments is due to the Fe TiPA electrolyte as it degrades over time with continuous cycling. The capacity loss seen during the symmetrical cycling is consistent with that of the Fe(III) TEA symmetrical cycling although the capacity loss seen during Fe(III) TiPA symmetrical cycling is less significant, this supports the suggestion that the TiPA ligand forms a more stable iron-ligand complex and therefore doesn't degrade as quickly as Fe(III) TEA.

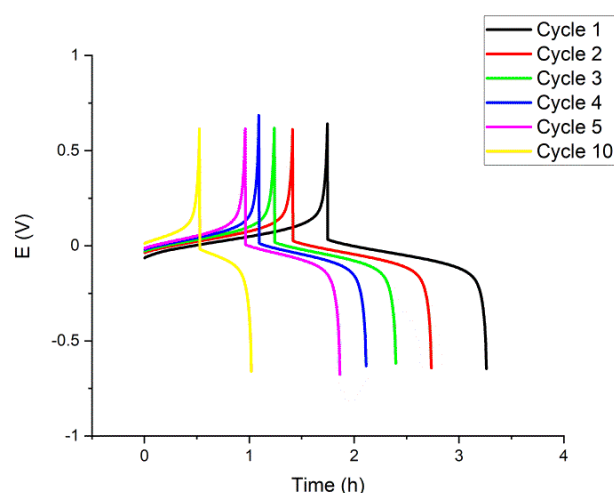


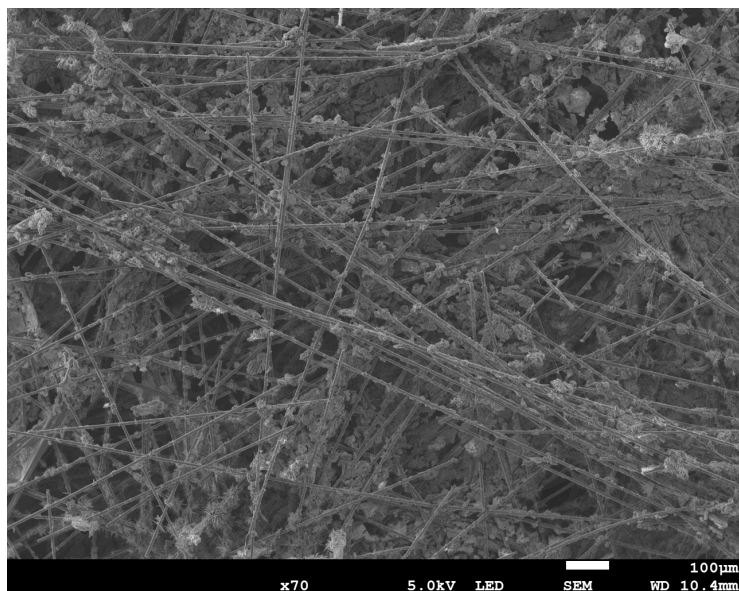
Figure 42 Charge-discharge curves of the symmetrical Fe(II/III) TiPA battery with Nafion-117 membrane at 5 mA cm^{-2} between 1V and -1V upper and lower potential thresholds in the flow cell.

From the symmetrical study seen in Figure 42 we can see that the Fe(III) TiPA degrades as the time taken to charge and discharge the system decreases with cycle number, this can therefore account for some of the capacity loss seen during the $\text{K}_4\text{Fe}(\text{CN})_6$ and Fe(III) TiPA battery. The capacity during discharge decreases by 31 % from cycle 1 to cycle 10 for the symmetrical Fe(III) TiPA whereas the capacity during discharge decreases by 66 % from cycle 1 to cycle 10 for the symmetrical $\text{K}_4\text{Fe}(\text{CN})_6$.

The difference in the loss of capacity could be due to the Fe(III) TiPA depositing on the fibres of the carbon paper electrodes more readily, this was confirmed through SEM and EDX analysis. The wet carbon paper electrodes were dried at $80 \text{ }^\circ\text{C}$ for 6 hours under vacuum to remove moisture before SEM and EDX analysis. The SEM image in Figure 43 shows clear deposits of salts on the carbon fibres and the EDX analysis (Appendix C) confirms that 2.1%

iron is present in the electrodes, the percentage of iron found in the electrodes was higher than the amount of iron in the electrodes used in the Fe(III) TiPA electrolyte, this could account for the additional capacity loss.

a)



b)

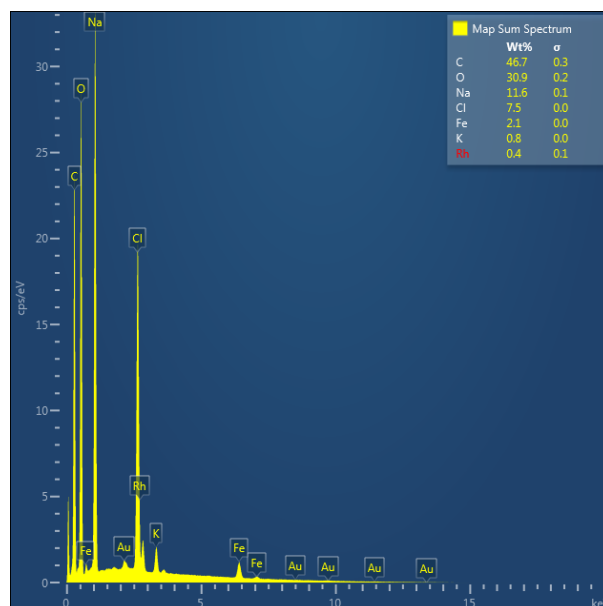


Figure 43 a) SEM image of the carbon paper electrode after use in Fe(III) TiPA. 100 μm scale b) Elemental analysis through EDX analysis.

After the charge-discharge studies the $K_4Fe(CN)_6$ and Fe(III) TiPA electrolytes were studied by cyclic voltammetry to assess any crossover of species during cycling, the CV of the cycled Fe(III) TiPA electrolyte showed no sign of $K_4Fe(CN)_6$. The CV of the cycled $K_4Fe(CN)_6$ seemed to have a small trace of the Fe(III) TiPA present as seen in Figure 44b which suggested a crossover of species from the negative electrolyte to the positive electrolyte. The CV of the Fe(III) TiPA has a large irreversible oxidation peak starting at 0.2 V, which suggests that the TiPA ligand is unstable at high potentials, this would mean that if the TiPA ligand is crossing over the membrane it would be irreparably damaged.

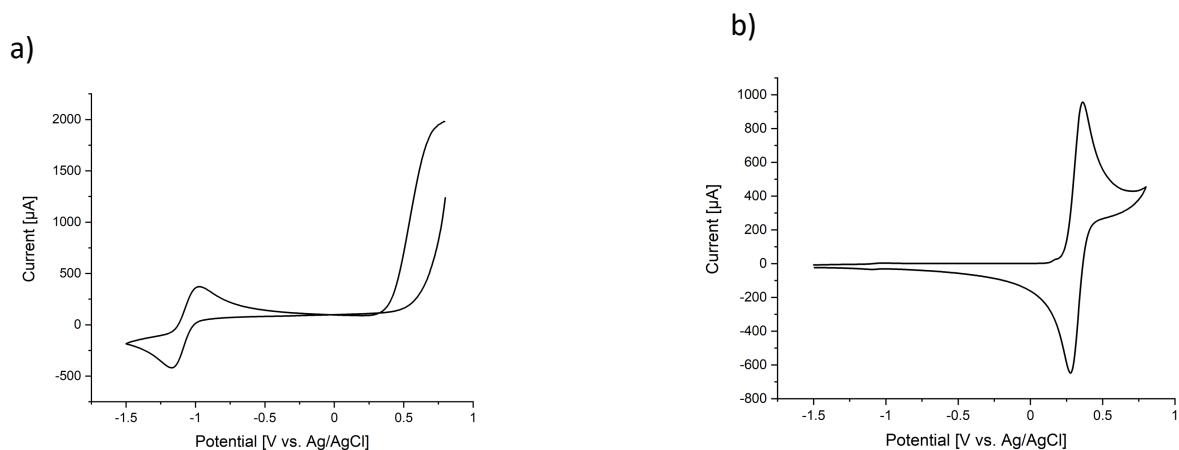


Figure 44 A) Cyclic Voltammetry of 0.1 M Fe(III) TiPA, 1 M NaCl, 3 M NaOH after battery cycling, 0.1 Vs^{-1} scan rate, N_2 atmosphere, first scan shown. B) 0.1 M $\text{K}_4\text{Fe}(\text{CN})_6$, 1 M NaCl, 3 M NaOH after battery cycling, 0.1 Vs^{-1} scan rate, N_2 atmosphere, first scan shown.

A crossover study was carried out where the Fe(III) TiPA electrolyte was pumped through one half of the flow cell (Nafion-117 membrane) without applying a current. The other half of the flow cell contained only a blank electrolyte containing the supporting salt 1 M NaCl and 3 M NaOH. The electrolytes were left pumping through the flow cell for 3 days and UV-Vis samples were taken of the blank electrolyte daily to assess the extent of Fe(III) TiPA crossover through the membrane. As the 1 mM concentration of the Fe(III) TiPA solution is translucent the UV section of the spectrum is used to assess the extent of the crossover as the absorbance peak $\lambda = 220 \text{ nm}$. After 2 days of continuous cycling the concentration of Fe(III) TiPA in the blank electrolyte was above that of 1 mM Fe(III) TiPA which can be seen in the UV-Vis spectrum in Figure 45, the crossover of the Fe(III) TiPA through the Nafion-117 membrane was faster than the crossover of Fe(III) TEA which took an additional 24 hours to achieve the same concentration of iron species.

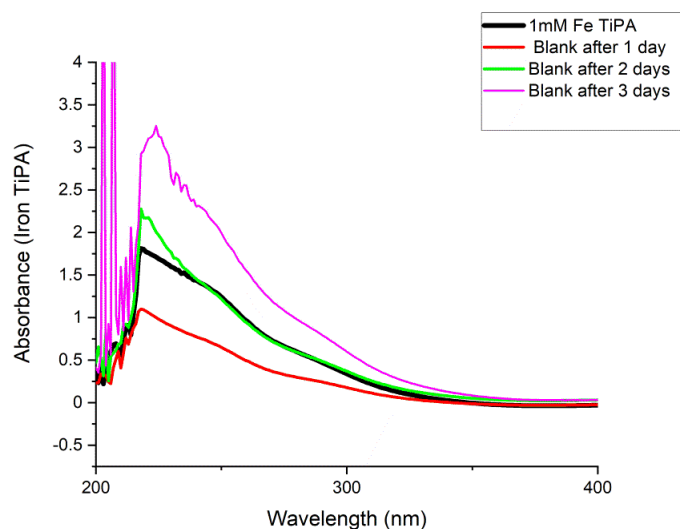


Figure 45 UV-Vis spectra of the 'blank' supporting electrolyte over 7 days whilst cycling with Fe(III) TiPA electrolyte. Absorbance peak = 220 nm

4.4 Conclusions

In conclusion, the Fe(III) TiPA electrolyte remained stable over the 100 cyclic voltammograms unlike Fe(III) TEA which proved the TiPAs increased stability. However, during charge-discharge studies a capacity loss is seen which is greater than that of the Fe(III) TEA battery. On further investigation it is found that Fe(III) TiPA degrades over time and the iron salts deposit heavily on the fibres in the carbon paper electrodes. This was inconsistent with previous Fe(III) TiPA and Fe(III) TEA research where a small amount of iron deposits on the electrodes for TiPA system and a larger amount deposits on the electrodes of the TEA system. Fe(III) TiPA performed well in a Fe-CoRFB at high pH and achieved EE of 65% or above over 100 cycles,⁴⁹ the large contrast in the results obtained in this work could be due to the use of ferrocyanide in the positive electrolyte as previous work used Co TiPA as the posolyte which may be more stable in high pH conditions. To improve the system the solubility of the Fe(III) TiPA would need to be improved and further investigation into the capacity loss is required. The Fe(III) TiPA electrolyte may be better paired to an alternative posolyte.

Chapter 5 – Conclusions and future work

5.1 Conclusion

In conclusion, all-iron RFBs are promising energy storage devices which could store excess renewable energy on a grid scale. They are able to store energy for longer durations of time whilst being cost effective and due to iron's low-toxicity, are likely to have minimal detrimental effect on the environment. To achieve a desirable energy storage capacity in a flow battery a high solubility of iron active material is required. The solubility of the ferric ion in electrolytes at the pHs required for a FeRFB is low as the pH of the ferric ions in the electrolyte has to be above 3 in an all-iron RFB to minimise the HER on the negative electrode. At these pHs precipitation of the ferric ions can occur as $\text{Fe}(\text{OH})_3$, to prevent this precipitation iron is reacted with different complexing ligands to increase solubility. A successful iron-ligand complex will exhibit fast and reversible electrokinetics with moderate solubility and the ligand should be electrochemically inactive.

This work focussed on using a high pH so as to maximise the solubility of the ferrocyanide, a limiting factor in many RFBs using this catholyte. For the anolyte iron was complexed with two different ligands, triethanolamine (TEA) and triisopropanolamine (TiPA). Fe(III) TEA has been used with ferrocyanide in an all-Fe RFB previously and achieved a good energy density but a capacity loss could be seen over time which was attributed to the TEA ligand crossing over the membrane. Charge-discharge experiments were carried out with $\text{K}_4\text{Fe}(\text{CN})_6$ and Fe(III) TEA electrolytes with 2 different membranes, Nafion-117 and BTMA membrane. The system performed better with the Nafion-117 membrane and achieved CE of 83% and VE of 79%, however a capacity loss could be seen over time. Capacity loss in RFB applications is often due to contamination due to crossover of materials, a crossover investigation was carried out and UV-Vis confirmed that Fe TiPA was able to crossover the Nafion-117 membrane over time. The Fe(III) TEA electrolyte stability was investigated in this work by continuous cyclic voltammetry scans and symmetrical cycling which found that the electrolyte became unstable under constant charging and discharging and suggested that the electrolyte was unstable in the +2 oxidation state. As the Fe(II) TEA complex is unstable it is possible that the labile TEA ligand becomes detached from the iron centre and crosses over the membrane due to its small size leading to contamination and capacity loss of the system.

The Fe(III) TiPA complex is a relatively novel iron complex which has only been investigated in an Fe-Co RFB. The Fe(III) TiPA electrolyte proved to be a promising contender for an all-Fe RFB based on its performance in the Fe-Co RFB which showed CE of 98% and VE of 75%. The Fe(III) TiPA electrolyte was paired with $K_4Fe(CN)_6$ in this work to evaluate its performance in an all-Fe RFB. Charge-discharge studies of this system were carried out with both Nafion-117 and BTMA membrane and the efficiency and capacity were evaluated and compared with the $K_4Fe(CN)_6$ and Fe(III) TEA system. It was found that the $K_4Fe(CN)_6$ and Fe(III) TiPA system had larger capacity loss over time due to the electrolytes not discharging properly, in turn this negatively impacted the systems efficiency. The system performed slightly better with the Nafion-117 membrane which was consistent with the Fe(III) TEA system which suggests the BTMA membrane is not as suitable for RFB applications. Overall the $K_4Fe(CN)_6$ and Fe(III) TEA system performed better than the $K_4Fe(CN)_6$ and Fe(III) TiPA system which was unexpected due to the stability study performed where 100 continuous cyclic voltammetry scans were taken of each electrolyte which showed that the Fe(III) TiPA remained stable over the 100 scans whereas the Fe(III) TEA became unstable by scan 15. The difference in performance of the battery experiments could be due to Fe(III) TiPA electrolyte depositing iron more readily in the carbon paper electrodes which was confirmed by SEM and EDX analysis. The alkaline conditions used seems to have been a contributing factor to the problematic capacity loss, and is therefore not suited to further flow battery studies of an all iron system.

5.2 Future work

The future of aqueous all-iron RFBs relies on improving the stability and solubility of the iron salts/iron-ligand complexes in the electrolytes. The solubility of the Fe(III) TiPA and Fe(III) TEA and many other iron-ligand complexes is low and further work is needed in improving the solubility of the complexes to achieve a desirable energy density, increased solubility may be achieved by using alternative pH conditions and supporting salts. The use of additives may also improve the solubility whilst helping to stabilise the complex, an increased complex stability will ensure less degradation of the electrolytes and increase capacity retention.

New Iron-ligand complexes should also be investigated using novel ligands to assess their suitability for use in aqueous all-iron RFB by evaluating their redox potential, stability and solubility. The ligands should remain low cost and have a non-detrimental effect of the environment to create a sustainable an all-iron RFB.

References

- ¹ S. Nalley, International Energy Outlook, EIA, 2021.
- ² S. Yao, S. Zhang, X. Zhang, *J. Cleaner prod*, 2019, **235**, 1338-1352.
- ³ J. Cho, S. Jeong, Y. Kim, *Energy Combust. Sci.*, 2015, **48**, 84.
- ⁴ M.H. Chakrabarti, S. a. Hajimolana, F.S. Mjalli, M. Saleem, I. Mustafa, *Arab. J. Sci. Eng.*, 2013, **38**, 723–739.
- ⁵ J. A. Mellentine, MSc Thesis, University of Iceland, 2011 K. Xu, *Chem. Rev*, 2004, **104**, 4303–4417.
- ⁶ G. J. May, A. Davidson, B. Monahov, *J. Eng st*, 2018, **15**, 145-157.
- ⁷ K. Xu, *Chem. Rev*, 2004, **104**, 4303–4417.
- ⁸ J. Noack, N. Roznyatovskaya, T. Herr and P. Fischer, *Angew. Chem. Int. Ed.*, 2015, **54**, 9776–9809.
- ⁹ A. Z. Weber, M. M Mench, J. P. Meyers, P. N. Ross, J. T. Gostick, Q. Liu, *J. Appl Electrochem*, 2011, **41** 1137–1164.
- ¹⁰ E. Sum, M. Skyllas-Kazacos, *J. Power Sources*, 1985, **15**, 179–190.
- ¹¹ PVEducation, "https://www.pveducation.org/pvcdrom/battery-characteristics/battery-efficiency" <https://www.pveducation.org/pvcdrom/battery-characteristics/battery-efficiency> (accessed January 2021).
- ¹² A. Clemente, R. Costa-Castello, *Energ*, 2020, **13**, 4514.
- ¹³ L. H. Thaller, NASA, TM-X-71540, 1974.
- ¹⁴ Z. Yang, J. Zhang, M.C. Kintner-Meyer, X. Lu, D. Choi, J.P. Lemmon, J. Liu, *Chem. Rev*, 2011, **111**, 3577-3613.
- ¹⁵ R. A. Potash, J. R. McKone, S. Conte, H. D. Abruna, *J. Electrochem Soc*, 2016, **163**, A338-A344
- ¹⁶ M. Skyllas-Kazacos, D. Kasherman, D.R. Hong, M. Kazacos, *J. Power. S*, 1991, **35**, 399–404.
- ¹⁷ M. Rychcik, M. Skyllas-Kazacos, *J. Power. S*, 1988, **22**, 59–67.
- ¹⁸ Y. K. Zeng, T.S Zhao, L. An, X. L. Zhou, L. Wei, *J. pow sourc*, 2015, **300**, 438-443.
- ¹⁹ Sigmaaldrich, <https://www.sigmaaldrich.com/catalog/product/aldrich/204854?lang=en®ion=GB>, (accessed January 2021).

-
- ²⁰ A. Tomaszewska, Z. Chu, X. Feng, S. O'Kane, X. Liu, J. Chen, C. Ji, E. Endler, R. Li, L. Liu, Y. Li, S. Zheng, S. Vetterlein, M. Gao, J. Du, M. Parkes, M. Ouyang, M. Marinescu, G. Offer, B. Wu, *eTransportation*, 2019, **1**, 1-28.
- ²¹ W. Duan, J. Huang, J.A. Kowalski, I.A. Shkrob, M. Vijayakumar, E. Walter, B. Pan, Z. Yang, J.D. Milshtein, B. Li, C. Liao, Z. Zhang, W. Wang, J. Liu, J.S. Moore, F.R. Brushett, L. Zhang, X. Wei, *ACS Energy Lett*, 2017, **2**, 1156–1161.
- ²² J. Huang, B. Pan, W. Duan, X. Wei, R.S. Assary, L. Su, F.R. Brushett, L. Cheng, C. Liao, M.S. Ferrandon, W. Wang, Z. Zhang, A.K. Burrell, L.A. Curtiss, I.A. Shkrob, J.S. Moore, L. Zhang, The lightest organic radical cation for charge storage in redox flow batteries, *Scientific reports*, 2016, **6**.
- ²³ J. F. Kucharyson, L. Cheng, S. O. Tung, L. A. Curtiss, L. T. Thompson, *J. Mater Chem. A*, 2017, **5**, 13700-13709.
- ²⁴ A.A. Shinkle, A.E.S.S. Sleightholme, L.D. Griffith, L.T. Thompson, C.W. Monroe, *J. Power Sources*. 2012, **206**, 490–496.
- ²⁵ P.J. Cabrera, X. Yang, J.A. Suttill, R.E.M. Brooner, L.T. Thompson, M.S. Sanford, *Inorg Chem*, 2016, **54**, 10214–10223.
- ²⁶ C. Schotten, T. Nicholls, R. A. Bourne, N. Kapur, B. N. Nguyen, C. E. Willans, *Green Chem*, 2020, **22**, 3358-3375.
- ²⁷ A. Dinesh, S. Olivera, K. Venkatesh, *Environ Chem Lett*, 2018, **16**, 683–694.
- ²⁸ G. Berckmans, M. Messagie, J. Smekens, N. Omar, L. Vanhaverbeke, J. Van Mierlo, *Energies*, 2017, **10**, 1314.
- ²⁹ L. W. Hruska, R. F. Savinell, *J. Electrochem Soc*, 1981, **128**, 18–25.
- ³⁰ T. J. Petek, PhD thesis, Case Western Reserve University, 2015.
- ³¹ C. P de Leon, A. Frias-Ferrer, J. Gonzales-Garcia, D. A. Szanto, F. C. Walsh, *J. Power Sources*, 2006, **160**, 716.
- ³² Y. Mori and H. Yokoi, *Chem Soc Japan*, 1994, **67**, 2724.
- ³³ A. G. Sharpe, *Inorganic Chemistry*, Pearson Education UK, 2012.
- ³⁴ Western Oregon University, <https://wou.edu/las/physci/ch412/pourbaix.htm>, (accessed January 2021).
- ³⁵ K. L. Hawthorne, DPhil thesis, Case Western Reserve University, 2014.
- ³⁶ B. Li, J. Liu, *Nat Sci Rev*, 2017, **4**, 91-105.

-
- ³⁷ J. Luo, A. Sam, B. Hu, C. DeBruler, X. Wei, W. Wang, T. L. Liu, *Nano Energy*, 2017, **42**, 215-221.
- ³⁸ US Pat., 4180623, 1979,
- ³⁹ C. Chu, B. W. Kwon, W. Lee, *Korean J. Chem. Eng.*, 2019, **36**, 1732–1739.
- ⁴⁰ I. M. Kolthoff, W.J. Tomsicek, *J. Phys. Chem.* 1934, **39**, 945–954.
- ⁴¹ Y. W. D. Chen, K. S. V. Santhanam, and A. J. Bard, *J. Electrochem Soc*, 1981, **128**, 1460.
- ⁴² A. S. N. Murthy and T. Srivastava, *J. power source*, 1989, **27**, 119.
- ⁴³ P. Modiba, M. Matoetoe, and A.M. Crouch, *Electrochimica Acta*, 2013, **94**, 336.
- ⁴⁴ J. G. Ibanez, C. S. Choi, and R. S. Becker, *J. Electrochem Soc*, 1987, **134**, 3083.
- ⁴⁵ P. Modiba, M. Matoetoe and A. M. Crouch, *J. Power Sources*, 2012, **205**, 1-9.
- ⁴⁶ Y.H. Wen, H. M. Zhang, P. Qian, H. T. Zhou, P. Zhao, B. L. Yi, and Y. S. Yang, *Electrochimica Acta*, 2006, **51**, 3769.
- ⁴⁷ K. Gong, F. Xu, J. B. Grunewald, X. Ma, Y. Zhao, S. Gu, Y. Yan, *ACS Energy Lett*, 2016, **1**, 89–93.
- ⁴⁸ S. Mingyu, N. Chanho, C. Yongjin, K. Yongchai, *Chem Eng J*, 2020, **398**, 125631.
- ⁴⁹ C. Noh, Y. Chung, Y. Kwon, *Chem Eng J*, 2021, **405**, 126966.
- ⁵⁰ K. L. Hawthorn, J. S. Wainright, R. F. Savinell, *J. Electrochem Soc*, 2014, **161**, 1662–1671.
- ⁵¹ K.L. Hawthorne, T. J. Petek, M. A. Miller, J.S. Wainright, R. F. Savinell, *J. Electrochem Soc*, 2015, **162**, 108–113.
- ⁵² Basi, https://www.basinc.com/manuals/EC_epsilon/Techniques/CycVolt/cv_analysis, (accessed September 2021)
- ⁵³ N. Elgrishi, K. J. Rountree, B. D. McCarthy, R. S. Rountree, T. T. Eisenhart, J. L. Dempsey, *J. Chem. Ed.* 2018, **95**, 197-206.
- ⁵⁴ Y. Chen, M. Zhou, Y. Xia, X. Qin, X. Xu, Q. Wang, *Joul.* 2019, **3**, 2255-2267.
- ⁵⁵ P. L. Domingo, B. Garcia, J. M. Leal, *Can. J. Chem*, 1989, **68**, 228-235.
- ⁵⁶ C. Visy, G. Bencsik, Z. Nemeth, A. Vertes, *Electrochem Acta*. 2008, **53**, 3942-3947.
- ⁵⁷ N. Thoegersen, J. Janata, J. Ruzicka, *Anal. Chem*, 1983, **5**, 1986-1988
- ⁵⁸ A. Derja, A. E. Hanssali, *J. Chim. Phys.* 1997, **94**, 596-583.
- ⁵⁹ Abcam, <https://www.abcam.com/dmsa-meso-23-dimercaptosuccinic-acid-lead-chelating-agent-ab142294.html>, (accessed September 2021)
- ⁶⁰ Spinnbarkeit, *Fac. Den. J*, 2014, **5**, 140
- ⁶¹ J. Luo, A. Sam, B. Hu, C. DeBruler, X. Wei, W. Wang, T. Leo, *Nan Energ*, 2017, **42**, 215-221.

-
- ⁶² A. Le, D. Floner, T. Roisnel, O. Cador, L. Chancelier, F. Gerneste, *Electrochem Acta*, 2019, **301**, 472-477.
- ⁶³ D. Irizarry, thesis, Worcester Polytechnic Institute, 2015.
- ⁶⁴ S. Nikman, DPhil thesis, Lancaster University, 2020.
- ⁶⁵ F. R. Brushett, J. D. Milshteun, J. L. Barton, *JCESR*, Massachusetts Inst Tech, 9-17.
- ⁶⁶ J.D. Milshtein, K.M. Tenny, J.L. Barton, J. Drake, R.M. Darling, F.R. Brushett, *J. Electrochem. Soc.* 2017, **164**, E3265–E3275
- ⁶⁷ A. Parasuraman, T. M. Lim, C. Menictas, M. Skyllas-Kazacos, *Electrochem Acta*, 2013, **101**, 27-40.
- ⁶⁸ C. G. Armstrong, DPhil thesis, Lancaster University, 2020.
- ⁶⁹ H. Prifti, A. Parasuraman, s. Winardi, T. M. Lim, M. Skyllas-Kazacos, *Membrane*, 2012, **2**, 275-306.
- ⁷⁰ X. Li, H. Zhang, Z. Mai, I. Vankelecom, *E & Env Sc*, 2011, **4**, 1147.
- ⁷¹ J. Ponce-Gonzalez, D. K. Whelligan, L. Wang, R. Bance-Soualhi, Y. Wang, Y. Penf, H. Peng, D. C. Apperley, H. N. Sarode, T. P. Pandey, A. G. Divekar, S. Seifert, A.M. Herring, L. Zhuang, J. R. Varcoe, *En Environ Sci*, 2016, **9**, 3724.
- ⁷² L. Gubler, *Cur op Electrochem*, 2019, **18**, 31-36.
- ⁷³ K. Toghill, CHEM 218 Electrochemistry L7 Voltammetry, Lancaster University, 2018.

Appendix A: SEM and EDX analysis of unused carbon paper electrode

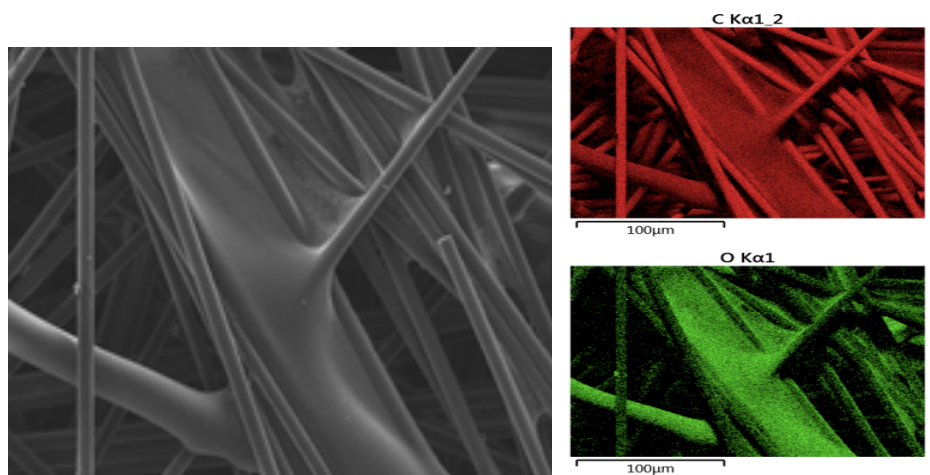


Figure 46. SEM and EDX analysis of the unused carbon paper material (20301A, Technical Fibre Products Ltd) 100 µm scale.

Appendix B: SEM and EDX analysis of carbon paper electrodes for a) $K_4Fe(CN)_6$ b) Fe(III) TEA

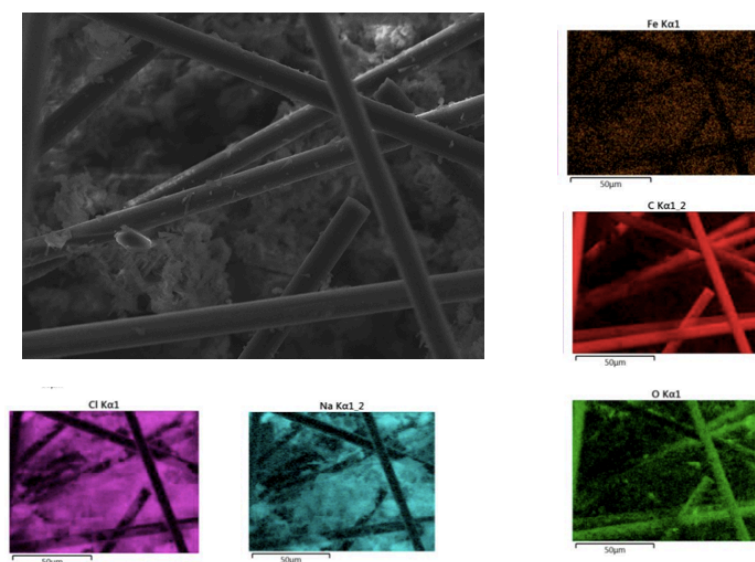


Figure 47. SEM and EDX analysis of the carbon paper material used in $K_4Fe(CN)_6$ (20301A, Technical Fibre Products Ltd). 100 µm scale

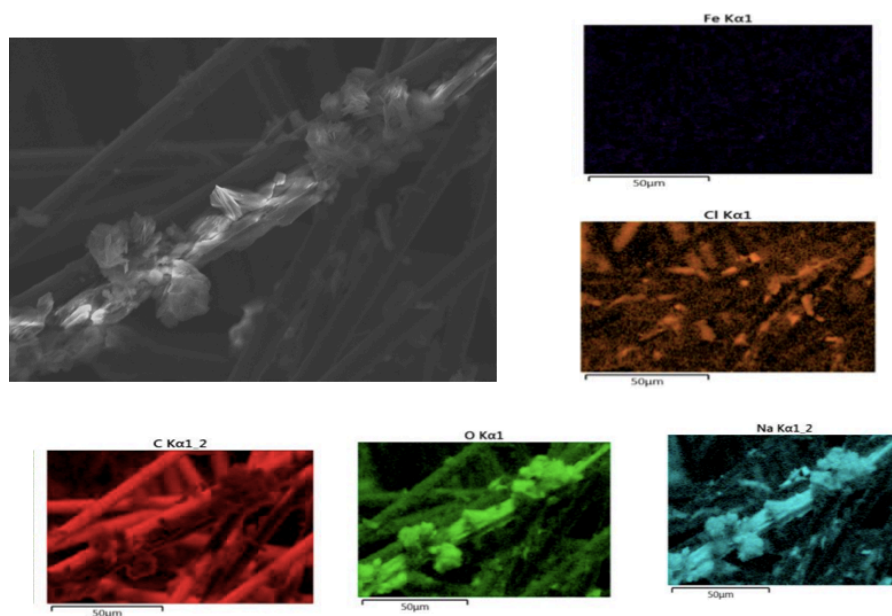


Figure 48. SEM and EDX analysis of the carbon paper material used in Fe(III) TEA (20301A, Technical Fibre Products Ltd) in 100 µm scale.

Appendix C: SEM and EDX analysis of carbon paper electrodes for Fe(III) TiPA

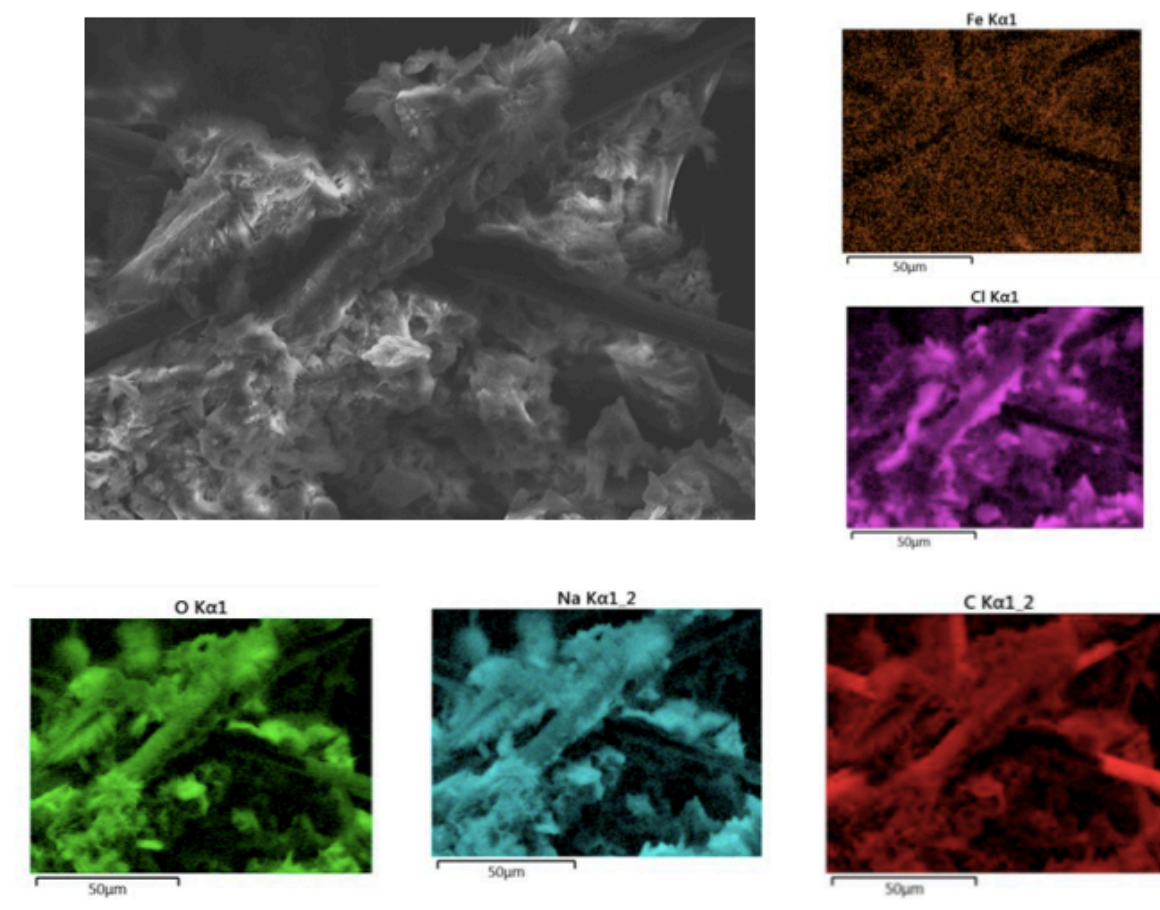


Figure 49. SEM and EDX analysis of the carbon paper material used in Fe(III) TiPA (20301A, Technical Fibre Products Ltd) 100 µm scale.